PULSATING WHITE DWARFS AND ORBITAL DECAY IN BINARIES

Sun, Meng (孙萌)
Beijing, China

B.S., Sichuan University, Chengdu, Sichuan, China 2012

M.S., University of Virginia, Charlottesville, Virginia, USA 2014

A Dissertation Presented to the Graduate
Faculty of the University of Virginia
in Candidacy for the Degree of
Doctor of Philosophy

Department of Astronomy

University of Virginia
June, 2018

Phil Arras

Zhi-Yun Li

Shane W. Davis

Kent Yagi

Abstract

Three projects related to stellar and binary evolution and waves in stars are investigated.

Motivated by the discovery of a handful of pulsating, extremely low-mass white dwarfs (ELM WDs, mass $M \lesssim 0.18\,M_\odot$) which likely have WD companions, a binary formation model was developed for these systems. ELM WD is formed using angular momentum losses due to magnetic braking by the stellar wind of the primary star. Evolutionary models are constructed using the Modules for Experiments in Stellar Astrophysics (MESA), with ELM WD progenitors in the range $1.0 \lesssim M_{\rm d}/M_\odot \lesssim 1.5$ and WD companions in the range $0.4 \lesssim M_{\rm a}/M_\odot \lesssim 0.9$. Upon the thinning of the evolved donor's envelope, the donor star shrinks out of contact and mass transfer ceases, revealing the ELM WD. Systems with small helium core masses have previously been suggested as evolving to the short orbital period, hydrogen poor AM CVN accretors. Systems with large helium core masses expand out to orbital periods $P_{\rm orb} \gtrsim 15\,{\rm hr}$, larger than those of the observed pulsators. In between this range, ELM WDs may become pulsators both as pre-WDs and on the WD cooling track. The resulting models for the stellar structure are used to compute expected g and p-mode periods and compare to the observed periods.

WASP-12b is a hot Jupiter with an orbital period of only $P = 1.1$ day, making it one of the shortest-period giant planets known. Recent transit timing observations measure a decreasing orbital period with $P/\dot{P} = -3.2$ Myr. These observations imply that a Gyrs old planet is now about to be destroyed by its star over the next few Myr. One mechanism to produce orbital decay is through tidal friction. The tide raised in the star by the planet may spin up the star, with the orbit contracting to conserve angular momentum. Calculations are presented for the "dynamical tide" excitation

of gravity waves by the time-changing tidal force. The main damping mechanism is nonlinear wave breaking at the center of the star, if the star has a radiative core. I find that the orbital decay rate due to the dynamical tide is insufficient to shrink the orbit if WASP-12 is a main sequence star, since the core is then convective and the low-amplitude gravity wave forms a weakly damped standing wave. However, if WASP-12 is a subgiant star with a radiative core, the dynamical tide breaks nonlinearly at the center of the star. This traveling wave limit may then provide roughly enough friction to account for the observed orbital decay.

In addition to the direct measurement of orbital decay in WASP-12, indirect evidence of orbital decay in binaries containing a post-main sequence star comes from the lack of binaries with close orbital separations, as they have already suffered orbital decay and destruction by the parent star. A broad parameter study of orbital decay is presented for a range of primary and secondary stars as well as orbital separation. The goal is to make predictions for the range of orbital separation at which systems will be missing due to orbital decay and engulfment by the star.

Abstract in Chinese

摘要

本文主要介绍了有关恒星演化、双星演化、恒星的脉动和潮汐的三个相关工作。

随着一些低质量脉动白矮星以及双白矮星系统的发现，本文研究了它们的形成和演化过程。极低质量白矮星是在双星中形成的。在演化过程中，由于主星的星风伴随着磁制动效应，两颗星的距离在减小。当主星充满它的洛希半径之后，主星的物质会流向伴星或者宇宙空间。最终主星会形成极低质量白矮星。本文涉及的所有恒星演化过程由一个称为MESA的开源程序模拟。极低质量白矮星的前身是一颗质量范围在1 - 1.5倍太阳质量之间的恒星，其白矮星伴星的质量范围在0.4 - 0.9太阳质量。主星在经历白矮星冷却之前，半径减小，此时它不再充满它的洛希半径，这时两颗星的物质交换会停止。在主星开始丢失质量之前，双星系统中的主星如果只有一个很小的氦核，那么这种系统会形成AM CVn系统。AM CVn双星系统的轨道周期一般小于一小时，且缺乏氢元素。若在主星开始丢失质量之前，主星已经有一个较大的氦核，这种系统会演化成轨道周期大于15小时的致密星系统。而本文讨论的脉动低质量白矮星，介于这两种系统之间。此外，我们还利用模拟得到的极低质量白矮星模型计算了它的本征频率，包括g模式和p模式，并和观测到的震动频率做了比较。

WASP-12b是一颗热木星，其轨道周期仅有1.1天，使得它成为离其主星最近的系外行星之一。从观测上，我们得到，这个系统的轨道周期在以大约29毫秒每年的速度在减小。这些结果表明，这颗几十亿年的行星，将会在接下来的几百万年里被恒星吞噬。一种造成轨道半长轴缩小的机制是潮汐。行星在恒星表面制造的潮汐产生的摩擦力，可以加速恒星的自转。如果假定系统角动量守恒并忽略行星的自转角动量，恒星自转加速意味着恒星自转角动量增加，导致轨道角动量的减小，此时轨道半长轴也减小。为研究此现象，我们计算了动力学潮汐在此系统中的作用，动力

学潮汐就是星震学中的重力波，其回复力是浮力，只能在辐射区传播。这种动力学潮汐在恒星靠近外部的对流层和辐射层交界处产生，并向恒星内部传播。如果这种重力波能传播到恒星中心附近的辐射区，此时他的振幅要大于波长(非线性制动，类比水波碰到海岸：水波传到岸边附近，其振幅大于波长，然后波不再向前传播)，波停止传播，所携带能量也转化为热能储存在恒星中心。如果WASP-12是一颗主序星，其中心是对流区，则动力学潮汐的作用非常小，重力波在到达恒星之前就从核对流区和外层辐射区交界处弹回，波的能量不能转化为热能，形成驻波。但是，如果WASP-12是一颗矮巨星，其结构包含一个核辐射区和一个对流区包层，动力学潮汐将在恒星中心的辐射区显著衰减，从而把波的能量在此转化成热能。假定WASP-12是矮巨星，通过计算得出的动力学潮汐的能量耗散率和WASP-12系统的轨道周期衰减率可以达成一致。

对于WASP-12系统，我们是直接观测到了它的轨道衰减速度。潮汐作用被间接观测到的实例是，很少有非常近距离的、且包含一颗晚期恒星的双星系统被发现，因为伴星在观测到之前就已经和主星合并。在另外一项工作中，我们以主星质量、伴星质量和轨道周期为变量，对潮汐在主星演化的过程中对轨道半长轴的影响进行了研究。详细来说，质量范围在1-3倍太阳质量之间的主星，我们研究了它从零龄主序星到红巨星阶段的潮汐作用，动力学潮汐(由非线性制动和辐射耗散使其衰减)和平衡潮汐(由对流区的湍流使其衰减)均被考虑在内。最后，本文的理论结果和APOGEE红外巡天项目以及系外行星系统的观测做了比较。

Acknowledgements

I came to UVa as a raw astrophysics student with almost no experience in coding. Without my advisor Phil Arras, I may have had no chance to write down the following chapters. He is the kind of human being that can derive equations and do integrations in his sleep. He also made me realize that people are born with differences in intelligence as he is way smarter than me. It is worth that I came across half of the Earth then became this cool idea reservoir's student. I feel lucky that besides Phil, I was supervised remotely by Nevin Weinberg from one of the centers of the universe, Cambridge, MA. It is a great honor to work with a high class astrophysicist. And he is such a responsible person. During my postdoctoral applications, he uploaded tons of recommendation letters almost instantly.

Thanks to my committee members Zhi-Yun Li, Steve Majewski, Shane Davis and Kent Yagi as they have been tolerant of my procrastination (i.e., this thesis). They are the most popular advisors in the Graduate School of Arts and Sciences. Thank you for giving me so many coding suggestions, science inspirations and thoughts during our discussion.

I also want to express the same gratefulness to Jin Zhu, the curator of the Beijing Planetarium, and Jian Guan, my high school science teacher. Without them, my first hands-on astronomy research would not be finished and I would have no chance of joining the Beijing Teenage Science and Technology Club as an amateur astronomer. They are the two main people that make me decide to devote myself to astronomy. I still remember the experiences of using the small telescopes, running the Messier marathon in Pinggu District, Beijing, taking the trail of the Shenzhou 6 spacecraft near the Juyongguan Great Wall, and the cloudy 2009 total eclipse in Wuhan, China.

Thanks to all of my office mates and 6th-year graduate students Apurva Oza,

Bruce Wu, Dom Pesce, Haifeng Yang, Matt Pryal, Nick Troup, Sandy Liss, Scott Suriano and Yiqing Song for building the best office and classroom environment. Thank you for being always ready for sharing my happiness and sadness, and spending the enormous amount of time to help me edit English articles. You are the best.

My Chinese native speaker fellows: Andy Lam, Bin Chen, Bo Zhao, Changji Cao, Che-Yu Chen, Dong Zhang, Hongxu Dong, Huangxing Li, Mengyao Liu, Mengzhen Wang, Jiaye Guo, Jinchao Zhao, Ruobing (Robin) Dong, Xiaopu Li, Xiaoshan Huang, Xiaping Tang, Wei Han, Wenlan Huang and Zhao Guo, without you, my life would be extremely boring. Even though I am about to graduate, I will never be ready to say goodbye. But I am 100% sure I will still feel your full support remotely.

Thanks to David Rigby for computer and any related technical support. He is a master on any electronics. This is fantastic.

Last but not least, I gratefully acknowledge my parents and husband for always being on my side. ~~Without them, I would be a slim guy~~. Because of the Chinese National Astronomy Olympiad, Chenliang and I have known each other since high school. Then we met again at UVa, which ~~sounds like a Chinese idiom "enemies are fated to meet"~~ proves that "destiny ties people together." My parents would be ready to cross the Pacific Ocean to help me if I gave them a call. I could not ask for more amazing parents than them.

Acknowledgements in Chinese

致谢

由于此章内容阅读人数可能较多，进而我认为有必要备份一份中文版。此章节大意和英文版争取一致，但细节会略有不同，毕竟文学素养不佳，英语也是我一生的痛。英文人名我就不翻译了，因为可能看起来会非常奇怪……当然，如果我能被允许写得搞笑一点的话，就更好了。可惜这里好像不能写段子、不能加表情包、不能加弹幕，无法淋漓尽致的展现我的风趣幽默，真让人感到遗憾。

首先我要感谢几位大佬的全力支持，我的老板Phil Arras和Nevin Weinberg。Phil是一个比我聪明一万倍的人，让我深深的体会到人和人的智商差别，还是很大的。同时我也时常惊讶于他总有各种有趣且可以实践的想法，而且愿意花时间和精力在学生身上。总之，有这样一位良师，我觉得跨过大半个地球来读书，还是值得的。我们虽然和Nevin不在一所学校，但我也受到很多来自Nevin的帮助，比如帮我提交无数封推荐信，还是秒发，完全不用催。当然，给我印象最深的是，他有几篇十分高深的文章，我读好几遍，都不一定能理解一半。作为学生，这种被智商碾压经历，让我又一次完整了人生。

还有我毕业答辩委员会的成员，李老师，Steve Majewski，Shane Davis和Kent Yagi。跪谢他们江湖救急，以及容忍我的各种拖延症。能有这几位无敌炫酷的理论和观测大佬在我的答辩委员会里，考虑到他们又是本学院偶像级人气天团成员，我真是发自肺腑的感受到什么是光宗耀祖。

我能跳天文这个坑，和我高中的经历有着直接关系，毕竟我是在那个阶段起，算是成为一个天文爱好者。我在高一的时候认识了北京天文馆朱进馆长，一个不修边幅特别接地气、一手把国内天文奥赛办起来的人。当年和我们一起参加过竞赛的同好，已经有不少人和我一样准备开始或者已经开始相关领域的博后生涯了。还有北京汇文中学的科技老师，关键老师，没有他，我恐怕也没有机会认识朱进馆长，也没有机会参加北京市科技俱乐部这样一个高大上的组织。在此感谢他们两位，带

我入门，学习使用小望远镜、机械单反相机，组织各种天文观测活动。印象比较深的是第一次玩梅西耶天体马拉松，坐标北京平谷区黄松峪；张北坝上草原的星空大会；一帮人大半夜跑到居庸关长城附近拍神舟六号过境的轨迹；2009年武汉的阴天日全食(说多了都是泪)，这都是弥足珍贵的回忆。

这一波说的是和我同年入学以及同办公室的同学，Apurva Oza, Bruce Wu, Dom Pesce, Matt Pryal, Nick Troup, Sandy Liss, Scott Suriano, 宋一清和杨海峰。感谢他们在我感到万分沮丧甚至开始怀疑人生的时候，随时倾听我的各种吐槽。都是出来混的(划掉，改成共患难的人)，日子挺苦挺不容易的，记得多喝热水，喜欢就买，不行就分，重启试试。

感谢我那些说汉语的同学和各路师兄师姐师弟师妹们：Andy Lam，曹长际，陈彬，陈哲宇，董红序，董若冰，郭佳叶，郭钊，韩薇，黄雯兰，黄小珊，李黄幸，李晓璞，刘梦瑶，汤夏平，王梦真，张栋，赵博，赵晋超。没有他们，我的课余生活就毫无亮点可言了。可惜我毕业以后，大家又要天各一方了。验证了“人生就像茶几，上面摆满了杯具和餐具”的这句鲁迅先生说过的话(划掉)。

还有管系里几乎一切电子设备的David Rigby，真是老厉害了，感觉没有他解决不了的问题。

最后，十分重要的，我要感谢我的家人，几乎不干涉我做任何决定的父母和黄先生，任我走上了这条撞了南墙也不死心的路(后半句划掉)。没有他们的支持，我想我可能会更苗条一些(整句话划掉)。我和黄先生在高中时候因为天文奥赛，是互相见过面的，但是他脸盲应该不记得我，结果居然到这边读书之后又碰上了，真是验证了那句老话“冤家路窄”(整句话划掉)。说正经的，他们都是非常明智的人，总觉得我做什么都是对的，所以真是亲生的啊。我这样一个严肃认真且含蓄沉默的人，煽情的话也不多说了，他们都懂的。

然后没了。感觉我在你们心中伟岸的人设已然崩塌了……(手动再见)

Table of Contents

List of Figures

List of Tables

Chapter 1

Background

1.0.1 Motivation for White Dwarf Formation in Binaries

This section is the motivation and background for Chapter 2. With the recent direct detection of gravitational waves (Abbott et al. 2016), the era of gravitational wave astronomy has begun. Binary systems containing white dwarfs (WDs) are predicted to be strong gravitational wave sources in the mHz frequency range (Evans et al. 1987). One of the goals of the planned eLISA mission is to detect gravitational waves generated by inspiraling double WDs (Ruiter et al. 2010). Close accreting WD binary systems may also be the progenitors of type Ia supernova (Iben & Tutukov 1984). Among the brightest sources in the universe, type 1A supernovae are used as a standard candle (Sandage et al. 1996). This lead to the discovery that the universe is in an accelerating expansion era and the content is dominated by dark energy (Riess et al. 1998; Perlmutter et al. 1999). In spite of their importance in astrophysics, many aspects of WD binary formation and evolution are poorly understood. The goal of my work is to better understand the WD interior structure and evolution by studying the oscillation modes in the stars.

The motivation of the WD binary evolution project in Chapter 2 is the discovery of the pulsating helium core WDs with mass less than 0.2 $M_{\odot}$. In single star evolution, the lowest mass helium core WD that can be produced is $\simeq 0.4 - 0.45\,M_{\odot}$ depending on the strength of the stellar wind that exists on the red giant branch (RGB; D'Cruz et al. 1996). Thus, $M < 0.2M_{\odot}$ helium core WDs can only be produced in binary systems, and based on observations, the pulsating low-mass WDs are usually with another degenerate star (Hermes et al. 2012, 2013b,a).

1.0.2 Motivation for Orbital Decay by Tides

Stars greatly expand in radius when they leave the main sequence, eventually becoming hundreds of times bigger than their main sequence radius. Stellar or planetary companions with orbital separation less than a few AU can be engulfed by the giant star as it expands. Additionally, tides may cause the binary orbit to decay, bringing the companion inward to the star, rather than waiting for the star to expand to where it orbits. This orbital decay due to tides may significantly extend the orbital radius out to which planets are destroyed. If an observed giant star lacks close-in planetary companions, this may be due to orbital decay having already caused a merger to occur. In some rare cases binaries may be caught in the act of rapid orbital decay due to tides.

Once a merger occurs, if the substellar companion is massive enough, it may eject the hydrogen envelope of the RGB star (Nelemans & Tauris 1998). For a small planet, it will likely be completely disrupted by the star (Sandquist et al. 1998; Nordhaus et al. 2010) with little effect on the star.

Previous studies have focused on the final product of planetary systems, namely how far from the end-product WD that planets might be found. There are three

aspects to this problem. In addition to the expansion of the star and the decay of orbits due to tides, mass loss during the RGB and AGB causes the orbits of surviving planets to expand in proportion to the amount of mass lost from the star. Hence the expectation is that planets should only be found much further than the maximum radius attained by the star during the post-main sequence evolution.

Work by previous groups is as follows. Mustill & Villaver (2012) found that a Jupiter size planet initially outside 3 AU can survive through the entire nuclear evolution of its host star. The strong stellar wind in the AGB phase causes the orbit to expand, with the final result being an orbital radius 3 - 6 AU around the WD. Jupiter size planets within a few AU merge with the host star due to orbital decay caused by tidal friction. My results in Chapter 3 and 4 show that tides are also important in shrinking the orbit when the star is in the subgiant or RGB phase.

The motivation of the tides project is the orbital decay in progress for the WASP-12 system (Maciejewski et al. 2016; Patra et al. 2017), and many close binaries and star-planet systems with an orbital period within 20 days discovered by APOGEE survey (Troup et al. 2016). The tidal effect can significantly change the orbit of those systems. The fate of the systems is predictable by calculating the energy dissipation rate by tides.

1.1 Stellar Evolution

The projects described in Chapters 2-4 use the MESA stellar evolution code in order to study the structure and evolution of both single stars and stars in binary systems. In this section we briefly review the evolution of single stars (Kippenhahn & Weigert 1990). Chapter 4 will discuss extensions to the theory of single star evolution required when the stars in a binary interact. The focus will be on stars of mass $\lesssim 3\,M_{\odot}$.

Stars are formed from the collapse of a molecular cloud. During the pre-main sequence phase, contraction leads to an increasing temperature and fusion of hydrogen to helium is ignited when the central temperature reaches about 10^7 K. The subsequent phase of core hydrogen burning is called the main sequence phase, and is the longest nuclear burning phase. After the hydrogen in the core is exhausted, the star undergoes additional phases of evolution called the red giant branch (RGB), helium core burning, and the asymptotic giant branch (AGB). On the RGB, hydrogen burns in a shell outside the helium core, adding onto the mass of the core. The structure of the burning shell mainly depends on the mass of the core, and hence the star's luminosity and radius mainly depend on the helium core mass. The end of the RGB and the start of core helium burning depends on the mass of the star. Stars of mass $\lesssim 2.3\,M_\odot$ undergo the "helium core flash" in which helium is ignited explosively in degenerate conditions. Stars of mass $\gtrsim 2.3\,M_\odot$ ignite helium more smoothly under non-degenerate conditions. The helium in the core then burns to a mixture of carbon and oxygen. Lastly, the asymptotic giant branch is the phase in which core helium has been exhausted, and helium shell burning commences. The radius during the RGB and AGB is much larger than during the main sequence. When all the nuclear fuel has been depleted, and the temperature can no longer rise to burn any heavier elements, solar-type stars become white dwarfs (WDs). Although not discussed in this thesis, stars of mass $8M_\odot \lesssim M \lesssim 20M_\odot$ become neutron stars and high mass stars $M \gtrsim 20M_\odot$ form black holes (Fryer 1999).

Stellar structure is described by four equations. The first is the hydrostatic equilibrium equation, which describes how the inward gravity force is balanced by the outward pressure gradient force. The next equation integrates the interior mass versus radius. The third equation describes the sources and sinks of heat, such as heating

by fusion reactions, and cooling by optically thin emission of neutrinos. Outside the nuclear burning regions, the luminosity is constant as there is no energy generated there. The last equation describes the radial temperature gradient inside the star, which depends on whether radiation or convection (fluid motions) transports the heat outward through the star. If there are no chemical concentration gradients, then when the temperature gradient is greater than the adiabatic temperature gradient, the heat is carried out by convection. This is analogous to boiling water in a kettle on the burner. The three main microphysical inputs for stellar structure are the nuclear burning rates and the equation of state and opacity of the gas. Also important for the formation and evolution of white dwarfs is element diffusion, which leads to a stratification of heavy elements below light elements once diffusion has had time to act.

1.1.1 Low Mass Star Evolution

The Chapter 3 in this thesis is concerned with stars in the mass range 1.0 - 3.0 $M_{\odot}$, evolving from the MS to the RGB phase. For stars of mass 1.0 - 1.5 $M_{\odot}$ star, we also study the evolution until the white dwarf (WD) phase. All the simulations of the thesis are done with Modules for Experiments in Stellar Astrophysics (MESA), an open source stellar evolution and structure code (Paxton et al. 2011, 2013, 2015, 2018). Figure 1.1 shows the evolutionary track in log g ($g = GM/R^2$ is the surface gravity) and $T_{\rm eff}$ plane ($T_{\rm eff}$ is roughly the surface temperature) for a 1, 2 and 3 $M_{\odot}$ star, from pre-main sequence (PMS) to the RGB phase. All the tracks start at the top right of the figure, where the surface gravity of the star is small. Then the star collapses until the central hydrogen ignited and enters the MS phase. The location of the MS star on Figure 1.1 is at the bottom left of each evolutionary track. For the example

of the solar-type star, the coordinates of its MS phase are $(T_{\rm eff}, \log g) = (6000, 4.5)$. The main sequence is the most stable phase of the star during its entire evolution, where the luminosity, radius, $\log g$ and $T_{\rm eff}$ are nearly constant. A single solar-type star spends roughly 10 Gyr in this phase. The relation between the MS lifetime and mass is $t_{\rm MS}/(10\,{\rm Gyr}) \simeq (M/M_\odot)^{2.5}$ (Hansen & Kawaler 1994), so that 2 and 3 $M_\odot$ stars spend less time in the MS phase.

The difference between the evolution of low and high mass stars in the MS phase is that the nuclear energy is dominated by proton-proton chain (pp chain) for stars of mass $\lesssim 1.3\,M_\odot$, and the CNO cycle for stars greater than 1.3 $M_\odot$ (Salaris & Cassisi 2006). In the CNO cycle, carbon, nitrogen and oxygen isotopes are used as catalysts. Because the latter fusion reaction requires a higher temperature, the CNO cycle only occurs in higher mass stars. Furthermore, for low mass stars at the MS, it consists of a radiative core and a convective envelope. For star mass greater than 1.2 - 1.3 $M_\odot$, the the steeper temperature dependence from CNO burning implies that the star has a convective zone at the center. By coincidence, the convective envelope at the surface of the star is thick for $M \lesssim 1.3\,M_\odot$ and much thinner for more massive stars. The presence and extent of central and surface convection zones is an important factor for dynamical tide excitation of gravity waves (see Chapters 3 and 4).

The subgiant phase is between the MS and the RGB phase, and marks the transition from core to shell hydrogen burning. For star mass greater than 1.3 $M_\odot$, the cease of the central convective core means the beginning of the subgiant phase. This will be important in Chapter 3. At the RGB phase, the central hydrogen is exhausted and the shell hydrogen is ignited. The star's luminosity and radius increases significantly. On the evolutionary track of Figure 1.1, the star at the RGB phase moves to top right from the bottom left of its MS position. As its radius keeps expanding,

the log g is getting smaller. For a solar-type star at the late phase of RGB, its radius can be a hundred times greater than its MS radius. The Sun will engulf Mercury and Venus in the late RGB phase (Boothroyd & -Juliana Sackmann 1995; Schröder & Connon Smith 2008).

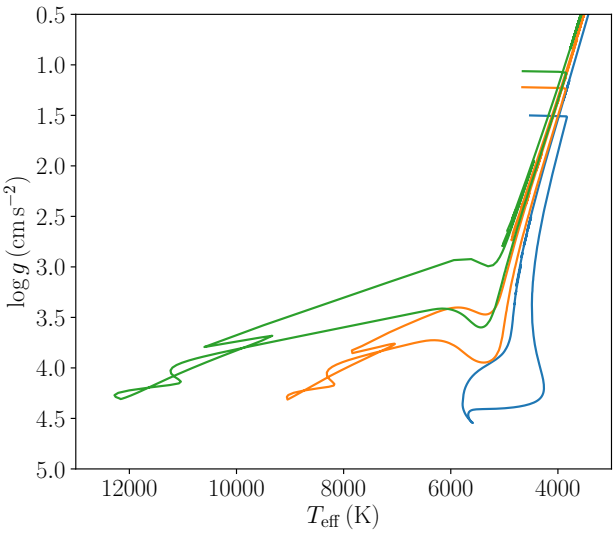

Fig. 1.1.— The evolutionary track for 1 $M_\odot$ (blue), 2$M_\odot$ (orange) and 3 $M_\odot$ (green) stars from Pre-MS to the RGB phase in the log g and $T_{\rm eff}$ plane.

1.1.2 Binary Evolution

The evolution of the two stars in a binary proceeds as for single star evolution until the two stars begin to interact. Either due to the orbital separation shrinking or due to the radius of the more massive star growing, one star will eventually begin to overflow its Roche lobe and lose mass. In this thesis, binary interaction enters in two different situations. In Chapter 2, we are interested in studying the formation of compact double WD binaries. The size of the orbit for the observed binaries can be much smaller than the size of the progenitor stars! Hence the stars must have

undergone a dramatic transformation from their zero-age main sequence appearance to their end result as compact objects (WDs). Next, in Chapters 3 and 4, the binary separation shrinks due to transfer of energy and angular momentum from the orbit to one of the stars. This eventually brings the star and its companion (a star or a planet) into contact. The evolution of these systems once they come into contact is thought to proceed by two possible scenarios, depending on whether mass transfer is stable or unstable.

Unstable mass transfer is defined by an exponential growth in mass loss rate to large values. It arises when mass loss leads to the Roche lobe radius moving deeper inside the stellar radius, so that mass loss accelerates with time (Hjellming & Webbink 1987; Soberman et al. 1997). Eventually the mass loss rate becomes so large that the entire envelope around the helium core is lost from the donor star and forms a common envelope (CE) around the donor core and the accretor (see Figure 1.2). Energy and angular momentum exchange between the two stars and the CE causes the orbit to shrink rapidly. The gravitational energy release powers the ejection of the envelope (Paczynski 1976). The end result is that the CE is fully ejected and the binary has a much smaller separation.

Stable mass transfer refers to a much lower and and more constant mass loss rate from the primary star. The mass loss rate is typically set by nuclear evolution of the primary or angular momentum losses from the orbit due to tides, stellar winds or gravitational radiation (Soberman et al. 1997). The simplest situation for the accretion ("conservative mass transfer") is to imagine mass transfer due to nuclear evolution of the primary, with no angular momentum losses, and the mass lost from the donor all landing on the accretor (Tout et al. 1997). In this case it is straightforward to show that the orbit first shrinks, until the donor and accretor have the

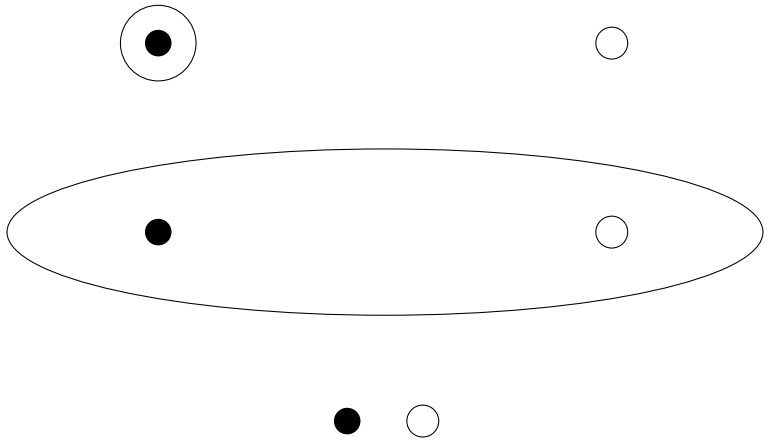

Fig. 1.2.— A schematic diagram showing the CE evolution. The black dot shows the degenerate core of the primary star with an envelope surrounding on the left. The secondary star shows in the circle on the right. In the CE theory, the mass of the companion keeps as a constant.

same mass, and then expands significantly. We found that conservative mass transfer can only produce helium core WDs greater than $0.2 M_{\odot}$, and hence cannot produce ELM WD with mass $M \lesssim 0.18\, M_{\odot}$. Further, the orbital periods resulting from conservative mass transfer are much longer than observed for the pulsating ELM WD. The problem is that the rate at which mass is lost from the surface is comparable to the rate at which the helium core grows and the core gets too big. The mass loss rate can be greatly sped up, as compared to the nuclear burning rate, by including "magnetic braking," which is the loss of angular momentum due to a stellar wind from the donor (Skumanich 1972; Smith 1979). Hence the donor loses mass simultaneously in a cold flow of gas through the L1 point in the Roche lobe overflow, as well as a magnetized outflow from the hot stellar corona. This stellar wind torque tries to spin down the star, but tides then synchronize the spin of the star, causing the orbit to lose angular momentum (Rappaport et al. 1983). A second ingredient commonly assumed is that some fraction of the mass which leaves the donor in the

Roche lobe overflow does not settle onto the accretor, but instead is ejected from the system, for example due to a disk wind. This loss of mass and angular momentum from the binary system are called "non-conservative mass transfer," and they may greatly change the evolution and fate of the binary (Tauris & van den Heuvel 2006). It is believed that the AM CVn systems contain a carbon-oxygen WD accreting from a hydrogen poor donor star, and are formed by the RLOF channel with magnetic braking (Podsiadlowski et al. 2003). Since they evolve to orbital periods lass than 1 hour, gravitational wave emission from the AM CVn's may be strong enough to be detected by eLISA (Nelemans et al. 2004). The cataclysmic variable (CV) binaries, where a WD accretes matter from an unevolved star, is also produced by the RLOF channel (Podsiadlowski et al. 2003). The formation of low-mass WD presented here is in between CVs and AM CVns, where the progenitor of the low-mass WD is somewhat evolved, with a small helium core at the beginning of the RLOF. The pulsations of these low-mass WDs may aid in understanding their structure and perhaps even allow us to discern their formation process.

The magnetic braking torque has been studied by both theoretical calculations as well as from observations of rotation rates of single stars. Observation of stellar rotation rates find that older stars tend to rotate much more slowly than younger stars, for low mass stars, while higher mass stars tend to retain rapid rotation rates over their lifetime (Kraft 1967). The observed spin-down of low mass stars is called "magnetic braking." The magnetized stellar wind of the rotating stars efficiently carries away angular momentum, spinning down the star. In a binary system, if one of the stars slows down its rotation due to stellar wind torques, tidal transfer of angular momentum shrinks the orbit (Rappaport et al. 1983). For the magnetic braking formation channel, we will show that the minimum WD mass is $\simeq 0.14\,M_{\odot}$.

1.2 Stellar Oscillations

Stellar oscillations serve two purposes in this thesis. For the ELM WD studied in Chapter 2, we are interested in using measured g-mode oscillation periods in order to carry out asteroseismic analysis for these stars to constrain the properties of their interiors. In Chapters 3 and 4, stellar oscillations are used in the context of tides. The g-modes can be excited by the tidal potential of the companion, transferring energy and angular momentum between the orbit and the star. This is called the "dynamical tide."

To give some background on the material on Chapters 2-4, here we give an introduction to free stellar oscillations in Section 1.2.1 and tidal forcing of stellar oscillations in Section 1.3.2.

1.2.1 Adiabatic Stellar Oscillation Equations

The equations describing stellar oscillation modes are the linearized equations of mass, momentum and energy conservation equation. These equations are solved assuming a spherically symmetric, time-independent background star, so that oscillations may be expanded in spherical harmonics $Y_{\ell m}(\theta, \phi)$ and with time dependence $\exp(-i\omega t)$. In this section we ignore dissipative processes, focusing on adiabatic fluid motion. The mass conservation equation, which is also called as the continuity equation, is

$$\frac{\partial \rho}{\partial t} + \boldsymbol{\nabla} \cdot (\rho \mathbf{v}) = 0 \tag{1.1}$$

where ρ is the mass density, t is time and $\mathbf{v}$ is velocity.

The momentum conservation equation, written in the Euler form, is

$$\rho\left(\frac{\partial}{\partial t}+\mathbf{v}\cdot\boldsymbol{\nabla}\right)\mathbf{v}=-\boldsymbol{\nabla}p+\rho\mathbf{g}, \tag{1.2}$$

here, p is the gas pressure and $\mathbf{g}$ is gravitational acceleration.

The energy equation, here represented by the first law in thermodynamics, is

$$T\frac{\mathrm{d}s}{\mathrm{d}t}=0, \tag{1.3}$$

where s is the entropy per unit mass. This equation says the entropy of a fluid element does not change in time. The comoving derivative is $d/dt=\partial/\partial t+\mathbf{v}\cdot\boldsymbol{\nabla}\mathbf{v}$.

The gravitational acceleration is $\mathbf{g}=-\boldsymbol{\nabla}\Phi$, where Φ is given by the Poisson equation,

$$\nabla^2\Phi=4\pi G\rho. \tag{1.4}$$

Here Φ is the gravitational potential and G is the gravitational constant.

In the linearized fluid equations, two types of the perturbations are used. Eulerian perturbations are at a fixed position $\mathbf{r}$, and are denoted by a symbol $\prime$. For example, the full density field is written as

$$\rho(\mathbf{r},t)=\rho_0(\mathbf{r})+\rho'(\mathbf{r},t). \tag{1.5}$$

On the left hand side, $\rho(\mathbf{r},t)$ is the full density in the perturbed star. On the right hand side, $\rho_0(\mathbf{r})$ is the background density at $\mathbf{r}$ and $\rho'(\mathbf{r},t)$ is the Eulerian perturbation at $\mathbf{r}$.

In the Lagrangian description, the perturbation is defined in the co-moving frame following the motion of the fluid, and denoted by the symbol δ. The Lagrangian

perturbation is related to the Eulerian perturbation as, e.g. (Aerts et al. 2010; Shapiro & Teukolsky 1983),

$$\delta\rho(\mathbf{r},t) = \rho'(\mathbf{r}_0,t) + \delta\mathbf{r}\cdot\boldsymbol{\nabla}\rho_0. \tag{1.6}$$

The "Lagrangian displacement vector" is defined as the displacement of the fluid element from its position in the background star to its position in the perturbed star. It is given by

$$\boldsymbol{\xi} = \delta\mathbf{r} = \mathbf{r} - \mathbf{r_0} = \xi_r\mathbf{e_r} + \boldsymbol{\xi_h}, \tag{1.7}$$

where in the second step we separated the vector into radial (ξ_r) and horizontal (ξ_h) components. Given the displacement vector, the velocity perturbation is

$$\mathbf{v}' = \dot{\boldsymbol{\xi}}, \tag{1.8}$$

where the dot denotes a time derivative.

Each quantity in Equations 1.1 - 1.4 may be written as the sum of a background star piece plus a first order perturbation piece, as in Equation 1.5. Plugging these expansions into Equations 1.1 - 1.4, the background star quantities may be canceled, as they satisfy the equations for a time-independent, spherically-symmetric background. Further, we ignore nonlinear terms here and focus on the linearized equations.

The linear perturbations may be expanded in terms of spherical harmonics, since the background star is spherically symmetric. For example, the density perturbation has the form

$$\rho'(r,\theta,\phi,t) = \sum_{\ell m}\rho'_{\ell m}(r,t)Y_\ell^m(\theta,\phi), \tag{1.9}$$

where $Y_\ell^m(\theta,\phi)$ is given by

$$Y_\ell^m(\theta,\phi) = (-1)^m \sqrt{\frac{2\ell+1}{4\pi}\frac{(\ell-m)!}{(\ell+m)!}} P_\ell^m(\cos\theta)\exp(\mathrm{i}m\phi) \tag{1.10}$$

and $P_\ell^m(\cos\theta)$ is the Associated Legendre polynomials (Courant & Hilbert 1953). Here θ is co-latitude and ϕ is longitude.

Vectors, such as the displacement vector, are expanded in the radial and poloidal spherical harmonic as

$$\boldsymbol{\xi} = \sum_{\ell m} \left(\xi_{r,\ell m}(r,t) Y_\ell^m(\theta,\phi)\mathbf{e}_r + \xi_{h,\ell m}(r,t) r \boldsymbol{\nabla} Y_\ell^m(\theta,\phi)\right). \tag{1.11}$$

The toroidal harmonic may be omitted here, as it would not provide any nonzero restoring forces. It must be included if the Coriolis force or magnetic fields are included.

Plugging the spherical harmonic expansions for each perturbation variable into Equations 1.1 - 1.4 and integrating each equation against a particular spherical harmonic leads to separable equations which only involve the spherical harmonic coefficients for a single value of ℓ and m. Further, the azimuthal symmetry implies the equations are independent of the spherical harmonic order m, but they do depend on the degree ℓ. The degree ℓ and order m of the spherical harmonic coefficients will be suppressed unless needed, so that $\rho'_{\ell m}(r,t) \to \rho'(r,t)$, etc.

For a time-independent background and free oscillations, we also assume that each perturbation variable oscillates harmonically, so that $\xi_r(r,t) = \xi_r(r)\exp(-i\omega t)$, etc. The oscillating factor $\exp(-i\omega t)$ may then be cancelled from the linearized equations, leading to equations that depend only on r. Here ω is the oscillation frequency.

The full non-linear fluid equations reduce to following linearized equations for adiabatic stellar oscillations.

The horizontal momentum equation

$$-\omega^2 \rho \xi_h = -\frac{p' + \rho \Phi'}{r}. \tag{1.12}$$

The continuity equation can be written

$$\frac{\mathrm{d}\xi_r}{\mathrm{d}r} = -\left(\frac{2}{r} + \frac{1}{\Gamma_1 p}\frac{\mathrm{d}p}{\mathrm{d}r}\right)\xi_r + \frac{1}{\rho c^2}\left(\frac{S_\ell^2}{\omega^2} - 1\right)p' + \frac{\ell(\ell+1)}{\omega^2 r^2}\Phi', \tag{1.13}$$

where $c = \sqrt{\Gamma_1 p/\rho}$ is the sound speed, S_ℓ is the Lamb frequency defined by $S_\ell^2 = [\ell(\ell+1)c^2]/r^2 = k_h^2 c^2$, and k_h is the horizontal wave number.

The radial momentum equation becomes

$$\frac{\mathrm{d}p'}{\mathrm{d}r} = \rho(\omega^2 - N^2)\xi_r + \frac{1}{\Gamma_1 p}\frac{\mathrm{d}p}{\mathrm{d}r}p' - \rho\frac{\mathrm{d}\Phi'}{\mathrm{d}r}, \tag{1.14}$$

where N^2 is the Brunt - Väisälä frequency, which is defined as

$$N^2 = g\left(\frac{1}{\Gamma_1 p}\frac{\mathrm{d}p}{\mathrm{d}r} - \frac{1}{\rho}\frac{\mathrm{d}\rho}{\mathrm{d}r}\right). \tag{1.15}$$

For adiabatic motion, constant entropy co-moving with the fluid element may be written in the form

$$\rho' = \frac{p'}{c^2} + \rho\frac{N^2}{g}\xi_r. \tag{1.16}$$

The definition of the Eulerian perturbation to the gravitational acceleration in the radial direction is

$$\frac{\mathrm{d}\Phi'}{\mathrm{d}r} = g'. \tag{1.17}$$

And the Poisson equation can be written

$$\frac{1}{r^2}\frac{\mathrm{d}}{\mathrm{d}r}\left(r^2\frac{\mathrm{d}\Phi'}{\mathrm{d}r}\right) - \frac{\ell(\ell+1)}{r^2}\Phi'. = 4\pi G\left(\frac{p'}{c^2} + \frac{\rho\xi_r}{g}N^2\right). \tag{1.18}$$

Equations 1.13 - 1.18 comprise the four equations for linearized stellar oscillations. Given boundary conditions, they give rise to an eigenvalue problem for the eigenfrequency ω and the eigenfunction $\xi_r(r)$, $p'(r)$, $\Phi'(r)$ and $g'(r)$.

For standing wave solutions trapped inside the star, the boundary conditions are as follows. At the star center ($r = 0$), g and $N^2 \to 0$ while ρ and c^2 are nearly constant. A number of terms then contain $1/r$ coefficients which diverge at the center. A finite solution is found by canceling these terms against each other. This is accomplished by the radial dependence $p' \propto r^\ell$, $\Phi' \propto r^\ell$, $g' \propto r^{\ell-1}$ and $\xi_r \propto r^{\ell-1}$. Numerically, these boundary conditions can be enforced a small distance away from the center by imposing the relation (Aerts et al. 2010)

$$\xi_r = \frac{\ell}{\omega^2 r}\left(\frac{p'}{\rho} + \Phi'\right). \tag{1.19}$$

Similarly, finiteness in the Poisson equation 1.18, requires

$$\frac{\mathrm{d}\Phi'}{\mathrm{d}r} = \frac{\ell\Phi'}{r}. \tag{1.20}$$

At the surface of the star ($r = R$), if we assume the scale height vanishes then waves are trapped within the star. Equations 1.13-1.18 again have divergent terms which must be cancelled against each other. Assuming that $c^2 \to 0$ and $N^2 \to \infty$, we must enforce

$$p' = \rho g \xi_r \tag{1.21}$$

at the surface. This equation looks like the standard plane parallel equation of hydrostatic balance for pressure change p' over a height ξ_r.

For the gravitational potential, there is no mass outside the star, and so the outwardly decreasing solution of the potential must be chosen to avoid divergences at infinite. This implies

$$\frac{\mathrm{d}\Phi'}{\mathrm{d}r} = -\frac{(\ell+1)}{r}\Phi'. \tag{1.22}$$

The four ordinary differential equations 1.13, 1.14 1.17 and 1.18 contains four variables ξ_r, p', Φ' and $g' = \mathrm{d}\Phi'/\mathrm{d}r$, and we have four boundary conditions from 1.19 to 1.22. The boundary value problem can be solved numerically by the shooting method (Unno et al. 1989). Outward integration from the singularities at the center and surface must be used. There are two free parameters needed to start the inward integration from the surface, and two needed to start the outward integration from the center. The four variables must be continuous at the fitting point somewhere in the middle of the star. This is only possible at certain frequencies ω called eigenfrequencies.

1.2.2 Mode Categories

There are three types of hydrodynamic waves in stars: acoustic, internal gravity, and surface waves. The surface wave is commonly referred to as the f-mode, which stands for fundamental. Standing acoustic waves are called p-modes, and standing internal gravity waves are g-modes.The acoustic wave has its restoring force from pressure and has frequencies $\omega \gtrsim (GM/R^3)^{1/2}$ so high that they can never be resonantly excited by the tidal gravity of an orbiting companion. The internal gravity waves are restored by buoyancy forces and have lower frequencies $\omega \lesssim (GM/R^3)^{1/2}$ which may

be excited by tides. In asteroseismic studies of the ELM WD, we will be concerned with *both* p and g-modes. The surface wave (or fundamental) is restored by gravity and has frequencies $\omega \sim (GM/R^3)^{1/2}$ (for $\ell = 2$). It generally has the largest, albeit nonresonant, response to the tidal force.

1.2.2.1 WKB Treatment of Acoustic and Gravity Waves

For short vertical wavelength waves, the full boundary value problem can be simplified by introducing the Wentzel-Kramers-Brillouin (WKB) approximation, which turns the four differential equations into algebraic equations to be solved for the vertical wavenumber $k_r^2(r)$ as a function of position. The WKB method lends considerable insight into both the dispersion relation as well as the regions of propagation and evanescence within the star.

The perturbed gravitational potential, Φ', is due to the Eulerian density perturbations ρ' created by the fluid flow. The perturbed gravitational acceleration $-\nabla\Phi'$ may be shown to be small compared to the perturbed pressure gradient $-\nabla p'/\rho$ for short wavelength waves. In the *Cowling approximation*, $\boldsymbol{\nabla}\Phi'$ is then ignored in the momentum equations. Equations 1.13 and 1.14 becomes

$$\frac{\mathrm{d}\xi_r}{\mathrm{d}r} = -\left(\frac{2}{r} - \frac{1}{\Gamma_1 H_p}\right)\xi_r + \frac{1}{\rho c^2}\left(\frac{S_\ell^2}{\omega^2} - 1\right)p' \tag{1.23}$$

and

$$\frac{\mathrm{d}p'}{\mathrm{d}r} = \rho(\omega^2 - N^2)\xi_r - \frac{1}{\Gamma_1 H_p}p' \tag{1.24}$$

where $H_p = -(\mathrm{dln}p/\mathrm{d}r)^{-1}$ is the pressure scale height.

For high radial order modes, the eigenfunction $\xi_r(r)$ varies slowly in amplitude as compared with phase. To solve for the phase of the wave, the WKB ansatz $f(r) \sim$

$f_0 \exp(\mathrm{i} \int k_r \mathrm{d}r)$ is inserted for all perturbation variables. The radial derivative then becomes $\mathrm{d}f/\mathrm{d}r \sim \mathrm{i}k_r f$. As $k_r \gg r^{-1}$ and $k_r \gg H_p^{-1}$, the radial derivative terms are much bigger than the background lengthscale terms. The first term on the right hand side of the Equation 1.23 and the second term in the right hand side of Equation 1.24 can then be ignored. Combining the two resulting first order equations gives the second order wave equation

$$\frac{\mathrm{d}^2 \xi_r}{\mathrm{d}r^2} = \frac{\omega^2}{c^2}\left(1 - \frac{N^2}{\omega^2}\right)\left(\frac{S_\ell^2}{\omega^2} - 1\right)\xi_r = -K_s(r)\xi_r. \tag{1.25}$$

In order for the wave to propagate, $K_s(r) = (N^2/\omega^2 - 1)(S_\ell^2/\omega^2 - 1)\omega^2/c^2$ must be positive. Therefore, we have a propagating wave function when either of the two following conditions are satisfied:

$$\omega^2 > N^2 \text{ and } \omega^2 > S_\ell^2 \tag{1.26}$$

or

$$\omega^2 < N^2 \text{ and } \omega^2 < S_\ell^2 \tag{1.27}$$

and the zones are called propagation zones. The place where $K_s(r) = 0$ is called the turning point and the place where $K_s(r) < 0$ is the evanescent zone.

The modes which satisfy Equation 1.26 are called p-modes, and they are mainly restored by pressure forces. P-modes can propagate in either convective or radiative zones. The modes which satisfy Equation 1.27 are called g-modes, and their restoring force is mainly buoyancy. These g-modes only propagate in radiative zones. For high-order p-modes, where $\omega \gg N^2, S_\ell^2$, the length of the radial wave vector can be

obtained by rewriting wave vector as a function of its radial and horizontal component

$$|\mathbf{k}|^2 = k_r^2 + k_h^2 = k_r^2 + \frac{\ell(\ell+1)}{r^2} = \frac{\omega^2}{c^2} \tag{1.28}$$

which gives

$$k_r^2 = \frac{1}{c^2}(\omega^2 - S_\ell^2). \tag{1.29}$$

This shows that the number of the radial nodes increases with mode frequency for the p-mode. Similarly, the radial wave number for high-order g-mode ($\omega \ll S_\ell^2, N^2$) can be written

$$k_r^2 = k_h^2\left(\frac{N^2}{\omega^2} - 1\right). \tag{1.30}$$

In contrast to the p-mode, the number of the radial nodes decreases with an increasing frequency for the g-mode.

1.2.2.2 Surface Wave

The fundamental mode (f-mode) is a non-WKB mode as it has no radial nodes. It is analogous to deep water waves in the ocean.

There is a simple solution for the f-mode in a constant density star which captures some of the main features seen in realistic stellar models. In the interior of the star, we approximate the density ρ as constant, the sound speed c is infinite and the Brunt $N^2 = 0$. This implies that $\rho' = 0$ in the interior. Further, we assume the motion is incompressible so that $\nabla \cdot \xi = 0$. The momentum equation is

$$\ddot{\boldsymbol{\xi}} = -\boldsymbol{\nabla}\left(p'/\rho + \Phi'\right). \tag{1.31}$$

Taking the divergence and using incompressibility gives

$$0 = \nabla^2 \left(p'/\rho + \Phi' \right). \tag{1.32}$$

The Poisson equation for $\rho' = 0$ is

$$\nabla^2 \Phi' = 0, \tag{1.33}$$

so that both p' and Φ' satisfy the Poisson equation. In the interior of the star, the finite solutions are then

$$p'(r) = p'(R) \left(\frac{r}{R} \right)^{\ell} \tag{1.34}$$

and

$$\Phi'(r) = \Phi'(R) \left(\frac{r}{R} \right)^{\ell}. \tag{1.35}$$

Using the momentum equation, the radial displacement is then

$$\xi_r(r) = \frac{\ell}{\omega^2 R} \left(\frac{p'(R)}{\rho} + \Phi'(R) \right) \left(\frac{r}{R} \right)^{\ell - 1}. \tag{1.36}$$

There are two boundary conditions at the surface. The first is the hydrostatic boundary condition $p'(R) = \rho g \xi_r(R)$. The second condition must take into account the gravitational potential perturbation by the deformed surface. For a density profile $\rho(r) = \rho \Theta(R - r)$ and the Eulerian density perturbation is $\rho'(r) = \rho \delta(r - R) \xi_r(r)$. This gives rise to the Poisson equation

$$\nabla^2 \Phi' = 4\pi G \rho' = 4\pi G \rho \delta(r - R) \xi_r(R). \tag{1.37}$$

Integrating the Poisson equation over a narrow region near the surface gives

$$-\left(\frac{2\ell+1}{R}\right)\Phi'(R) = 4\pi G\rho\xi_r(R) = \frac{3g}{R}\xi_r(R), \tag{1.38}$$

where we used the surface gravity $g = GM/R^2 = 4\pi G\rho R/3$. Combining the expressions relating $\xi_r(R)$, $p'(R)$ and $\Phi'(R)$ we find the dispersion relation

$$\omega^2 = \frac{g}{R}\frac{2\ell(\ell-1)}{2\ell+1}. \tag{1.39}$$

In the limit $\ell \gg 1$, this agrees with the usual deep water dispersion relation for water waves, $\omega^2 = gk_h$.

The exact dispersion relation shows that the $\ell = 0$ and $\ell = 1$ f-modes have zero frequency, and the quadrupole mode is the lowest order f-mode. If we had omitted Φ' from the momentum equation (the Cowling approximation), we would have incorrectly found that the dipole ($\ell = 1$) f-mode has a nonzero frequency. For $\ell \gg 1$, however, we find that $\Phi' \propto p'/\ell$, and the Cowling approximation is good even for f-modes.

1.3 Tidally Forced Waves

In star-planet systems as well as close stellar binaries, tidal friction may give rise to expansion or decay of the orbit by transferring angular momentum between the orbit and the stellar spins. Tidal effects depend on two considerations: (1) the amplitude of the tide raised by the companion, and (2) the amount of friction in the primary (which converts the kinetic energy in the tidal flow into heat). In this section, the physics of how tides make a spiral-in phase of the binary system is introduced.

Figure 1.3 shows how tides change the orbit and the spin of the star for Darwin's

tidal theory (Darwin 1879). The secondary object raises two tidal bulges onto the primary star. The combination of the force generated by the tidal bulge at the close side and the further side produces a torque. If the primary rotates more slowly than the orbital angular velocity, the torque spins up the primary and the orbit shrinks in order to conserve angular momentum. If the primary star rotates faster than the orbital angular velocity, the tidal torque acts to slow down the stellar spin and expand the orbit, similar to the Earth-Moon and Jupiter-Io systems (Goldreich & Soter 1966).

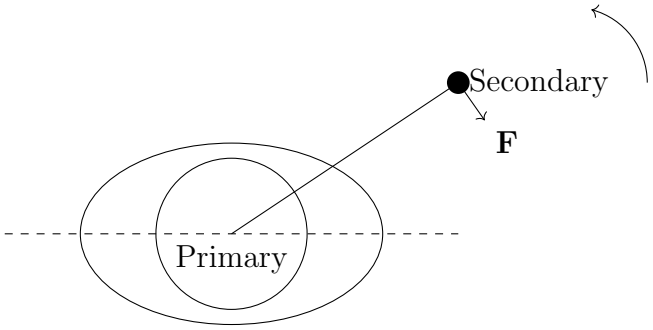

Fig. 1.3.— A schematic diagram showing the secondary star raise tides on the primary star. The secondary star rotate counterclockwise on this figure and raise two tidal bulges on the primary star that show in ecliptic. A lag angle is in between the solid line and the dashed line.

Most studies of tidal dissipation use the "equilibrium tide" approximation to the fluid flow (discussed below) and, following Darwin, parametrize the friction with a constant "lag angle" or "tidal Q" or "lag time." My work seeks to improve on both aspects of the problem by solving the boundary value problem for the forced tidal fluid flow as well as using physically motivated prescriptions for the dissipative effects.

For the adiabatic fluid motion, the equations of the tides in stars are very similar to the equations of the adiabatic oscillations, with an extra term tidal potential U in

describing the tidal acceleration $-\boldsymbol{\nabla}U$ due to the secondary. Define a new variable

$$\psi = \frac{p'}{\rho} + \Phi' + U = \omega^2 r \xi_h, \tag{1.40}$$

in terms of which Equation 1.13 becomes

$$\frac{\mathrm{d}\xi_r}{\mathrm{d}r} = -\left(\frac{2}{r} + \frac{1}{\Gamma_1 p}\frac{\mathrm{d}p}{\mathrm{d}r}\right)\xi_r + \frac{1}{c^2}\left(\frac{S_\ell^2}{\omega^2} - 1\right)\psi + \frac{\Phi' + U}{c^2}. \tag{1.41}$$

Similarly, Equation 1.14 becomes

$$\frac{\mathrm{d}\psi}{\mathrm{d}r} = (\omega^2 - N^2)\xi_r + \frac{N^2}{g}(\psi - \Phi' - U). \tag{1.42}$$

The Poisson Equation becomes

$$\frac{1}{r^2}\frac{\mathrm{d}}{\mathrm{d}r}\left(r^2\frac{\mathrm{d}\Phi'}{\mathrm{d}r}\right) = 4\pi G\rho\left(\frac{\psi - \Phi' - U}{c^2} + \frac{\xi_r}{g}N^2\right) + \frac{\ell(\ell+1)}{r^2}\Phi'. \tag{1.43}$$

The boundary conditions at the center of the star with the new defined quantity ψ is

$$\xi_r = \frac{\ell}{\omega^2 r}\psi. \tag{1.44}$$

At the star surface, the boundary conditions are the same with 1.21 and 1.22 (Unno et al. 1989).

The inclusion of the inhomogeneous forcing terms, involving the tidal potential $U \equiv U_{\ell m}(r)$, give rise to a boundary value problem in which the linear response to the forcing U at frequency ω may be found for each of the variables ξ_r, ψ, Φ' and g'. The true linear response is the solution to the boundary value problem (Goodman & Dickson 1998). However, often the solution can be idealized by two

different limits: the "equilibrium tide" and the "dynamical tide" (Cowling 1941; Zahn 1977). The equilibrium tide is the response that would occur if the star could instantly respond to the tidal force, and fluid inertia $\ddot{\xi}$ was unimportant. This solution is a good approximation when the tidal forcing frequency is smaller than the frequency of "important" modes. The equilibrium tide is often used as it gives a simple analytic solution. By contrast, the dynamical tide involves a wavelike response of the fluid, involving the excitation of a wave. This explicitly involves fluid inertia. There are two distinct limits for the response: standing waves, when dissipation is weak; and traveling waves, when dissipation occurs in less than a single group velocity travel time (Weinberg et al. 2012).

1.3.1 Equilibrium Tides

The equilibrium tide is formally the solution to the equations with ω set to $\omega = 0$ (Unno et al. 1989). From the horizontal momentum equation, $\omega^2 \xi_h = \psi/r$, this implies that $\psi = 0$ as well, and hence

$$\delta p = -\rho \left(\Phi' + U \right) . \tag{1.45}$$

The radial momentum equation then gives

$$\xi_r = -\frac{U + \Phi'}{g} \tag{1.46}$$

as long as $N^2 \neq 0$. In equilibrium tide flow, the fluid follows equipotentials of the full gravitational field. That is

$$\Phi(r) - g\xi_r + \Phi'(r) + U(r) \simeq \Phi(\mathrm{r}) \tag{1.47}$$

which implies

$$\xi_r = -\frac{\Phi' + U}{g}. \tag{1.48}$$

The continuity equation then gives

$$\frac{1}{r^2}\frac{\mathrm{d}}{\mathrm{d}r}(r^2\xi_r) + \boldsymbol{\nabla}_h \cdot \boldsymbol{\xi}_h = 0, \tag{1.49}$$

implying the motion is incompressible. Given the solution for ξ_r, this equation can be solved for the horizontal displacement as

$$\xi_h = -\frac{1}{\ell(\ell+1)r}\frac{d}{dr}\left[\frac{r^2}{g}\left(\Phi' + U\right)\right]. \tag{1.50}$$

While the equilibrium tide has zero divergence, the flow does containing shearing. This shearing leads to an important source of dissipation in stellar convection zones, where turbulent viscosity may give rise to rapid diffusion of momentum.

1.3.2 Dynamical Tides

The dynamical tide is the resonant excitation of internal gravity waves by the tidal force. Energy can be put into the wave through the work done, $-\rho\boldsymbol{\nabla}\cdot\dot{\boldsymbol{\xi}}$, by the tidal force. If dissipation is weak, the wave will be able to reflect many times between the inner and outer turning points and a standing wave will be formed. However, for efficient damping the wave energy dissipates as heat in the star before the wave has time to reflect back (Zahn 1977). The dissipation rate is maximized in the traveling wave limit.

An approximate solution is available in the traveling wave limit in the limit of short wavelengths (low forcing frequencies and wide orbits). In this limit, the work done

by the tide is highly oscillatory as the the wave is oscillatory but the tidal potential varies smoothly. Most of the energy is then put into the wave where the wavelength is longest, and this occurs near the turning point at the radiative-convective boundary. For an outer convective envelope, this implies a traveling wave fired inward toward the center of the star. An inward-going traveling wave boundary condition must be placed on this wave. The amplitude of the wave must also be matched to that in the convective envelope, which sets the wave amplitude.

In the above limit, the radial displacement satisfies the following wave equation near the turning point (Goodman & Dickson 1998)

$$\frac{\mathrm{d}^2\xi_r}{\mathrm{d}x^2} = x\xi_r \tag{1.51}$$

where a dimensionless radial coordinate is $x = (r - r_0)/\lambda$, and λ is the "Airy wavelength" given by

$$\lambda \equiv \left| \frac{\ell(\ell+1)}{\omega^2 r^2} \frac{\mathrm{d}N^2}{\mathrm{d}r} \right|_c^{-1/3} . \tag{1.52}$$

Using the two linearly independent solutions to the above Airy equation, the matching conditions are easily found. The resulting formula for the inward going wave luminosity is used in Chapters 3 and 4.

1.3.3 Wave Damping Mechanisms

The long-lengthscale equilibrium tide-type motions are most effectively damped by the turbulent eddies in stellar convective envelopes. The short-wavelength dynamical tide is evanescent in convection zones, but may be damped by radiative diffusion in radiative zones as well as by nonlinear fluid processes when the wave amplitude is large. In this section, the three damping mechanisms are discussed.

1.3.3.1 Turbulent Viscosity Damping

The tidally-induced fluid motions in the convection zone resemble the equilibrium tide, since gravity waves cannot propagate there. The left plot of Figure 1.4 shows the relative movement between shearing layers inside the convection zone. The upper layer moves towards the right, and the lower layer moves towards the left. If momentum can be exchanged between the two layers then the shearing will be damped.

First consider "molecular" viscosity due to a finite mean free path between collisions. As a particle in the lower layer moves one mean free path into the upper layer, it carries with it leftward momentum. When it moves to the upper layer, it decreases the momentum of the upper layer. During this process, a friction force and heat are produced, and are parametrized by a kinematic viscosity $\nu \sim v_{\rm th}\lambda$ with the units $\rm cm^2 s^{-1}$, like a diffusion coefficient. The characteristic lengthscale the particle moves is the mean free path λ, and its characteristic speed is the thermal velocity $v_{\rm th}$. Because the mean free path is so small in stars, molecular viscosity is typically too small to explain tidal evolution observations by many orders of magnitude.

The eddies carrying the heat out of the star in turbulent convection zones may serve a similar purpose as molecular viscosity. Instead of particles hopping mean free paths traveling at the thermal speed, consider fluid eddies in the stellar convective zone, which are shown as the circular arrows in the right panel of Figure 1.4. The shearing motions of the tidal flow may perform work on the eddies, implying an irreversible loss of energy from the tidal flow to the turbulent convective flow. For eddies of size $L \sim H_p$ and velocity $v_{\rm ed} \sim (F/\rho)^{1/3}$ (F is the heat flux), the turbulent viscosity $\nu \sim H_p v_{\rm ed}$ can be many orders of magnitude larger than molecular viscosity, and large enough to cause rapid tidal evolution in some circumstances (Zahn 1977). The energy dissipation rate due to turbulent viscosity can be estimated as $\dot{E} \sim$

$M_{\rm env}\nu|\boldsymbol{\nabla}\dot{\xi}|^2$, where $M_{\rm env}$ is the mass of the stellar convective zone.

One issue that arises in practice is that it is only *resonant* eddies, with turnover times comparable to the tidal forcing period, that are effective in damping the tidal shearing motions (Goodman & Oh 1997; Penev et al. 2009, 2011; Ogilvie & Lesur 2012). Hence the "standard" turbulent viscosity, using the largest eddy sizes $\sim H_p$ and velocities $v_{\rm ed}(H_p)$, are not applicable in many situations where the orbital period is shorter than the large eddy turnover time (e.g. 1 month for the Sun). The theory of "reduced viscosity" attempts to use not the largest eddies, but smaller resonant eddies which turnover with timescales comparable to the orbital period. As this is a complicated and unsolved problems, we summarize the two most commonly used models for reduced viscosity.

Zahn (1966, 1989) substitutes the mixing length term in computing the kinematic viscosity, with the distance that the biggest eddy covered during half of the forcing period to get the viscosity, $\nu_{\rm ZN} = \nu(P_f/\tau_{\rm ed})$, here $\tau_{\rm ed}$ is the eddy turnover time for the biggest eddy. Alternatively Goldreich & Nicholson (1977) and Goldreich & Keeley (1977) use the eddies with a turnover time equivalent to the forcing period $P_{\rm f}$ in computing the viscosity. Developed from the Kolmogorov spectrum, which gives the relation between energy and the size of the eddy, the relation between the eddy

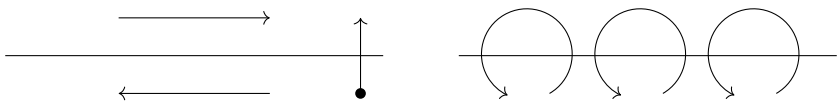

Fig. 1.4.— A schematic diagram showing the convective damping. The horizontal lines marks the upper and lower layer inside the star convective zone. The test particle is shown as a black dot. The eddies are displayed as counterclockwise arrows on the right.

velocity with a size $l_{\rm GN}$ and its length scale is

$$v_{\rm ed}(l_{\rm GN}) \sim (l_{\rm GN})^{1/3}, \tag{1.53}$$

which means the eddy velocity is proportional to the length scale to the power of 1/3. Then the eddy turnover time for the eddy with a size $l_{\rm GN}$ is

$$\tau_{\rm ed}(l_{\rm GN}) = P_{\rm f} = \frac{l_{\rm GN}}{v_{\rm ed}(l_{\rm GN})} \sim \tau_{\rm ed}\left(\frac{l_{\rm GN}}{l}\right)^{2/3} \tag{1.54}$$

The derived viscosity for Goldreich and Nicholson's theory $\nu_{\rm GN}$ is then

$$\nu_{\rm GN} \sim v_{\rm ed}(l_{\rm GN}) \times l_{\rm GN} \sim \nu_{\rm std}\left(\frac{l_{\rm GN}}{l}\right)^{4/3} \sim \nu_{\rm std}\left(\frac{P_{\rm f}}{\tau_{\rm ed}}\right)^{2}. \tag{1.55}$$

To summarize, For Zahn's theory, the viscosity is reduced linearly with orbital period. For Goldreich and Nicholson's theory, there is a quadratic reduction with orbital period factor. The energy dissipation rate of the equilibrium tides is therefore expected to be greatly reduced for close systems.

1.3.3.2 Radiative Damping

In radiative zones, hot and cold regions are created by the compression and rarefaction of waves. Thermal diffusion due to heat carried by photons may then allow heat to flow from the hot to the cold regions, damping the wave. Radiative damping is more important for shorter lengthscale waves, as then the heat does not have to diffuse as far (Zahn 1975; Goodman & Dickson 1998).

Since the dynamical tide can have very short lengthscales, for low frequency gravity waves, radiative damping may be significant. For a traveling wave suffering strong thermal diffusion, the wave energy converts to heat during the propagation, even be-

fore it reaches the inner turning point. The thermal diffusion is particularly important in the electron degenerate cores of RGB stars. The decrease in wave energy may be parametrized as $\sim \exp(-\alpha)$ where α represents the fraction of wave energy damped in one group travel time (Goodman & Dickson 1998). Results are presented for α in Chapter 4.

1.3.3.3 Nonlinear Damping

As ocean waves approach the shore and the water depth decreases, their amplitude increases. When the wave height (amplitude) becomes comparable to the wavelength (distance between crests), the wave breaks nonlinearly and deposits its energy locally in the form of shorter wavelength waves and heat. The same process happens for the dynamical tide in stars.

In RGB stars, the dynamical tide is excited at the radiative-convective boundary and propagates inward. As the wave approaches the center, moving into a region of smaller area ($4\pi r^2$), in order for the wave luminosity to remain constant the wave amplitude must increase. When the wave amplitude (ξ_r) becomes comparable to the vertical wavelength ($2\pi/k_r$) the wave energy is locally converted into heat, and the traveling wave limit is applicable (Kumar & Goodman 1996; Goodman & Dickson 1998; Barker & Ogilvie 2010; Weinberg et al. 2012). In Chapters 3 and 4, the traveling wave luminosity at the radiative-convective boundary may be used to compute the nonlinearity $k_r\xi_r$ in the radiative zone, and the condition for nonlinear wave breaking is checked to see when the traveling wave limit may be used.

Chapter 2

Formation of the Extremely Low-Mass White Dwarf Binaries

This chapter is based on the publication Sun & Arras (2018).

2.1 Introduction

Extremely low-mass white dwarfs (ELM WDs) are here defined as helium-core WDs with masses $M \lesssim 0.18\,M_\odot$, sufficiently low that no hydrogen shell flashes occur during the WD cooling stage. More massive WDs have shell flashes, which quickly decrease the mass of the hydrogen-rich envelope. The thicker envelopes of ELM WDs allow for significantly higher stable hydrogen burning rates, keeping these lower mass stars more luminous than their slightly more massive counterparts (Driebe et al. 1999).

Helium core WDs can in principle be formed through single star evolution, for sufficiently small mass that helium core ignition is avoided. Large helium core WDs of mass $M \lesssim 0.45\,M_\odot$ may be produced in less than 13.7 Gyr (D'Cruz et al. 1996) if enhanced mass-loss rates are assumed on the red giant branch (RGB). However,

far larger mass-loss rates would be needed to strip more than $0.8\,M_\odot$ on the RGB to uncover a helium core mass $M_\mathrm{c} < 0.2\,M_\odot$ starting from a $M_i \simeq 1\,M_\odot$ zero-age main sequence (ZAMS) star. Further, the main sequence (MS) evolution time for ZAMS masses $M_\mathrm{i} \lesssim 0.2\,M_\odot$ is $t_\mathrm{ms} \gtrsim 1000\,\mathrm{Gyr}$, and hence, in practice, ELM WDs can only be produced through binary evolution, either by stable Roche-lobe overflow (RLOF) or unstable mass transfer (MT) and a common envelope (CE) inspiral.

ELM WDs have been observed to pulsate with g and p-mode oscillations (Hermes et al. 2012, 2013b,a), opening up the possibility of probing the interiors of these exotic stars with seismology. One question is whether the two different formation channels can be distinguished through seismology. Since the structure of these objects is particularly simple, with a helium core and a thick, hydrogen-rich envelope, there are in principle fewer parameters required to characterize the star than for carbon-oxygen core DA and DB WD pulsators. One complication is that, for the effective temperature T_eff range of observed pulsators, there may be insufficient time to establish diffusive equilibrium throughout the star (Córsico & Althaus 2014). This complicates the calculation of stellar models, because time-dependent diffusion must be included, but also provides an additional opportunity for changing composition profiles to affect the mode periods.

A number of ELM WDs were recently discovered by the ELM, SPY and WASP surveys (Koester et al. 2009; Brown et al. 2010, 2012, 2013, 2016; Maxted et al. 2011; Kilic et al. 2011, 2012; Gianninas et al. 2015). Follow-up observations of ELM survey candidates allowed Hermes et al. (2012) to discover the first pulsating ELM WD, SDSS J184037.78+642312.3. Subsequently, the 2nd and 3rd pulsating helium WDs, SDSS J111215.82+111745.0 (J1112) and SDSS J151826.68+065813.2, were discovered with seven oscillation frequencies, respectively. For J1112, two modes with shorter periods

were suggested as possible p-mode oscillations (Hermes et al. 2013b). This is the only known WD with p-mode pulsations. There are currently seven known pulsating ELM WDs (see Table 2.1). The $T_{\rm eff}$ range of the seven stars is $7,890 < T_{\rm eff}/{\rm K} < 9,560$, and the surface gravity range is $5.78 < \log_{10}(g/{\rm cm\ s^{-2}}) < 6.68$. The range of observed pulsation periods for the seven objects is from 1184 to 6235s (Hermes et al. 2013a; Bell et al. 2015; Kilic et al. 2015). Pulsations are also observed in pre-ELM WDs WASP J1628+10B and WASP J0247-25B, which have not yet cooled off to the WD cooling track. An interesting point in regards to the driving of the observed modes by the κ mechanism is that the driving by the helium partial ionization zone may indeed explain the observed pulsations (Córsico et al. 2016), but it was necessary to turn off diffusion, otherwise helium would settle down below the driving region. Models which include element diffusion (Istrate et al. 2016) must include a source of mixing to keep the helium lofted up in the driving region.

The expected range of oscillation mode periods of helium WDs with mass $M \lesssim 0.2 M_{\odot}$ was examined by Steinfadt et al. (2010), who showed that the smaller WD mass and larger radius lead to mode periods as much as a factor of 2 longer than the carbon-oxygen core WD with $\log_{10}(g/{\rm cm\,s^{-2}}) \approx 8$. They also showed that g-mode pulsations may contain most of their energy in the helium core, so that the mode periods may be sensitive to $M_{\rm c}$. Córsico and Althaus (2014; hereinafter CA) studied the two short period p-modes of J1112, finding that the model p-modes nearly match the observed short period modes for a low-mass WD with $M \simeq 0.16\ M_{\odot}$, but the implied surface gravity was then well below that inferred from spectra. Subsequently Tremblay et al. (2015) used three-dimensional (3-D) hydrodynamic simulations of WD atmospheres, and fitting these new model atmospheres implied significantly different $\log g$ for cool DA WDs, as much as 0.35 dex, closer than that required by the short

p-mode periods. At present, the minimum mass ELM WD from the ELM survey is $M = 0.14\ M_{\odot}$ (Brown et al. 2016) with a $\log_{10}(g/\mathrm{cm\,s^{-2}}) = 5.5$. One question addressed in this paper is the minimum mass for the ELM WD from binary evolution.

There are seven observed pulsating WDs with mass lower than $0.2 M_{\odot}$. Table 2.1 gives their parameters from observations. The mass estimates of the ELM WDs and their companions are shown in columns 2 and 6. Except J1618+3854, all other $\log g$ is given by 3-D atmosphere simulations (Tremblay et al. 2015; Kilic et al. 2015). Three of the systems have no radial velocity detection of a companion.

Section 2.2 discusses a promising formation channel, Roche-lobe overflow including orbital angular momentum losses due to magnetic braking. Binary evolution and ELM formation results from this model are presented in Section 2.3. Discussion and conclusions are given in Sections 3.4 and 2.5. Appendix 2.6 shows that the minimum WD mass produced through conservative mass transfer is larger than the ELM WD mass range. Appendix 2.7 shows that formation of an ELM WD by CE evolution tends to produce very close binaries, which may merge in many cases.

2.2 ELM formation through magnetic braking

The Cataclysmic Variable (CV) model of ELM WD formation in this paper assumes that the progenitor of the ELM WD was the initially less massive star. The initially more massive star formed a WD companion.

From the discussion in Appendix 2.6, magnetic braking is key to form ELM WDs so that the envelope is stripped before the core can grow too large. This section starts with a brief summary of previous work on CV binaries with both unevolved ($M_{\rm c} = 0$) and slightly evolved ($M_{\rm c} \lesssim 0.05\,M_{\odot}$) stars transferring mass to a WD.

The ELM formation model presented here is the extension to CVs with higher core masses in the range $0.06 \lesssim M_{\rm c}/M_{\odot} \lesssim 0.16$. In this model, the ELM WD started as the donor star, and appeared as a $M < 0.18\,M_{\odot}$ WD at the end of MT. The lower core mass end for the ELM WD comes from the requirement that MT ends before the AM CVN phase, so that the ELM WD may be observed as a pulsator. The upper core mass limit for the ELM WD is set by requiring that no shell flashes occur on the WD cooling track, allowing thick surface hydrogen layers and long-lived stable nuclear burning.

Canonical CV evolution of unevolved donor stars with masses $M_{\rm d} \lesssim 1\,M_{\odot}$ uses magnetic braking laws calibrated by observations of the spin-down of single stars to understand binary evolution. Since the thermal time is shorter than the mass-loss timescale for these systems, the evolution is relatively insensitive to the initial donor mass, and the evolution of different donor masses converges to the same track at shorter $P_{\rm orb}$. The well-known CV period gap, the scarcity of accreting systems in the range $2 < P_{\rm orb}/{\rm hr} < 3$, is understood as the donor shrinking inside the Roche lobe when the magnetic braking torque decreases sharply. The physical origin of the angular momentum loss rate by magnetic braking $\dot{J}_{\rm mb}$ was initially thought to be the disappearance of the tachocline as the star became fully convective, although it was later realized that even late M stars may be able to generate large magnetic fields which can support a comparable level of coronal activity required to generate a magnetic wind (Kraft 1967; Skumanich 1972; Spruit & Ritter 1983; Browning 2008). Regardless of the origin of the torque decrease, it is implemented in evolutionary codes by turning $\dot{J}_{\rm mb}$ off by hand when the donor star becomes fully convective. MT then resumes at $P_{\rm orb} \simeq 2\,{\rm hr}$ when gravitational wave torques shrink the orbit and bring the donor back into contact. The gradual lengthening of the thermal time as the

hydrogen burning limit is approached changes the structure of the donor from that of a low-mass MS star to a brown dwarf responding adiabatically to mass-loss. As a result the donor star expands upon losing mass, and the orbital evolution switches from contraction to expansion.

The evolution of CVs with slightly evolved donors $M_{\rm c} \lesssim 0.05\,M_{\odot}$ has been discussed by Podsiadlowski et al. (2003) and van der Sluys et al. (2006). They showed that systems with evolved donors can form short-period AM CVn systems for small $M_{\rm c}$, and also dominate the CV population at long orbital periods $P_{\rm orb} \gtrsim 5\,{\rm hr}$ for larger $0.03 \lesssim M_{\rm c}/M_{\odot} \lesssim 0.05$. A bifurcation period at $16 \lesssim P_{\rm orb}/{\rm hr} \lesssim 22$ separates the systems which move to shorter periods from those that expand. In the period range $1 \leqslant P_{\rm orb}/{\rm hr} \leqslant 5\,{\rm hr}$ the CV population is dominated by unevolved stars.

Podsiadlowski et al. (2003) discussed that, as compared to unevolved donors, care must be taken in the magnetic braking torque when the donor's convective envelope becomes thin. The commonly used $\dot{J}_{\rm mb}$ formulae have been calibrated for stellar masses less than about $1\,M_{\odot}$, and do not take into account the reduced magnetic torque for sufficiently thin surface convection zones. The well known Kraft break (Kraft 1967) in the rotation rates of single stars at mass about $1.3\,M_{\odot}$ divides the higher-mass, rapid rotators from the lower-mass slow rotators, indicating a dramatic reduction in $\dot{J}_{\rm mb}$ when the surface convection zone becomes small. For evolved donors, this reduction is key to the formation of ELM WDs. Due to the degenerate helium core, these stars always have radiative cores, and hence $\dot{J}_{\rm mb}$ would not undergo the same drastic reduction as for unevolved donors. However, MT gradually sheds the envelope until it becomes so thin that the shell burning strongly decreases, with an associated shrinking of the convective envelope. This tends to cause the evolved donor to fall out of contact. If, in addition, a prescription for reduced $\dot{J}_{\rm mb}$ at small

convective envelope mass is included then a long non-accreting phase in which the donor star emerges as an ELM WD may result. Systems with small $M_{\rm c}$ which fall out of contact at small $P_{\rm orb}$ may be driven back into contact by gravitational wave losses, while those with larger $M_{\rm c}$ are sufficiently distant that they don't have time to come back into contact in a Hubble time.

The magnetic braking law chosen here is the same as used for unevolved donors, with a reduction in torque for small convective envelopes. The reasonableness of this prescription can be judged by the agreement of the model $P_{\rm orb}$, $\log_{10}\,g$ and $T_{\rm eff}$ with observations.

2.2.1 Description of the Simulations

Binaries are evolved using the "binary_donor_only" option in the Modules for Experiments in Stellar Astrophysics code (MESA, version 8845; Paxton et al. 2011, 2013, 2015), which evolves the structure of the donor star and orbit in time, but treats the accretor as a point mass. Mass transfer is assumed to be fully non-conservative (MESA parameter mass_transfer_beta = 1), so the accretor mass $M_{\rm a,i}$ is a constant in time and mass-loss from the binary is assumed to take place in a fast wind from the accretor. The physical basis for this assumption is that accretion disk winds may limit the mass that falls on to the accretor, and nova explosions may remove the accreted mass.

The mixing length parameter is set to $\alpha_{\rm ML} = 1.9$. The ZAMS metallicity of all stars is $Z = 0.01$, which is characteristic of the disk stars in the Galaxy (Bensby et al. 2014). As stars evolve faster for lower metallicity with the same star mass (Istrate et al. 2016), this metallicity choice helps accelerate the production of a WD within the age of the Galaxy. The nuclear burning network used is "pp_and_cno_extras", which

includes ^{1}H, ^{3}He, ^{4}He, ^{12}C, ^{14}N, ^{16}O, ^{20}Ne, ^{24}Mg and extended networks which comprise the pp-chain and CNO cycle. Element diffusion is included over the entire evolution, starting from ZAMS end extending through the WD cooling track. This setting is crutial in regards to the critical mass at which H flashes occur, as well as to the number of flashes before the WD cooling as found by Istrate et al. (2016). The setting "diffusion_use_cgs_solver = .true." is used to allow for electron degeneracy in the diffusion physics. Five classes of elements, ^{1}H, ^{3}He, ^{4}He, ^{16}O, ^{56}Fe, are evolved. Helium core masses, $M_{\rm c}$, reported here are computed as the mass interior to the point where the mass fraction of ^{1}H is 1% that of ^{4}He.

The total orbital angular momentum, J, evolves through torques due to magnetic braking ($\dot{J}_{\rm mb}$), gravitational waves ($\dot{J}_{\rm gr}$, Landau & Lifshitz 1975) and mass-loss from the binary ($\dot{J}_{\rm ml}$)

$$\dot{J} = \dot{J}_{\rm mb} + \dot{J}_{\rm gr} + \dot{J}_{\rm ml}. \tag{2.1}$$

Angular momentum loss from the binary due to a fast wind in the viscinity of the accretor is (Tauris & van den Heuvel 2006)

$$\dot{J}_{\rm ml} = J\ \frac{M_{\rm d}\dot{M}_{\rm d}}{M_{\rm a}(M_{\rm d}+M_{\rm a})}. \tag{2.2}$$

The mass-loss torque $\dot{J}_{\rm ml}$ is important during the thermal timescale mass transfer TTMT, when $M_{\rm d} \gtrsim M_{\rm a}$ and the mass-loss rate of the donor $\dot{M}_{\rm d}$ is high. Thereafter, $\dot{J}_{\rm mb}$ takes over until the convection zone thins. The gravitational wave torque $\dot{J}_{\rm gr}$ is important for short periods $P_{\rm orb} \lesssim 3\,{\rm hr}$, and is the dominant torque at the second phase of MT at $P_{\rm orb} \lesssim 1\,{\rm hr}$.

For thick convection zones with mass fraction $q_{\rm conv} > 0.02$, the magnetic braking formula of Rappaport et al. (1983) is used. MESA's implementation is to set $\dot{J}_{\rm mb} = 0$

when the fraction of mass in the convection zone $q_{\rm conv} > 0.75$ to implement the above-mentioned reduction at small stellar mass. To take into account reduced magnetic braking when the surface convection zone is thin, the ansatz from Podsiadlowski et al. (2002) is that $\dot{J}_{\rm mb}$ is reduced by an exponential factor as the convection zone mass becomes small. The end result used in the simulations is then

$$\begin{aligned} \dot{J}_{\rm mb} &= -3.8 \times 10^{-30} M_{\rm d} R_\odot^4 \left(\frac{R_{\rm d}}{R_\odot}\right)^\gamma \omega^3 \\ &\times \begin{cases} 0, & 1 > q_{\rm conv} > 0.75 \\ 1, & 0.75 > q_{\rm conv} > 0.02 \\ e^{1-0.02/q_{\rm conv}}, & q_{\rm conv} < 0.02 \end{cases} \end{aligned} \tag{2.3}$$

where $\dot{J}_{\rm mb}$ is in CGS units $\mathrm{g\,cm^2\,s^{-1}}$, magnetic braking index $\gamma = 4$ was used in the calculations, $\omega = 2\pi/P_{\rm orb}$ is the orbital angular velocity in $\mathrm{rad\,s^{-1}}$, $R_{\rm d}$ is the donor star radius. The mass fraction $q_{\rm conv} = 0.02$ is for the current solar convection zone and so magnetic braking is suppressed on the MS for more massive stars. Because the donors are evolved, their radii shrink less than for unevolved donors and there is only a weak dependence on γ. Calculations with $\gamma = 3$ and 4 gave similar results.

A side effect of the reduced $\dot{J}_{\rm mb}$ at small $q_{\rm conv}$ is that donors with mass $1.3 \lesssim M_{\rm d}/M_\odot \lesssim 1.4$, which have small magnetic braking on the MS, can have sufficient magnetic braking as evolved donors, with thicker convection zones that they work well as the progenitors of ELM WDs. Their MS lifetime is much shorter than a $0.9 \leqslant M_{\rm d}/M_\odot \leqslant 1.1$ donor, so this leaves more time for the WD to cool to small $T_{\rm eff} \lesssim 9000\,\mathrm{K}$ and enter the blue edge of the instability strip. Simulations of donors with larger masses $M_{\rm d} \gtrsim 1.5\,M_\odot$ had difficulty forming an ELM WD because $M_{\rm c} \gtrsim 0.1\,M_\odot$ at the end of the MS which, when combined with core growth during the accretion phase, makes them too large to be the ELM WD with $M < 0.18\,M_\odot$.

Furthermore, the orbits are much wider than for the $1.0 \leqslant M_{\rm d}/M_{\odot} \leqslant 1.4$ cases.

Simulations in which the MT rose sharply and exceeded $|\dot{M}_{\rm d}| > 10^{-3}\,M_{\odot}$ yr^{-1} were stopped and labeled as exhibiting unstable MT. This occurs if the initial mass ratio $q_{\rm i} = M_{\rm d,i}/M_{\rm a,i}$ is too large, where $M_{\rm d,i}$ is the initial donor star mass, $M_{\rm a,i}$ is the initial accretor mass, and is exacerbated by wider orbital separations such that the donor was well up the giant branch when MT commenced. As discussed in Appendix 2.7, unstable MT and CE may lead to merging for the $M_{\rm c} \lesssim 0.1\,M_{\odot}$ here.

In our model, the ELM WD progenitor is assumed to be the initially less massive star, and the initially more massive star becomes the ELM WD companion, itself a WD. The initially more massive star is assumed to form a WD through a CE phase, because short orbital periods from 1 to 3 days are required in the second phase of MT to form the ELM WD. Let M_1 be the mass of the initially more more massive star, M_2 the mass of the initially less massive star, and $a_{\rm CE,i}$ the initial semi-major axis before the CE. Notice that the subscript "1", "2" and "CE" are only used in this section, and indicate the star parameters before the stable RLOF phase. For a wide initial orbit, a core mass $M_{1,\rm c}$ is formed in star 1, and by removing the envelope, $M_{1,\rm c}$ is the mass of the ELM companion. Applying the CE energy equation (Equation 2.8 in the appendix), and expressing the answer in terms of the post-CE (but pre-magnetic braking) orbital period $P_{\rm CE,orb,f}$, gives

$$\left(\frac{G(M_{1,\rm c}+M_2)P_{\rm CE,orb,f}^2}{4\pi^2}\right)^{1/3} = R_1(M_{1,\rm c})\times\left(\frac{M_{1,\rm c}M_2}{(2/\alpha\lambda)M_1(M_1-M_{1,\rm c})+M_1M_2r_{\rm L}(M_1/M_2)}\right). \tag{2.4}$$

with the appropriate $R_1(M_{1,\rm c})$ relation for each core mass range, this equation can be solved for $P_{\rm CE,orb,f}$ during the evolution, where $P_{\rm CE,orb,f}$ is the post-common envelope (but pre-magnetic braking) orbital period, $\lambda \simeq 1$ is a mass-dependent factor describing the binding energy, α is the efficiency of tapping orbital energy to remove

the envelope, and $r_{\rm L}a$ is the effective radius of the Roche lobe, and $r_{\rm L}$ is a parameter defined in Eggleton (1983). MESA models for $M_{1,\rm i}$ =1, 2, 3, 4, 5 $M_\odot$ were used to find R_1, $M_{1,\rm c}$ and M_1 during the evolution. The radius grows non-monotonically, so this leads to gaps in $M_{1,\rm c}$ over regions where the radius decreases below its maximum value.

Figure 2.1 shows numerical solutions of Equation 2.4 for companion mass $M_{1,c}$ as a function of $P_{\rm CE,orb,f}$. The ELM WD progenitor mass has been fixed at $M_2 = 1.3\,M_\odot$, and five different M_1 have been used to give the different lines. The product $\alpha\lambda$ is set to 2 for convenience. There is a general trend that $M_{1,\rm c}$ must be larger for larger orbital period or M_1, in order that the orbital energy release can balance the binding energy. During the second phase of MT, the companion is the accretor and so $M_{\rm a,i} = M_{1,\rm c}$, and the progenitor of the ELM WD is the donor, so $M_{\rm d,i} = M_2$.

The separation at the onset of the RLOF should be slightly greater than 5 $R_\odot$ to form an ELM WD. If $M_{1,\rm c}$ is fixed at 0.6 $M_\odot$ with $M_2 = 1.3\,M_\odot$ and the separation after the CE $a_{\rm CE,f} = 5R_\odot$, there are still two free (but not completely free) parameters M_1 and the orbital period before the CE $P_{\rm CE,i}$. Moreover, M_1 is greater than M_2 because the massive star evolves first. This can lead to a CE phase. And M_1/M_2 is greater than one to have unstable MT followed by a CE phase (Woods & Ivanova 2011). For $M_1 = 2$ $M_\odot$, $P_{\rm CE,i}$ is 7.6 days.

2.3 results on binary formation

2.3.1 The Fiducial Case

Figure 2.2 displays evolution tracks in the $\log_{10}\,g$ versus $T_{\rm eff}$ plane for the fiducial case with $M_{\rm d,i} = 1.3\,M_\odot$ and (constant) accretor mass $M_{\rm a,i} = 0.6\,M_\odot$. The entire

Table 2.1: Properties of the seven pulsating ELM WDs. The error bars of $\log_{10} g$, $T_{\rm eff}$, Mass Function, $M_{2,\rm min}$ and $P_{\rm orb}$ are in Sun & Arras (2018).

Object	M ($M_\odot$)	$\log_{10} g$ (cm s^{-2})	$T_{\rm eff}$ (K)	Mass Function ($M_\odot$)	$M_{2,\rm min}$ ($M_\odot$)	$P_{\rm orb}$ (hrs)	Ref.
J1840+6423	0.177	6.34	9120	0.399	0.65	4.5912	(1)(7)
J1112+1117	0.169	6.17	9240	0.028	0.14	4.1395	(2)(7)
J1518+0658	0.197	6.68	9650	0.322	0.58	14.624	(2)(7)
J1614+1912	0.172	6.32	8700	...	...	...	(3)(7)
J2228+3623	0.175	5.78	7890	...	...	...	(3)(7)
J1618+3854	0.179	6.54	8965	...	...	...	(4)
J1738+0333	0.172	6.30	8910	0.000346	1.47	8.51496	(5)(6)

(1)Hermes et al. (2012); (2)Hermes et al. (2013b); (3)Hermes et al. (2013a); (4)Bell et al. (2015); (5)Gianninas et al. (2015); (6)Kilic et al. (2015); (7)Tremblay et al. (2015).

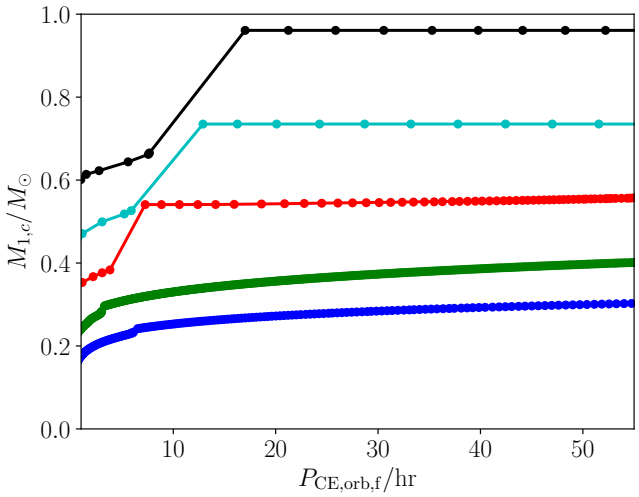

Fig. 2.1.— ELM WD companion mass $M_{1,\rm c}$, as a function of post-common envelope (but pre-magnetic braking) orbital period, $P_{\rm CE,orb,f}$. The lines represent different progenitor mass $M_1/M_\odot = 1, 2, 3, 4, 5$ for the companion. The ELM WD progenitor is assumed to have mass $M_2 = 1.3\,M_\odot$.

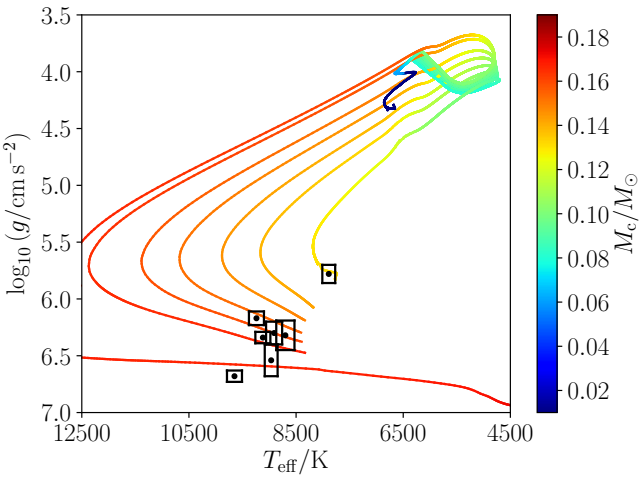

Fig. 2.2.— Evolutionary models for the donor of initial mass $M_{\rm d,i} = 1.3\,M_\odot$ and (constant) accretor mass $M_{\rm a,i} = 0.6\,M_\odot$. The figure shows the entire range of ELM WDs, which is covered by the range of initial orbital periods $P_{\rm orb,i}$ =0.90, 0.93, 0.95, 0.97, 0.99, 1.02 days, from right to left. In addition, a model with slightly larger $P_{\rm orb,i} = 1.03$ day is shown, for which shell flashes occur on the WD cooling track. The color indicates the helium core mass, $M_{\rm c}\,(M_\odot)$. The black points with error bars are the seven pulsating ELM WDs. The track with $P_{\rm orb,i} = 0.90$ day gives the minimum mass of the ELM WD to be $M_{\rm d,f} = 0.146 M_\odot$. The $P_{\rm orb,i} = 1.03$ day model yields a WD of mass $M_{\rm d,f} = 0.179\,M_\odot$. The evolution between the first and last shell flashes is not shown on the plot, for clarity.

range of ELM WDs is covered by the initial orbital period $P_{\rm orb,i}$ =0.90, 0.91, 0.93, 0.95, 0.97, 0.99, 1.02 days, after the CE but before the RLOF phase. The narrow range of $P_{\rm orb,i}$ which produce ELM WD is similar to the result found by Smedley et al. (2017). The donor in the track with $P_{\rm orb,i} = 1.03\,{\rm day}$ has a core mass large enough that diffusion-aided shell flashes occur on the WD cooling track. The color indicates $M_{\rm c}$. The black points with error boxes represent the seven pulsating ELM WDs with parameters derived using 3-D atmosphere models (Tremblay et al. 2015) except J1618+3854 (since only the $\log_{10}\,g$ and $T_{\rm eff}$ from 1-D atmosphere model is given in other references), with the half width of the box showing the measurement uncertainty.

All runs begin at the ZAMS with $\log_{10}\,(g/{\rm cm\,s^{-2}}) = 4.4$ and $T_{\rm eff} = 6500\,{\rm K}$. Along the MS, and as the star evolves to the RGB, its radius increases with $M_{\rm c}$, and so wider orbits come into contact with larger $M_{\rm c}$. The ELM WD commences MT with $0.06 \lesssim M_{\rm c}/M_\odot \lesssim 0.1$, and $M_{\rm c}$ increases during the MT phase. Figure 2.2 shows that models with larger $M_{\rm c}$ evolve to a higher maximum $T_{\rm eff}$, the elbow in the curve that separates the pre-WD phase (increasing $T_{\rm eff}$) from the WD cooling track (decreasing $T_{\rm eff}$). This plot shows the same behavior between shell flashes, that the loops in the $\log g - T_{\rm eff}$ plane become larger, evolving to higher maximum $T_{\rm eff}$. As a result, when systems with shell flashes enter the WD cooling track, their evolution is more nearly horizontal, at constant $\log_{10}\,g$. This gives rise to a wedge in the $\log_{10}\,g - T_{\rm eff}$ plane which separates the ELM WD with $M \lesssim 0.18\,M_\odot$ without shell flashes from the slightly more massive WDs, with $M \gtrsim 0.18\,M_\odot$, which do have shell flashes. The hydrogen-rich envelope is thinner after the shell flashes, so the residual hydrogen burning is smaller and the system evolves to lower $T_{\rm eff}$ more quickly. All runs were evolved to an age 13.7 Gyr, except the one run in the Figure which come back into

contact. Furthermore, the low-mass donor star evolves slower and cannot reach the WD cooling phase by the age of the Galactic disk (10 Gyr). We extended the evolution to 13.7 Gyr to see if the WD cooling phase can be reached within a Hubble time. The ELM WDs in Figure 2.2 have much longer cooling times, and only get down to $T_{\rm eff} \simeq 8000\,{\rm K}$, while the run with shell flashes in the lower panel makes it down to $T_{\rm eff} \lesssim 4000\,{\rm K}$. The observed systems evidently span the range of ELM WDs with thick envelopes as well as those which have undergone shell flashes.

For smaller $P_{\rm orb,i}$, the donor comes into contact at core mass $0.01 \lesssim M_{\rm c}/M_\odot \lesssim 0.07$, and stays in contact to short $P_{\rm orb} \lesssim 1$hr. For systems that come into contact early on the MS, at very small $M_{\rm c} \lesssim 0.01\,M_\odot$, standard CV evolution with a period gap at 2-3 hours is recovered. However, the radiative core is small or nonexistent in this case, and they are not expected to be g-mode pulsators. The core mass at contact for these cases is small, at roughly $M_{\rm c} \lesssim 0.06\,M_\odot$, in agreement with Podsiadlowski et al. (2003).

Figure 2.3 shows $\dot{M}_{\rm d}$ versus $P_{\rm orb}$ (top panel), $\dot{J}$ contributions versus $P_{\rm orb}$ (second panel), donor $R_{\rm d}$ versus $M_{\rm d}$ (third panel) and $P_{\rm orb}$ versus age (bottom panel). The initial periods are $P_{\rm orb,i} = 0.90$ (blue), 0.95 (green), 0.99 (red) and 1.02 days (cyan).

In the top two panels, evolutionary tracks producing ELM WDs start at long periods and proceed to shorter periods on the whole. Magnetic braking is small for $M_{\rm d,i} = 1.3\,M_\odot$ on the MS, due to the small surface convection zone, so $P_{\rm orb}$ is nearly constant during that time. When the system first comes into contact, TTMT results in high mass-loss rates $10^{-8} \lesssim \dot{M}_{\rm d}/M_\odot\,{\rm yr}^{-1} \lesssim 10^{-7}$. TTMT continues until the ratio $M_{\rm d}/M_{\rm a}$ decreases to the critical value (1 for conservative transfer, see Woods et al. 2012) at which point TTMT ends, and the much slower nuclear or $\dot{J}$ timescale MT takes over. During TTMT, $\dot{J}_{\rm ml}$ dominates, due to the high accretion rates (second

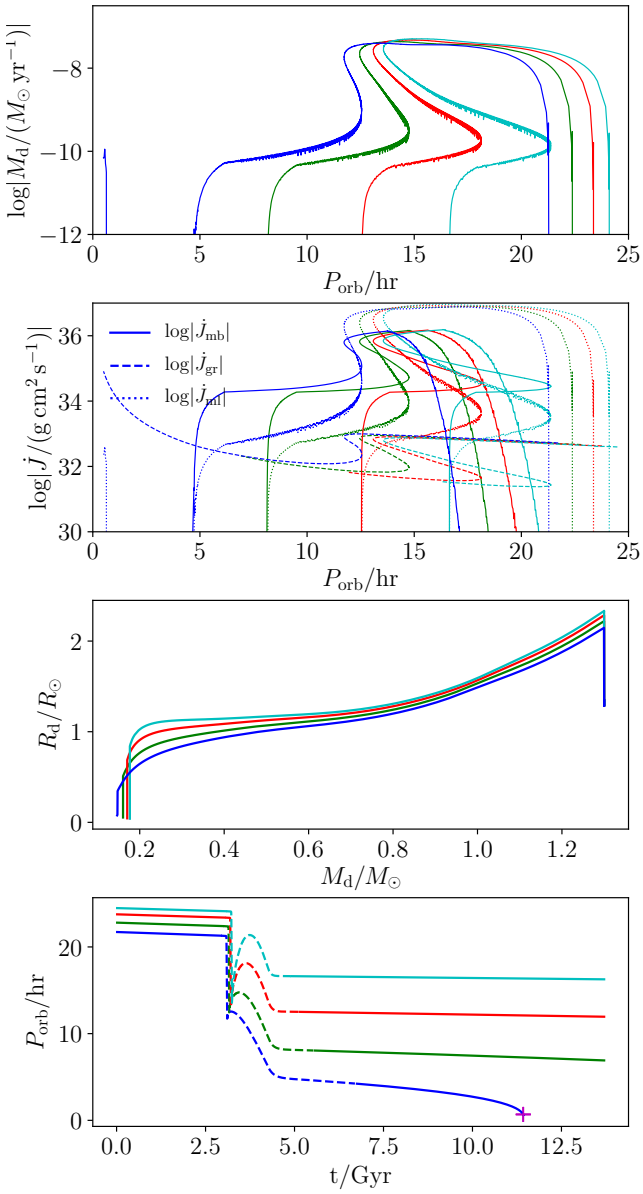

Fig. 2.3.— Several evolutionary tracks with $P_{\rm orb,i} = 0.90$ (blue), 0.95 (green), 0.99 (red) and 1.02 (cyan) day for $M_{\rm d,i} = 1.3\,M_\odot$ and $M_{\rm a,i} = 0.6\,M_\odot$ (see Figure 2.2). From top to bottom, the panels give the mass-loss rate of the donor star ($\dot{M}_{\rm d}$) versus orbital period ($P_{\rm orb}$), the separate contributions to the orbital angular momentum loss rate ($\dot{J}_{\rm ml}$, $\dot{J}_{\rm mb}$ and $\dot{J}_{\rm gr}$) versus $P_{\rm orb}$, the donor star radius ($R_{\rm d}$) versus donor mass ($M_{\rm d}$), and $P_{\rm orb}$ versus age (t). In the bottom panel, on the $P_{\rm orb,i} = 0.90$ day track, the magenta cross marks the beginning of the second phase of MT.

panel). Shortly thereafter, the increased size of the convection zone removes the suppression of $\dot{J}_{\rm mb}$, and it subsequently dominates until MT turns off at $5 \leqslant P_{\rm orb}/{\rm hr} \leqslant 11$. Subsequently $J_{\rm gr}$ dominates and all systems undergo orbital decay. Only the lowest mass, less evolved donors undergo sufficient orbital decay to come back into contact at $P_{\rm orb} \approx 1\,{\rm hr}$. For larger $M_{\rm c}$, evolution driven by the expansion of the star as it tries to ascend the RGB becomes more important than orbital shrinkage due to magnetic braking, leading to a period bifurcation separating the orbits which shrink from those which expand (Podsiadlowski et al. 2003).

The third panel in Figure 2.3 shows donor radius as a function of mass during the evolution. Before contact, $R_{\rm d}$ increases with $M_{\rm c}$. Smaller $P_{\rm orb,i}$ runs commence MT first, at smaller $R_{\rm d}$, while larger $P_{\rm orb,i}$ allows $R_{\rm d}$ to grow further. During TTMT, the high MT rate causes the radius to be slightly inflated. As discussed in Appendix 2.6 (see Figure 2.22), the decrease in mass of the hydrogen-rich envelope leads to smaller hydrogen shell-burning luminosity, accompanied by shrinkage of the radius. This is seen in the steep drop in radius in third panel of Figure 2.3, leading the system to fall out of contact, as shown in the first panel. Models with thick hydrogen envelopes have modest shrinkage in radius beyond that point. The lowest mass model comes back into contact, evolving toward smaller $M_{\rm d}$.

The bottom panel in Figure 2.3 shows $P_{\rm orb}$ versus age. The evolution starts on the left, with tracks at different $P_{\rm orb,i}$ denoted by solid lines. When MT commences (dashed lines starting at 3 Gyr), rapid orbital decay occurs during TTMT. Then the slower orbit evolution on the $\dot{J}$ timescale lasts 2 to 3 Gyr. During this slow phase of MT, slight orbit expansion occurs for large $M_{\rm c}$, while continued orbital decay occurs for small $M_{\rm c}$. When MT ceases, the donor becomes an ELM WD near 5 to 6 Gyr (solid lines). The three largest $P_{\rm orb,i}$ and $M_{\rm c}$ tracks show only modest orbital decay

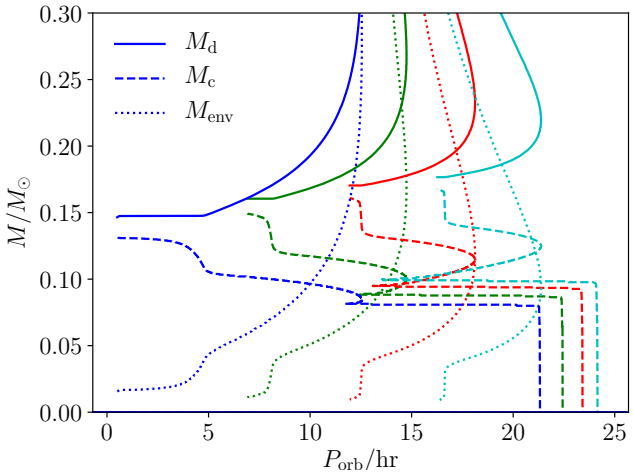

Fig. 2.4.— Donor star mass (M_d, solid), helium core mass (M_c, dashed) and envelope mass ($M_\mathrm{env} = M_\mathrm{d} - M_\mathrm{c}$, dotted) as a function of P_orb, for $P_\mathrm{orb,i} = 0.90$ (blue), 0.95 (green), 0.99 (red) and 1.02 (cyan) days, $M_\mathrm{d,i} = 1.3\,M_\odot$ and $M_\mathrm{a,i} = 0.6\,M_\odot$.

due to $\dot{J}_\mathrm{gr}$, while the lowest line decays from $P_\mathrm{orb} = 5\,\mathrm{hr}$ to 1 hr, at which point MT re-commences (the magenta cross).

Figure 2.4 shows total donor mass M_d, helium core mass M_c and envelope mass $M_\mathrm{env} = M_\mathrm{d} - M_\mathrm{c}$ versus P_orb. The tracks start from the right of the plot near $20 \lesssim P_\mathrm{orb}/\mathrm{hr} \lesssim 25$. The total donor mass M_d decreases downward during MT, and becomes constant when MT ceases. The envelope mass is seen to smoothly decrease, until the end of MT at $5 \leqslant P_\mathrm{orb}/\mathrm{hr} \leqslant 20$. The envelope mass M_env continues to decrease due to residual hydrogen burning, while the orbit slowly decays due to $\dot{J}_\mathrm{gr}$. The M_c lines initially rise vertically, as M_c increases before MT. The TTMT phase is so short that there is no time for M_c to grow above $0.07 \lesssim M_\mathrm{c}/M_\odot \lesssim 0.10$. The nuclear timescale MT is much longer, and M_c increases to $0.13 \lesssim M_\mathrm{c}/M_\odot \lesssim 0.15$. After MT, an additional $0.02 \lesssim M_\mathrm{c}/M_\odot \lesssim 0.03$ is converted from envelope to core by nuclear burning, during which time the orbit decays due to $\dot{J}_\mathrm{gr}$.

From the discussion in Section 2.2 (see Equation 2.3), the thickness of the con-

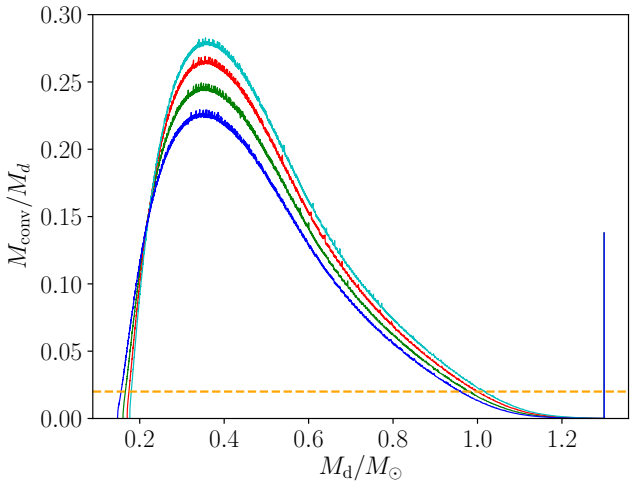

Fig. 2.5.— Mass fraction of the convective zone ($M_{\rm conv}/M_{\rm d}$) versus $M_{\rm d}$ for $M_{\rm d,i} = 1.3M_\odot$, $M_{\rm a,i} = 0.6M_\odot$ and $P_{\rm orb,i} = 0.9$ (blue), 0.95 (green), 0.99 (red), 1.02(cyan) days. The horizontal orange dashed line marks the value of $M_{\rm conv}/M_{\rm d}$ above which the full magnetic braking is applied, and below which magnetic braking is suppressed (see Equation 2.3).

vective envelope is an important parameter for the effectiveness of magnetic braking. Figure 2.5 shows the mass of the convective envelope $M_{\rm conv}$ as a function of $M_{\rm d}$. The systems evolve from right to left during MT. The $M_{\rm d,i} = 1.3\,M_\odot$ donor has a small convective envelope on the MS. The spike at $M_{\rm d} = 1.3\,M_\odot$, is due to the convective core on the MS. As $M_{\rm c}$ grows and the shell burning luminosity increases, $M_{\rm conv}$ increases. When nearly all the hydrogen-rich envelope has been lost, the luminosity drops and the convection zone shrinks again. The orange dashed line gives the threshold below which magnetic braking is exponentially suppressed. For the ELM WD, $M_{\rm conv}$ drops below the threshold and magnetic braking shuts off.

Figure 2.6 shows the same $\log g$ versus $T_{\rm eff}$ as Figure 2.2. The circles are placed at 1 Gyr intervals. Systems covered by the tracks have ages 9-12 Gyrs. The solid line shows phases where the system is out of contact, while the dashed lines show phases where MT is occurring. Following Steinfadt et al. (2010), phases for which the lowest

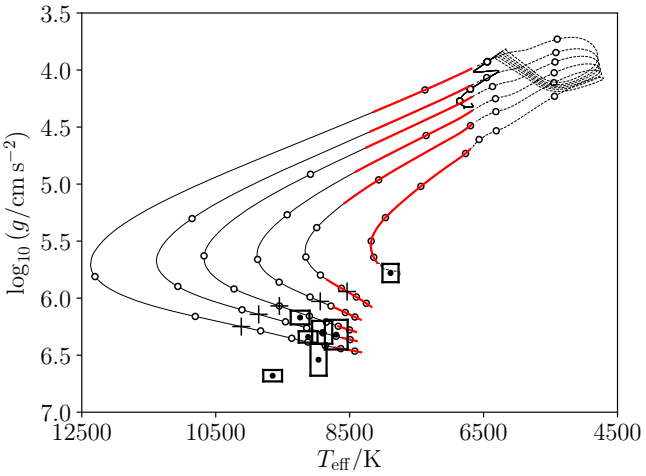

Fig. 2.6.— Gravity ($\log g$) versus $T_{\rm eff}$ for $M_{\rm d,i} = 1.3 M_\odot$, $M_{\rm a,i} = 0.6 M_\odot$ and $P_{\rm orb,i} =$ 0.90, 0.93, 0.95, 0.97, 0.99, 1.02 days. The hollow dots are placed at 1 Gyr intervals. The solid line shows phases where the system is out of contact, while the dashed lines show phases where MT is occurring. The black crosses show the places where the model reaches the diffusive equilibrium, see Section 2.3.5 for details.

order $\ell = 1$ g-mode is unstable are estimated by Brickhill's criterion, $P(\mathrm{g1}) \leqslant 8\pi \mathrm{t_{th}}$, and are covered by red lines, where $P(\mathrm{g1})$ is the mode period of the lowest order g-mode and $t_{\rm th}$ is the thermal time at the base of the surface convection zone. The two data points at high $\log g$ would require $M_{\rm d,f} > 0.18\,M_\odot$ tracks which are not shown on the plot. The estimate of the instability strip used here appears to give too cool a blue edge $T_{\rm eff}$ to explain the systems near $8500 \leqslant T_{\rm eff}/\mathrm{K} \leqslant 9,500$.

Figure 2.7 displays $T_{\rm eff}$ versus $P_{\rm orb}$ for $P_{\rm orb,i} = 0.90$, 0.93, 0.95, 0.97, 0.99, 1.02 days as well as the four observed systems with measured $P_{\rm orb}$. The evolution starts from the right hand side of the plot. The dashed, solid and red lines have the same meaning as in Figure 2.6. The pre-WD phase starts at $T_{\rm eff} \gtrsim 6500$ K. After the turning point as the $T_{\rm eff}$ reaches the maximum, the WD enters its cooling phase. The two pulsators with the shortest $P_{\rm orb}$ have slightly higher $T_{\rm eff}$ than the models. The lines covered by red segments show the unstable g1 mode with Brickhill's criterion. In

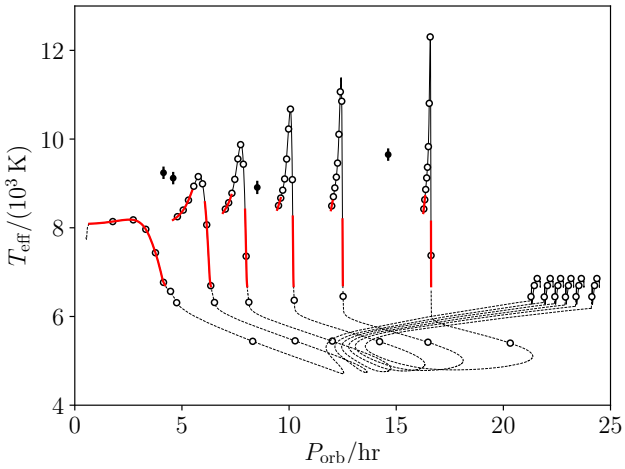

Fig. 2.7.— Effective temperature ($T_{\rm eff}$) versus $P_{\rm orb}$ for $M_{\rm d,i} = 1.3 M_\odot$, $M_{\rm a,i} = 0.6 M_\odot$ and $P_{\rm orb,i} = 0.90$, 0.93, 0.95, 0.97, 0.99, 1.02 days. The solid line shows phases where the system is out of contact, while the dashed lines show phases where MT is occurring. The red lines show models for which the g1 mode is unstable by Brickhill's criterion.

the following discussion section it will be shown that lower-mass donor and high-mass accretor can give better agreement.

2.3.2 A More Massive Accretor

The runs in this section use the same $M_{\rm d,i} = 1.3\,M_\odot$ but a heavier accretor mass $M_{\rm a,i} = 0.9\,M_\odot$. The structures and the evolutionary tracks of the donor stars do not change significantly with companion mass, while the orbital period of the system can be different (Istrate et al. 2016).

Figure 2.8 shows $M_{\rm d}$, $M_{\rm c}$ and $M_{\rm env}$ versus $P_{\rm orb}$, and should be compared to the fiducial case in Figure 2.4. After the onset of RLOF, the orbit first goes outward slightly, and then shrinks until $M_{\rm d} \approx M_{\rm a}$. The accretor is larger, so the orbit does not shrink as much as the fiducial case and the mass-loss rate is also smaller. The donor star is slightly less evolved at the beginning of the RLOF because, for the same

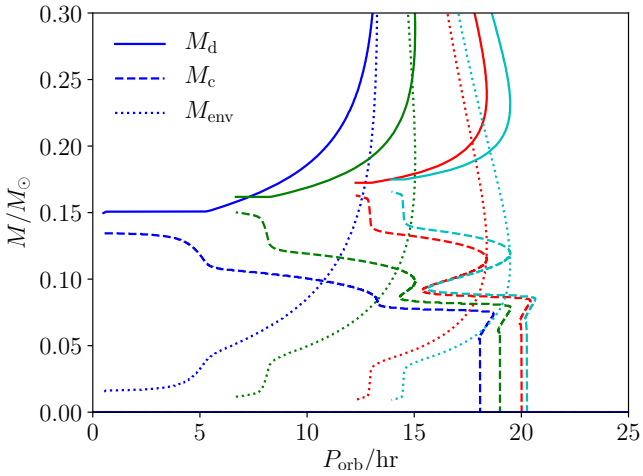

Fig. 2.8.— Same as Figure 2.4, but for donor mass $M_{\rm d,i} = 1.3\,M_\odot$ and heavier accretor mass $M_{\rm a,i} = 0.9\,M_\odot$. The orbital period for each line is $P_{\rm orb,i} = 0.90$ (blue), 0.95 (green), 0.99 (red) and 1.01 (cyan) days.

separation, the larger accretor makes the Roche-lobe radius smaller. As a result, smaller $P_{\rm orb,i}$ must be used to get the same $M_{\rm d,f}$.

The main difference between Figures 2.9 and 2.7 occurs on the WD cooling track after maximum $T_{\rm eff}$. During this long period, the larger $M_{\rm a,i}$ increases $\dot{J}_{\rm gr}$, causing the orbit to shrink faster. This is more evident for small $P_{\rm orb}$. A specific example is given in Figure 2.21, in which the pre-WD evolution is similar but the heavier accretor causes more orbital decay on the WD cooling track.

2.3.3 Solar Mass Donor and Low Mass Accretor

This section contains a comparison of evolutionary models for $M_{\rm d,i} = 1.0\,M_\odot$ and $M_{\rm a,i} = 0.45\,M_\odot$ to the fiducial case results in Section 2.3.1. The companion mass is near the upper end of the mass range for helium core WDs. In addition, $M_{\rm a,i}$ is also low enough that long $P_{\rm orb,i}$ models exhibit unstable MT. Even lower $M_{\rm a,i}$ can lead to unstable MT at a broader range of $P_{\rm orb,i}$.

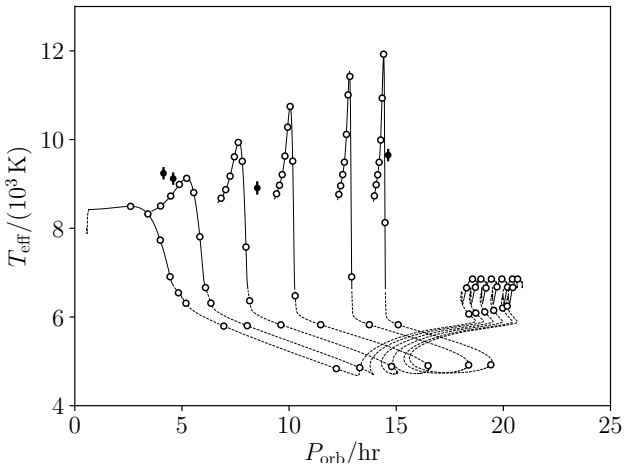

Fig. 2.9.— Same with Figure 2.7, but for donor mass $M_{\rm d,i} = 1.3\,M_\odot$ and larger accretor mass $M_{\rm a,i} = 0.9\,M_\odot$. he orbital period for each line is $P_{\rm orb,i} = 0.78$, 0.8, 0.82, 0.84, 0.86, 0.87 day.

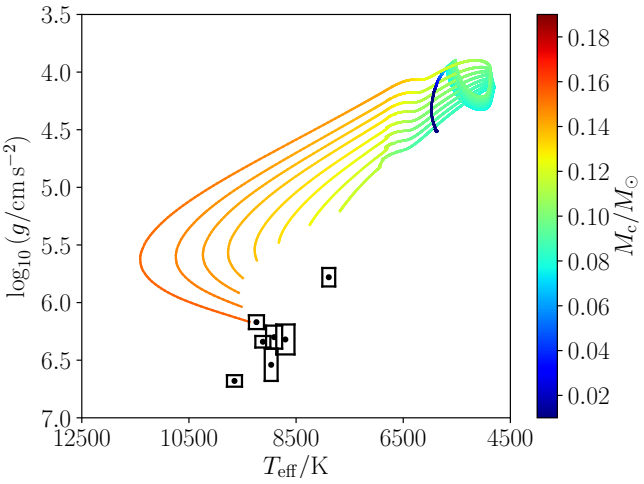

Fig. 2.10.— Evolutionary models for $M_{\rm d,i} = 1.0\,M_\odot$ and $M_{\rm a,i} = 0.45\,M_\odot$. The figure shows the entire range of ELM WDs, which is covered by the range of initial orbital periods $P_{\rm orb,i}$ =2.3, 2.35, 2.4, 2.45, 2.5, 2.55, 2.6, 2.67 days, from right to left. See Figure 2.2 for the description of the black dots.

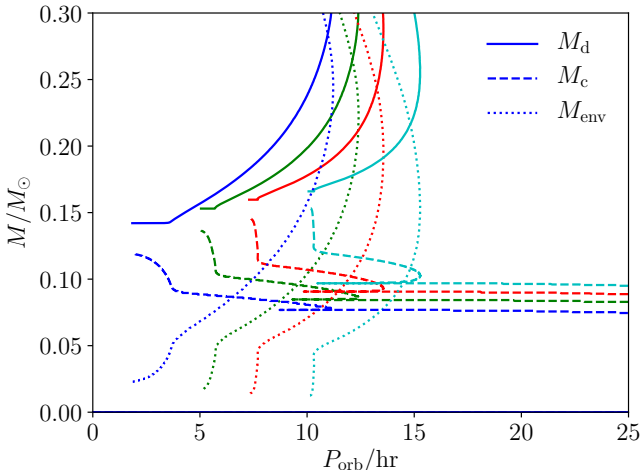

Fig. 2.11.— Same as Figure 2.4, but for $M_{\rm d,i} = 1.0\,M_\odot$ and a helium core accretor $M_{\rm a,i} = 0.45\,M_\odot$, for $P_{\rm orb,i} = 2.3$ (blue), 2.45 (green), 2.55 (red) and 2.67 (cyan) days.

Figure 2.10 gives the evolutionary tracks for $M_{\rm d,i} = 1.0\,M_\odot$ and $M_{\rm a,i} = 0.45\,M_\odot$ with $P_{\rm orb,i}$ =2.3, 2.35, 2.4, 2.45, 2.5, 2.55, 2.6, 2.67 days. The axes are the same as in Figure 2.2. For $P_{\rm orb,i} < 2.3$ days, accretion never ceases and the orbit shrinks to $P_{\rm orb} < 1$ hour. For $P_{\rm orb,i} > 2.67$ days, MT commences with a sufficiently large convective envelope that unstable MT occurs, yielding an upper limit to the WD mass produced with these evolutionary sequences. This is to be contrasted with the fiducial case in Figure 2.2, where the ELM WD sequence joins on to the sequences of WDs at larger $P_{\rm orb,i}$ which have shell flashes. Hence the bottom track in Figure 2.2, which shows the WD cooling track after flashes have stopped, would not occur for this case, due to the smaller $M_{\rm a,i}$ used in this section.

Figure 2.10 shows that most tracks have insufficient time to reach the $T_{\rm eff}$ of the data points. This is due to the long MS evolution. The $\log g$ at the elbow is slightly smaller than for the fiducial case.

Similar to Figure 2.4, Figure 2.11 shows $M_{\rm d}$, $M_{\rm c}$ and $M_{\rm env}$ as a function of $P_{\rm orb,i}$, now with $M_{\rm d,i} = 1.0\,M_\odot$ and $M_{\rm a,i} = 0.45\,M_\odot$. The selected $P_{\rm orb,i}$ are 2.3, 2.45, 2.55,

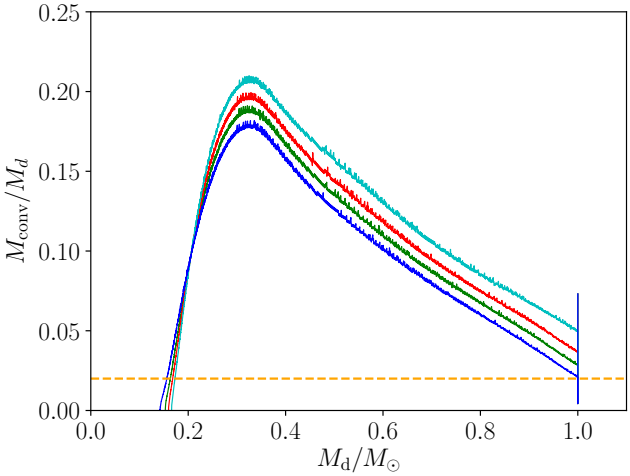

Fig. 2.12.— Mass fraction of the convective zone versus donor mass $M_{\rm d}$ for $M_{\rm d,i} = 1.0 M_\odot$, $M_{\rm a,i} = 0.45 M_\odot$ and $P_{\rm orb,i} = 2.3$ (blue), 2.45 (green), 2.55 (red), 2.67(cyan) days. See Figure 2.5 to compare to the fiducial model.

2.67 days. Tracks enter from the right hand side of the plot due to the large magnetic braking. This is in contrast to the fiducial case where RLOF began due to an increase in the stellar radius near the end of the MS. The tracks at smaller $P_{\rm orb}$ have incomplete burning of the envelope within the Hubble time.

Figure 2.12 shows $M_{\rm conv}/M_{\rm d}$ versus $M_{\rm d}$ for $M_{\rm d,i} = 1.0\,M_\odot$. The outer convection zone grows during the MS. As $P_{\rm orb,i}$ increases, the onset of RLOF occurs later, and with a larger surface convection zone. Since the outer convection zone has $q_{\rm conv} > 0.02$, magnetic braking is much larger than for the fiducial case and is evident in Figure 2.11. Therefore, making an ELM WD needs longer $P_{\rm orb,i}$ for $M_{\rm d,i} = 1.0\,M_\odot$, $P_{\rm orb,i} > 25$ hours. For even longer $P_{\rm orb,i}$, $M_{\rm conv}$ is sufficiently large for unstable MT to occur.

Figure 2.13 shows $T_{\rm eff}$ versus $P_{\rm orb}$, and should be compared to the fiducial model in Figure 2.7. First note that there are no tracks which end at $P_{\rm orb} > 10$ hours due to unstable MT. In the fiducial case, the heavier WDs with shell flashes would end in that region. Given sufficient time, the tracks at $P_{\rm orb} < 5$ hours would have slightly

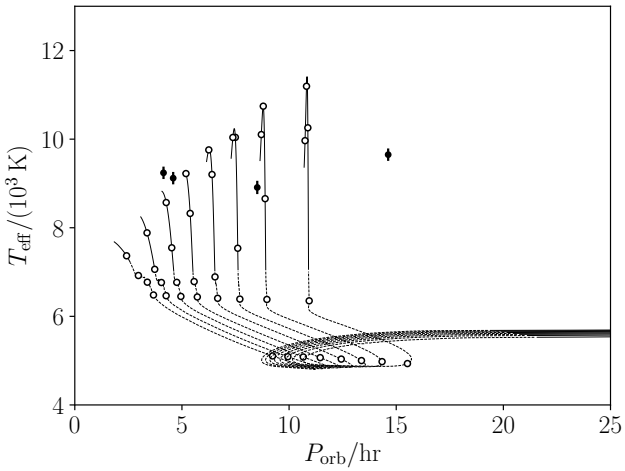

Fig. 2.13.— The evolutionary tracks of $M_{\rm d,i} = 1.0\,M_\odot$, $M_{\rm a,i} = 0.45\,M_\odot$ and $P_{\rm orb,i}$= 2.3, 2.35, 2.4, 2.45, 2.5, 2.55, 2.6, 2.67 days from right to left in the $T_{\rm eff}$ vs. $P_{\rm orb}$ plane. The hollow dots are placed at 1 Gyr intervals. The solid line gives the out of contact of the system, the dashed lines gives the in contact of the system.

larger maximum $T_{\rm eff}$, and would explain the data points better. However, there is insufficient time to reach the elbow.

2.3.4 The Maximum ELM WD Progenitor Mass

Given that more massive donors have a shorter MS phase, this leaves more time for the resultant ELM WDs to cool to $T_{\rm eff} \simeq 9,000$K and become pulsators. However, sufficiently massive progenitors produce helium cores at terminal age MS which are larger than the maximum ELM WD to avoid shell flashes. Hence there is a maximum progenitor which can create an ELM WD. This section describes models with donor mass $M_{\rm d} = 1.5\,M_\odot$ which approaches this limit.

Figure 2.14 shows evolutionary tracks for $M_{\rm d,i} = 1.5\,M_\odot$ and $M_{\rm a,i} = 0.6\,M_\odot$, for the range of initial orbital periods $P_{\rm orb,i} = 0.85$, 0.86, 0.87, 0.88, 0.89, 0.9 day. Comparing to the fiducial case in Figure 2.2, the $M_{\rm d,i} = 1.5\,M_\odot$ case does not produce lower mass

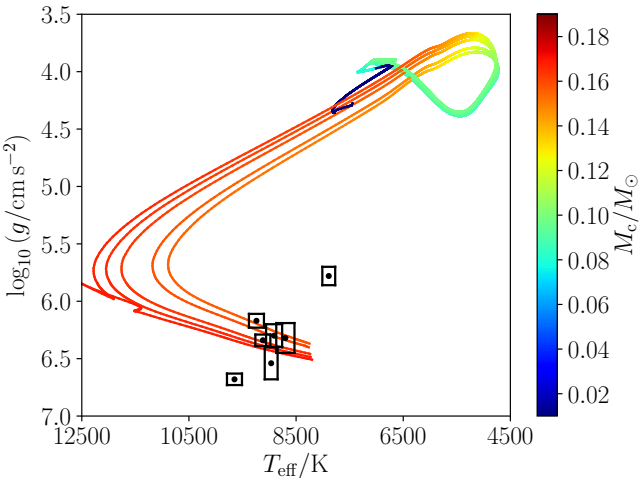

Fig. 2.14.— Evolutionary models for $M_{\rm d,i} = 1.5\,M_\odot$ and $M_{\rm a,i} = 0.60\,M_\odot$. The figure shows the entire range of ELM WDs (all of which have masses greater than 0.16 $M_\odot$), covering the range of initial orbital periods $P_{\rm orb,i}$ =0.85, 0.86, 0.87, 0.88, 0.89, 0.9 day, from right to left. See Figure 2.2 for the description the black dots. The leftmost track ($P_{\rm orb,i}$ =0.9 day) experiences a weak hydrogen flash prior to the WD cooling phase.

$M_{\rm d,f}$ which cover the small $\log g$ and $T_{\rm eff}$ part of the plot. In the $M_{\rm d,i} = 1.3\,M_\odot$ case, $0.07 \lesssim M_{\rm c}/M_\odot \lesssim 0.1$ before the onset of RLOF for cases which make an ELM WD with $M_{\rm d,f} \lesssim 0.17\,M_\odot$. By contrast, the runs with $M_{\rm d,i} = 1.5 M_\odot$ failed to produce an ELM WD (for which MT ceased) with mass less than 0.168 $M_\odot$. The leftmost track in Figure 2.14 has $P_{\rm orb,i} = 0.85$ days, and initial periods shorter than this value will have continuous MT and never emerge as an ELM pulsator.

Figure 2.15 shows $T_{\rm eff}$ versus $P_{\rm orb}$. The tracks start at the ZAMS with $20 \lesssim P_{\rm orb,i}/{\rm hr} \lesssim 21$, and the MT starts roughly 1-2 Gyr into the MS evolution of the donor star. The final WD thus has more time to cool, more time passes between the start of MT and the end of the 13.7 Gyr simulation, than in the lower-mass donor case. After MT commences and enough mass has been lost that $M_{\rm d} \lesssim M_{\rm a}$, the orbit expands dramatically and can exceed the initial separation $a_{\rm i}$. The smallest $P_{\rm orb,f}$ is near 12

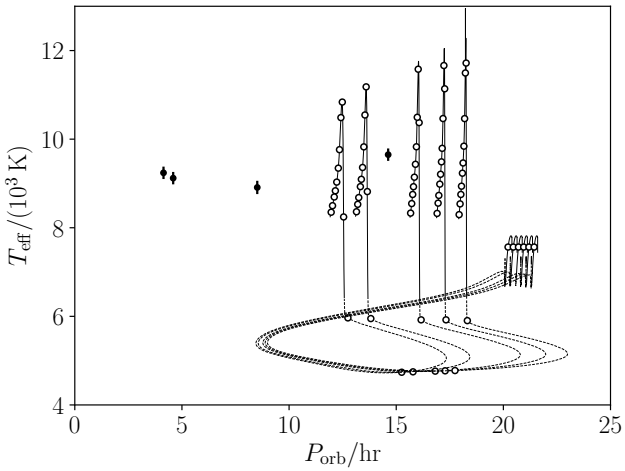

Fig. 2.15.— Same as Figure 2.7 for $M_{\rm d,i} = 1.5\,M_\odot$, $M_{\rm a,i} = 0.6\,M_\odot$ and $P_{\rm orb,i}$= 0.85, 0.86, 0.87, 0.88, 0.89, 0.9 day from right to left.

hours. As such, the $M_{\rm d,i} = 1.5 M_\odot$ case is unable to account for the three systems with $P_{\rm orb} < 12$ hrs.

Further increase of the donor mass above $M_{\rm d,i} = 1.5\,M_\odot$ would lead to larger $M_{\rm c}$ at terminal age MS, and larger final WD mass. The upper limit for $M_{\rm d,i}$ which may produce an ELM WD is thus near $1.5 \leqslant M_{\rm d,i}/M_\odot \leqslant 1.6$.

2.3.5 Mode Periods

Adiabatic mode periods have been computed using the GYRE code (Townsend & Teitler 2013), which is part of the MESA distribution.

Figure 2.16 shows the propagation diagram and the composition versus radius fraction $r/R_{\rm d}$ during the post-MT evolution of the $M_{\rm d,i} = 1.3\,M_\odot$, $M_{\rm a,i} = 0.6\,M_\odot$ and $P_{\rm orb,i} = 0.95\,$day model. Three different times are shown, where the color of the lines indicates the age, with the blue, green, and red lines representing models at 5.63 Gyr (right after the MT), 7.85 Gyr (at the elbow), and 13.7 Gyr (the termination of the simulation), respectively. The bump in the square of the Brunt - Väisälä frequency

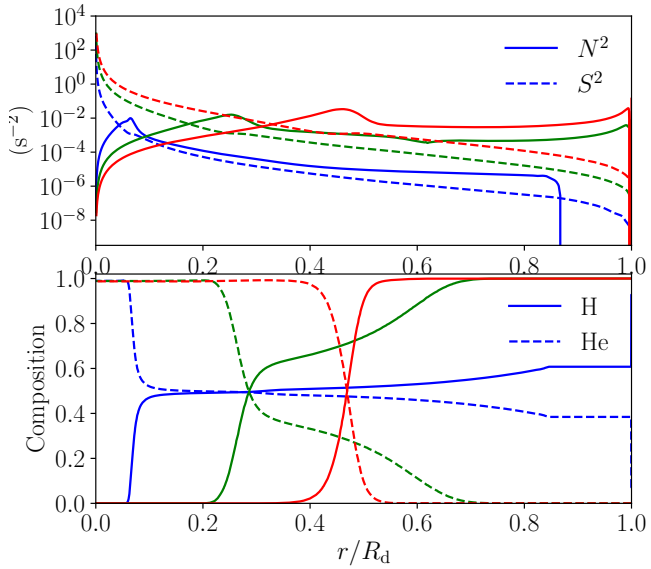

Fig. 2.16.— Propagation diagram (top panel) for the evolutionary track with $M_{\rm d,i} = 1.3\,M_\odot$, $M_{\rm a,i} = 0.6\,M_\odot$ and $P_{\rm orb,i} = 0.95\,$day. The solid lines show the Brunt - Väisälä frequency while the dashed lines give the square of the Lamb frequency for $\ell = 1$. The bump in the buoyancy frequency is due to the composition change from hydrogen to helium with depth. The color of the lines indicate the age, with the blue, green, and red lines representing models at 5.63 Gyr (right after the MT), 7.85 Gyr (at the elbow), and 13.7 Gyr (the termination of the simulation), respectively.

N^2 is caused by the composition switch from hydrogen to helium. After MT ends, the size of the helium core increases due to sinking of helium in the envelope and ongoing burning of hydrogen in the envelope.

In order for the composition profile to be in diffusive equilibrium, the diffusion timescale must be shorter than the nuclear burning and cooling timescales. The composition profile in Figure 2.16 is far from diffusive equilibrium just after MT (blue line) and also at the elbow (green line). The red line is in diffusive equilibrium to a good approximation, and a range of ages (not shown here) were in diffusive equilibrium as well. A close examination of the composition profiles at different ages shows that the residual hydrogen burning ends at nearly the time that diffusive equilibrium is established. The age at which diffusive equilibrium is established was determined for each of the tracks in Figure 2.6, and their position marked by a black cross. The rightmost track with the shortest $P_{\rm orb,i}$ didn't reach diffusive equilibrium before the second MT phase. The six pulsators with $8,500 \lesssim T_{\rm eff}/{\rm K} \lesssim 9,000$ are in diffusive equilibrium to a good approximation.

Fig. 2.17 shows the p-mode frequency spacing and g-mode period spacing for the fiducial model after MT has ceased. The different color lines represent different $P_{\rm orb,i}$. The blue and green lines appear shorter because they were terminated at the start of a second phase of MT. The g-mode period spacing is strongly dependent on the WD mass, so the lines differ by up to 30%. Also, g-mode period spacing depends on the age, mainly through the thickness of the hydrogen envelope, so there can be about 15% differences in the period spacing along an individual evolutionary track. A minimum in the g-mode period spacing occurs near the elbow separating the pre-WD and the WD cooling track. The p-mode frequency spacing becomes nearly constant for the high-mass models, however for the lower mass models the spacing is slowly

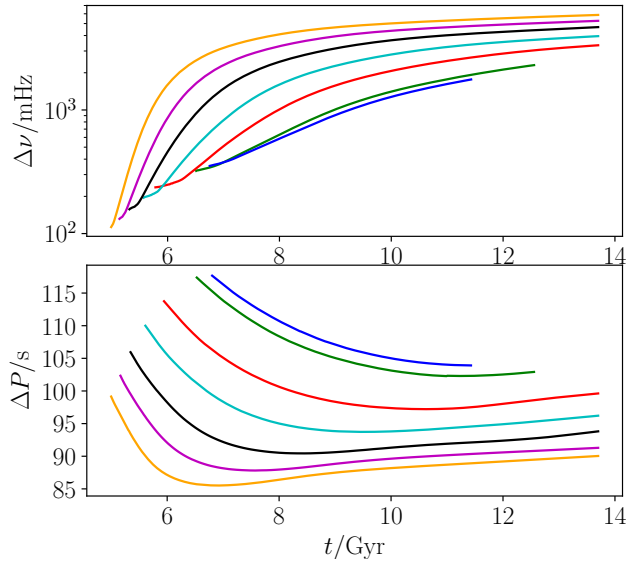

Fig. 2.17.— The p-mode frequency spacing (top panel) and the g-mode period spacing (bottom panel) versus donor star age. The fiducial model with $M_{\rm d,i} = 1.3\,M_\odot$ and $M_{\rm a,i} = 0.6\,M_\odot$ is used, with $P_{\rm orb,i} = 0.90$ (blue), 0.91 (green), 0.93 (red), 0.95 (cyan), 0.97 (black), 0.99 (magenta) and 1.01 (orange) days.

increasing in time over many Gyrs.

Fig. 2.18 displays the lowest order g-mode and p-mode for one evolutionary track ($M_{\rm d,i} = 1.3\,M_\odot$, $M_{\rm a,i} = 0.6\,M_\odot$, $P_{\rm orb,i} = 0.95$ day). Most of the oscillation modes are mixed modes on the pre-WD track, meaning that near the radiative core, the mode behaves like a g-mode, and in the outer convection zone the mode behaves like a p-mode with larger radial displacement. A sequence of avoided crossings are observed during the approximately 2 Gyr pre-WD phase. Starting at 7.5 Gyr, on the WD cooling track, the avoided crossings end, and the g-mode and p-mode are distinct, separated with gap in period. This period separation increases during the subsequent WD cooling phase.

Fig. 2.19 shows the $\ell = 1$ p-modes (dashed) and g-modes (solid) at a fixed $T_{\rm eff} =$ 9000 K. The final WD masses are from six evolutionary tracks, with $P_{\rm orb,i} = 0.93$, 0.95, 0.97, 0.99, 1.01, 1.03 days and $M_{\rm d,i} = 1.3\,M_\odot$, $M_{\rm a,i} = 0.6\,M_\odot$. The period gap

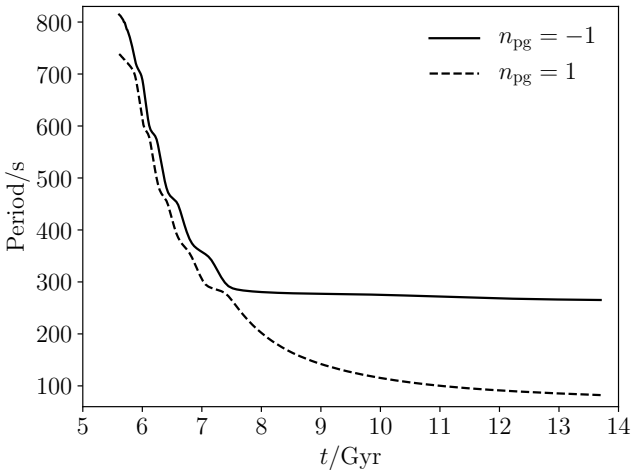

Fig. 2.18.— The lowest order of p-mode (dashed line) and g-mode (solid line) periods versus age after the MT phase for the track with $M_{\rm d,i} = 1.3 M_\odot$, $M_{\rm a,i} = 0.6 M_\odot$, $P_{\rm orb,i} = 0.95$ day.

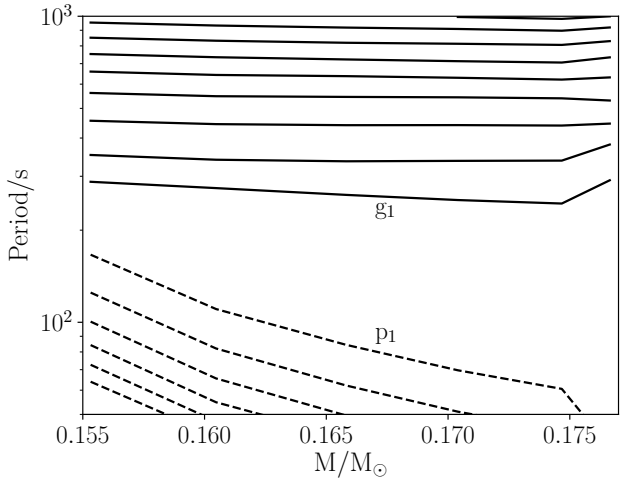

Fig. 2.19.— Eigen-periods versus the WD mass for different models evaluated at $T_{\rm eff} = 9000$ K. The six models with $M_{\rm d,i} = 1.3\,M_\odot$ and $M_{\rm a,i} = 0.6\,M_\odot$, and $P_{\rm orb,i} = 0.93$, 0.95, 0.97, 0.99, 1.01, 1.03 days are used, and the mode periods evaluated for the model with $T_{\rm eff}$ closest to 9000K.

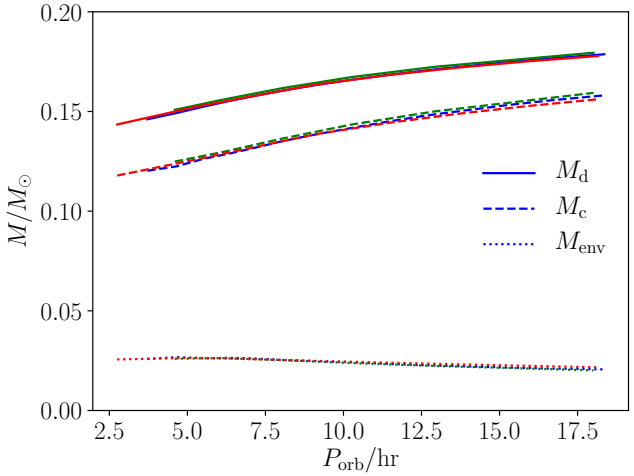

Fig. 2.20.— Total mass ($M_{\rm d}$), helium core mass ($M_{\rm c}$) and envelope mass ($M_{\rm env} = M_{\rm d} - M_{\rm c}$) as a function of $P_{\rm orb}$ at the end of the first phase of MT. The results of $M_{\rm d,i} = 1.3\,M_\odot$, $M_{\rm a,i} = 0.6\,M_\odot$ and $0.9 \leqslant P_{\rm orb,i}/{\rm day} \leqslant 1.03$ with a step of 0.01 day is in blue. The results from $M_{\rm d,i} = 1.3\,M_\odot$, $M_{\rm a,i} = 0.9\,M_\odot$ and $0.78 \leqslant P_{\rm orb,i}/{\rm day} \leqslant 0.89$ is in green. The results of $M_{\rm d,i} = 1.1\,M_\odot$, $M_{\rm a,i} = 0.6\,M_\odot$ and $0.84 \leqslant P_{\rm orb,i}/{\rm day} \leqslant 1.40$ is in red. See Figures 2.2, 2.3, 2.4 and 2.5.

between the p-modes and g-modes increases with the WD mass. The g-mode periods decrease slightly with the increased final mass in the mass range of the ELM WD. For WDs with masses above about $0.18 M_\odot$, the gap between the p-modes and g-modes begins to increase even more rapidly. The mode periods decrease with increasing WD mass, which agrees with CA's result (Córsico & Althaus 2014).

2.4 Discussion

2.4.1 Pre-WD Structure and Orbital Periods just after Mass Transfer Ends

Figure 2.20 shows the stellar mass as a function of $P_{\rm orb}$ just after the MT phase has ended. Three different initial binary mass configurations (fiducial case, larger accretor

mass, and smaller donor mass) are plotted. The helium core mass and hydrogen envelope mass are also plotted for each of these systems. Keep in mind that $P_{\rm orb}$ continues to change in the pre-WD and the WD cooling phases due to gravitational wave losses.Also, there is continued burning of the envelope adding to the core.

For the fiducial case, $P_{\rm orb,i}$ smaller than 0.9 day results in continuous accretion and thus no ELM WD pulsator. The lowest ELM WD mass is $M_{\rm d,f} = 0.146\,M_\odot$, with $M_{\rm c} = 0.120\,M_\odot$ and $P_{\rm orb} = 3.72$ hours. The envelope is 18% of the total mass in this case, much larger than for a standard $0.6\,M_\odot$ carbon/oxygen WD. A large fraction of the radius of the star is also taken up by the envelope in this case. All else being equal, larger $P_{\rm orb,i}$ results in higher pre-WD masses and $M_{\rm c}$, but lower $M_{\rm env}$, immediately post-MT. For $P_{\rm orb,i}$ above 1.03 days (in the fiducial case), the WD experiences hydrogren flashes prior to the cooling phase. At this upper boundary, the pre-WD mass is 0.179 $M_\odot$ and $P_{\rm orb}$ is 18.35 hours immediately post-MT, with an envelope containing only 11.5% of the total mass, which is smaller than all the ELM WDs with no hydrogen flashes before cooling. For non-ELM WDs which experience hydrogen flashes prior to the cooling phase, the resulting envelope is much thinner than for the lower-mass ELM WD. The trend of the thinner envelope with an increasing total WD mass agrees with Istrate et al. (2016).

The results from a simulation with high-mass companion, $M_{\rm a,i} = 0.9\,M_\odot$, are plotted as green lines in Figure 2.20. The blue and green lines are nearly overlapping, producing ELM WDs with almost identical mass, composition, and orbits immediately post-MT. Similarly, the results for a lower-mass donor $M_{\rm d,i} = 1.1 M_\odot$ are shown in red; this setup can create ELM WDs with even lower masses and shorter $P_{\rm orb}$. The minimum ELM WD mass for this setup is 0.143 $M_\odot$, with $P_{\rm orb} = 2.75$ hours immediately post-MT, and the range of $P_{\rm orb,i}$ that results in ELM WDs is considerably larger

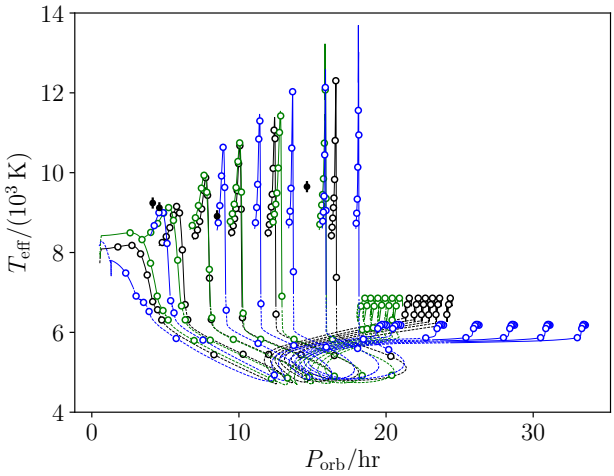

Fig. 2.21.— Evolutionary tracks for trying different donor and accretor mass with $M_{\rm d,i} = 1.1\,M_\odot$, $M_{\rm a,i} = 0.6\,M_\odot$ and $P_{\rm orb,i} = 0.84$, 0.88, 1.0, 1.1, 1.2, 1.3, 1.4 days in blue; $M_{\rm d,i} = 1.3\,M_\odot$, $M_{\rm a,i} = 0.6\,M_\odot$ and $P_{\rm orb,i} = 0.90$, 0.93, 0.95, 0.97, 0.99, 1,02 days in black; and $M_{\rm d,i} = 1.3\,M_\odot$, $M_{\rm a,i} = 0.9\,M_\odot$ and $P_{\rm orb,i} = 0.78$, 0.80, 0.82, 0.84, 0.86, 0.88 day in green. One of the blue tracks ($M_{\rm d,1} = 1.1\,M_\odot$, $M_{\rm a,i} = 0.6\,M_\odot$, $P_{\rm orb,i} = 0.88\,{\rm day}$) passes though the observed $T_{\rm eff}$ and $\log g$ from observation.

than for higher-mass donors. For small donor masses (e.g., $M_{\rm d,i} = 1.0$ and 1.1 $M_\odot$), the thick convective envelope present during the MS phase causes magnetic braking to be much stronger, resulting in a wider accessible range of $P_{\rm orb,i}$. Chen et al. (2017) used a wider range for $M_{\rm d}$, $M_{\rm a}$ and $P_{\rm orb}$ with different metallicities. Their mass-period relation is in agreement with Figure 2.20. And the difference in metallicity doesn't affect this relation at the low-mass WD range.

2.4.2 Models Producing Higher $T_{\rm eff}$ at Shorter $P_{\rm orb}$

From Figure 2.7, two of the ELM WDs, J1840 and J1112, have $4 \lesssim P_{\rm orb}/{\rm hr} \lesssim 5$ (a range that is accessible with our simulations), but with a higher $T_{\rm eff}$ that falls slightly above the theoretical tracks. This section is about making ELM WDs with $T_{\rm eff} \approx$ 9000 K and short orbital periods $P_{\rm orb} \lesssim 5$ hr.

Figure 2.21 compares evolutionary tracks for simulations with different $M_{\rm d,i}$ and $M_{\rm a,i}$. Prior to the WD cooling phase, the donor star reaches a maximum $T_{\rm eff}$. The trend is for this maximum $T_{\rm eff}$ to decrease with decreasing $P_{\rm orb,i}$, and for the fiducial case it appears that having $T_{\rm eff} \approx 9000$ K with $4 \lesssim P_{\rm orb}/{\rm hr} \lesssim 5$ is inaccessible. For a higher accretor mass, and even more dramatically for a lower donor mass, the maximum $T_{\rm eff}$ is increased relative to the fiducial case. So to make a WD with $T_{\rm eff} >$ 9000 K at short orbital periods, the preference is to have a low-mass donor and high mass accretor.

2.4.3 Stellar Engineering Construction of ELM WD

Instead of making ELM WDs models through binary evolution including magnetic braking, a simpler and cheaper alternative would be the following. Evolve a single ZAMS star until it reaches the desired $M_{\rm c}$. Then rapidly (on a timescale much shorter than the thermal and nuclear burning timescales) remove the envelope until the desired $M_{\rm env}$ is left. The resulting model would represent the start of the pre-ELM WD track seen in this work. The two parameters are $M_{\rm c}$ and $M_{\rm env}$, for a fixed composition. The star is then evolved through the pre-ELM WD and WD cooling tracks.

Though much simpler, the problem with this method is that it is not known a priori what to choose for $M_{\rm c}$ and $M_{\rm env}$. Furthermore, this method does not give the expected $P_{\rm orb}$ for the binary, or possible ranges of the mass of the companion WD. The former issue has been addressed in Figure 2.20, which shows how the total stellar mass is partitioned into core and envelope. This greatly restricts the range of allowed $M_{\rm env}$ because even far larger $M_{\rm env}$, up to half the mass of the star can be used for $M < 0.17\,M_{\odot}$ without incurring shell flashes. Such large $M_{\rm env}$ would have many Gyrs

of hydrogen burning until a more physically-motivated envelope size would result.

2.5 Conclusions

This work has discussed the formation of double WD binaries in which one of the stars is an ELM WD with mass $M \lesssim 0.18\,M_{\odot}$. The main results of the paper are as follows.

– ELM WDs cannot be formed via conservative MT. The mass-loss rate for conservative MT is not fast enough to remove more than 90% of the WD progenitor star before the helium core has grown beyond the ELM WD regime. As a result, the minimum mass of an ELM WD made by conservative MT is about 0.2 $M_{\odot}$.

–ELM WDs are not likely to be formed through common envelope evolution. For donor and accretor masses consistent with producing an ELM WD, the binding energy of the donor's envelope (90% of the donor mass) is so large that the final binary orbital separation would be unphysically small (i.e., smaller than the stellar radii), implying merging of the two stars.

– The ELM WD binary formation pathway investigated in this paper posits that the ELM WD progenitor is the initially less massive star. In this picture, the first MT phase occurs when the more massive companion evolves off the MS and the binary enters a common envelope phase. Upon ejection of the common envelope material, the initially more massive star becomes a helium or a carbon-oxygen WD. Once the initially less massive star evolves off the MS, a second (RLOF) MT phase takes place. The donor star in this phase is the progenitor of the ELM WD. Magnetic braking during this phase is crucial to strip the envelope before the core grows too large. Subsequent gravitational wave angular momentum losses lead to decay of the shortest orbital period systems, which may have a second phase of MT. MT was

assumed to be completely non-conservative.

– The possible mass range for the ELM WD progenitor is $1.0 \leqslant M_{\rm d,i}/M_{\odot} \leqslant 1.5$. For initial stellar mass below 1.0 $M_{\odot}$, the WD cannot reach the WD cooling phase within a Hubble time with the initial Z=0.01. For initial masses greater than 1.5 $M_{\odot}$, the (convective) helium core grows too large to make ELM WDs with mass less than about 0.17 $M_{\odot}$.

– Similar final ELM WDs can be produced via different combinations of donor mass, accretor mass and initial orbital period. In the first case the increasing donor radius as it evolves off the MS triggers the RLOF, while in the second case the decreasing orbital radius (caused by magnetic braking) shrinks the Roche lobe radius to the point where it reaches the stellar radius of the donor. An ELM WD binary with short $P_{\rm orb}$ and high $T_{\rm eff}$ may be produced from a low-mass donor with high-mass accretor. In general, the accretor mass should be large enough to avoid unstable MT.

– The mass range of ELM WDs created via RLOF is $0.146 \lesssim M/M_{\odot} \lesssim 0.18$, with $2 \leqslant P_{\rm orb}/{\rm hr} \leqslant 20$. For higher mass WDs there can be several hydrogen flashes prior to the cooling phase, and the final $P_{\rm orb}$ is wider than for ELM WDs with no shell flashes.

Appendix 2.6 and 2.7 discuss WD formation by conservative MT and CE evolution. It is shown that neither of these channels are likely to form an ELM WD.

2.6 Appendix A Conservative Evolution

The simplest case to consider for binary interaction is conservative MT with constant total mass and orbital angular momentum. Evolution occurs on the nuclear timescale

of the donor star, and significant orbit expansion occurs as it ascends the RGB.

Han et al. (2000) extended earlier studies (e.g. Kippenhahn et al. 1967) by considering $Z = 0.02$ stars with a range of ZAMS donor mass $1 \leqslant M_{\rm d,i}/M_{\odot} \leqslant 8$ and mass ratios $1.1 \leqslant (q = M_{\rm d,i}/M_{\rm a,i}) \leqslant 4$. Here $M_{\rm d,i}$ and $M_{\rm a,i}$ are the initial donor and accretor masses. The initial orbital separation and period, $a_{\rm i}$ and $P_{\rm orb,i}$, were set so that RLOF commenced in the early, middle or late Hertzsprung gap. This study found that the smallest WD masses are produced through a combination of the smallest possible donor masses, which evolve in the age of the Galaxy, the smallest accretor masses, to give higher mass-loss rates, and the smallest initial separations, to avoid building up the helium core. For a given donor mass, there is a limit on how small the accretor mass can be in order to avoid unstable MT. The smallest mass WD in their 150 simulations was $M = 0.21\,M_{\odot}$, with parameters $M_{\rm d,i} = 1.0\,M_{\odot}$, $M_{\rm a,i} = 0.5\,M_{\odot}$ and $P_{\rm orb,i} = 0.49\,{\rm day}$. Hence while conservative evolution produces masses approaching the ELM WD mass range, it appears that it cannot robustly produce WDs in the mass range $0.1 \leqslant M/M_{\odot} \leqslant 0.2$. Further, the final orbital periods have $P_{\rm orb,f} \approx 1\,{\rm week}$, much wider than the observed ELM systems.

The numerical results of Han et al. (2000) can be understood with the analytic treatment in Refsdal & Weigert (1971). For conservative evolution, the total mass $M_{\rm d,f} + M_{\rm a,f} = M_{\rm d,i} + M_{\rm a,i}$ is constant between the initial and final states, where $M_{\rm d,f}$ and $M_{\rm a,f}$ are the final donor and accretor star masses. The constancy of orbital angular momentum implies that $a_{\rm i}(M_{\rm d,i}M_{\rm a,i})^2 = a_{\rm f}(M_{\rm d,f}M_{\rm a,f})^2$, where $a_{\rm f}$ is the final separation after the MT. Kepler's 3rd law can be used to write $a_{\rm i} = (G(M_{\rm d,i} + M_{\rm a,i})P_{\rm orb,i}^2/(2\pi)^2)^{1/3}$, where $P_{\rm orb,i}$ is the orbital period where RLOF commences. Lastly, a mass–radius relation is required for the low-mass RGB star, at the maximum radius attained before the envelope becomes too thin and the radius

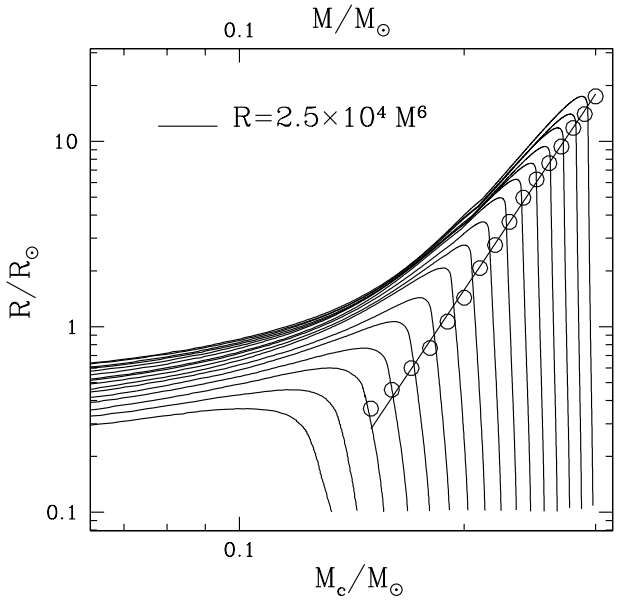

Fig. 2.22.— Solid lines show stellar radius (R, abscissa) versus helium core mass ($M_{\rm c}$, lower axis ordinate) during the evolution of single stars with metallicity $Z = 0.01$. The lines represent stellar masses $M/M_\odot = 0.15, 0.16, ..., 0.30$ from bottom to top. The open circles show the maximum radius along each track versus total mass (M, upper axis ordinate). The solid line is a fit to the circles, given by $R/R_\odot = 2.5 \times 10^4\,(M/M_\odot)^6$.

shrinks. Following Refsdal & Weigert (1971), this is estimated from single star evolution tracks.

MESA was used to evolve stars of constant total mass $M/M_\odot = 0.15, 0.16, ..., 0.30$ from ZAMS to the first shell flash on the WD cooling track, as shown in Figure 2.22. A maximum occurs in radius, beyond which the radius shrinks with further decrease of the envelope. The open circles show maximum radius versus total mass, and the solid line is a fit given by $R(M_{\rm d,f}) = 2.5 \times 10^4\, R_\odot (M_{\rm d,f}/M_\odot)^6$. Combining all these results, and approximating $M_{\rm a,f} = M_{\rm d,i} + M_{\rm a,i} - M_{\rm d,f} \simeq M_{\rm d,i} + M_{\rm a,i}$, gives the final WD mass

$$M_{\rm d,f} = 0.29\, M_\odot \left(\frac{P_{\rm orb,i}}{1\,{\rm day}}\right)^{0.087} \left(\frac{M_{\rm d,i} M_{\rm a,i}}{M_\odot (M_{\rm d,i} + M_{\rm a,i})}\right)^{0.26}. \tag{2.5}$$

Han et al. (2000)'s conclusions about the variation of $M_{\rm d,f}$ with $P_{\rm orb,i}$, $M_{\rm d,i}$ and $M_{\rm a,i}$ are directly observed in this formula. It agrees with the final WD masses of Han et al. (2000) to an accuracy of 2-3%.

To derive the smallest possible WD mass from conservative evolution, the accretor mass is evaluated at the stability limit $M_{\rm a,i} \simeq M_{\rm d,i}/2.5$, the donor mass is set to the smallest that can evolve in the age of the Galaxy, $M_{\rm d,i} \simeq 1.0\, M_\odot$ for $Z = 0.01$, and the initial orbital period is set so that RLOF commences near the end of the MS, $P_{\rm orb,i} \simeq 0.6\,{\rm day}$, with the result

$$M_{\rm d,f,min} \simeq 0.20\, M_\odot. \tag{2.6}$$

Hence conservative evolution cannot lead to an ELM WD of mass $M \lesssim 0.18\, M_\odot$.

It is instructive to consider why conservative MT produces WDs with mass $M > 0.2\, M_\odot$. Consider a donor of mass $M_{\rm d,i} = 1.2\, M_\odot$ near the end of the MS, with a $M_{\rm c} \simeq 0.1\, M_\odot$ core already built. For the core to be limited to $M_{\rm c} \lesssim 0.15\, M_\odot$ means

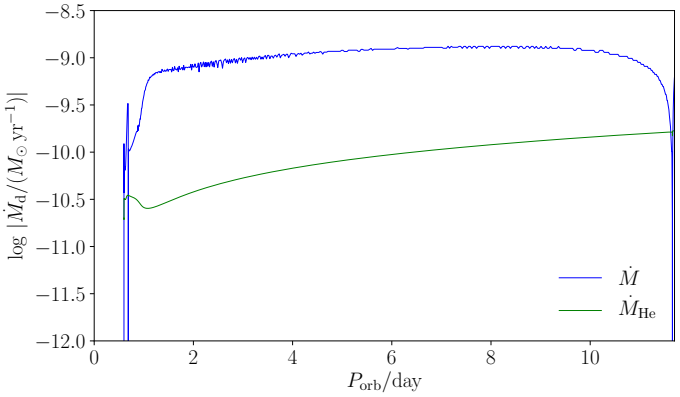

Fig. 2.23.— Mass loss rate, $\dot{M}_{\rm d}$, and growth rate of the helium core, $\dot{M}_{\rm c}$, for conservative evolution of a $M_{\rm d,i} = 1.2\,M_\odot$ donor with a $M_{\rm a,i} = 0.8\,M_\odot$ accretor, and initial orbital period $P_{\rm orb,i} = 0.6\,{\rm day}$. The solid line is the mass-loss rate from the star, and the dashed line is the growth rate of the helium core.

that only $0.05\,M_\odot$ can be added to the core while $1.05\,M_\odot$ must be lost by RLOF, requiring a mass-loss rate for donor of $|\dot{M}_{\rm d}| \gtrsim 20\,\dot{M}_{\rm c}$, where $\dot{M}_{\rm c}$ is the rate at which the helium core grows due to hydrogen shell burning. Figure 2.23 shows a MESA calculation of conservative binary evolution with a $M_{\rm d,i} = 1.2\,M_\odot$ donor transferring mass to a $M_{\rm a,i} = 0.8\,M_\odot$ accretor, with initial orbital period of $P_{\rm orb,i} = 0.6\,{\rm day}$. For $M_{\rm d,i} > M_{\rm a,i}$, there is an initial phase of TTMT at high $\dot{M}_{\rm d}$. Once the donor mass nearly equals the accretor mass $M_{\rm d} \lesssim M_{\rm a}$, this is followed by a second phase at lower $\dot{M}_{\rm d}$ on the nuclear timescale of the donor. It is during the second phase that the helium core builds up to large mass. Figure 2.23 shows that, as shell burning causes the radius to expand, setting $\dot{M}_{\rm d}$, it is also adding to the helium core at a rate $\dot{M}_{\rm c}$. The second phase has $10 \lesssim |\dot{M}_{\rm d}|/\dot{M}_{\rm c} \lesssim 15$, which allows the core to grow too much. What is needed is a faster rate of RLOF, to limit the increase of $M_{\rm c}$.

Lastly, conservative evolution tends to produce orbital periods far larger than that of ELM WDs. Plugging the result in Equation 2.5 in to Kepler's third law, the final

orbital period is

$$P_{\rm orb,f} = 2.2\,{\rm day}\left(\frac{P_{\rm orb,i}}{0.5\,{\rm day}}\right)^{0.74}\left(\frac{M_{\rm d,i}}{1\,M_\odot}\frac{0.5\,M_\odot}{M_{\rm a,i}}\frac{1.5\,M_\odot}{M_{\rm d,i}+M_{\rm a,i}}\right)^{2.22}, \qquad (2.7)$$

far larger than that observed for the ELM WDs.

Noise is apparent in the MT rate in Figure 2.23. To assess the size of the noise for different values of MESA solver parameters, runs were carried out with smaller values of "varcontrol_target" in the MESA namelist. This parameter controls the relative variation in values of the solution from one model to the next. A decrease of varcontrol_target from 10^{-3} to 10^{-4} contained smaller amounts of noise by a factor 10 in $\dot{M}_d$, during the time intervals where the MT rate was noisy (i.e., at the start of MT). And this change gave values of M_c, $M_{\rm env}$, R_d, $T_{\rm eff}$ and $\log_{10}\,g$ to better than 1%.

2.7 Appendix B Common Envelope Evolution

If the progenitor of the ELM WD is too massive compared to the companion, then MT can be unstable and grow to extremely large mass. At such high mass-loss rates, the mass is unable to settle on the accretor, and the donor's ejected envelope forms a common envelope around the uncovered core of the donor and the accretor (Tauris & van den Heuvel 2006). Drag forces from the two stars then inject energy and angular momentum into the envelope. If there is sufficient orbital energy to eject the envelope, then the two stars emerge as a much more compact binary. If there is insufficient energy to eject the envelope, merging results.

The problem with forming an ELM WD by CE is that the envelope is much more massive than the core, and an extreme spiral-in is required to eject the envelope.

Merging may be the outcome in many cases. Consider a numerical example with a donor star of mass $M_{\rm d} = 1.4\,M_\odot$ with He core $M_{\rm c} = 0.15\,M_\odot$. For metallicity $Z = 0.01$, the donor's radius is $R_{\rm d} = 2.6\,R_\odot$ for this core size. For unstable MT, there is an upper limit on the accretor's mass of $M_{\rm a} \lesssim M_{\rm d}/2.5 = 0.56\,M_\odot$ for the chosen donor mass. The factor 2.5 was found using MESA simulations for conservative MT, using a range of donor masses. The energy equation for CE evolution equates the binding energy of the donor's envelope to the change in orbital energy (Webbink 1984):

$$\frac{GM_{\rm d}(M_{\rm d} - M_{\rm c})}{\lambda R_{\rm d}} = \alpha \left(\frac{GM_{\rm c}M_{\rm a}}{2a_{\rm f}} - \frac{GM_{\rm d}M_{\rm a}}{2a_{\rm i}} \right), \tag{2.8}$$

where $a_{\rm f}$ is the separation of the resultant binary after CE. At contact, $R_{\rm d} = r_{\rm L}(M_{\rm d}/M_{\rm a})a_{\rm i}$, where $r_{\rm L}(2.5) \simeq 0.46$ relates the stellar radius to the initial separation for a star in Roche-lobe contact (Eggleton 1983). Solving for the final separation and plugging in numbers gives

$$a_{\rm f} = R_{\rm d} \left(\frac{M_{\rm c}M_{\rm a}}{r_{\rm L}M_{\rm d}M_{\rm a} + (2/\alpha\lambda)M_{\rm d}(M_{\rm d} - M_{\rm c})} \right) \simeq R_{\rm d} \left(\frac{\alpha\lambda}{2} \right) \left(\frac{M_{\rm a}}{M_{\rm d}} \right) \left(\frac{M_{\rm c}}{M_{\rm d} - M_{\rm c}} \right) \simeq 0.06\,R_\odot. \tag{2.9}$$

The small separation is due to two requirements. First $M_{\rm d}/M_{\rm a} \gtrsim 2.5$ in order to have unstable MT, and secondly the core is much less massive than the envelope so that $M_{\rm c}/(M_{\rm d} - M_{\rm c}) \approx 0.1$.

If the progenitor of the ELM WD was the initially more massive star, then the companion is a MS star of radius $R_{\rm a} \approx 0.5\,R_\odot$, which cannot fit inside the orbit, implying merging. If the progenitor of the ELM was the initially less massive star, and the initially more massive star became a massive WD, after the ELM WD formed, the

radius of the massive WD is smaller than the ELM WD. The radius of a $M_{\rm c} = 0.15\,M_{\odot}$ ELM WD with a thick hydrogen envelope can be as large as $0.05 \leqslant R_{\rm ELM}/R_{\odot} \leqslant 0.15$, and so the ELM could not fit inside the final separation, and a merger would result. Back to the numerical example at the begining of this section, for the mass ratio $M_{\rm c}/M_{\rm a} = 0.15/0.56 = 0.27$ and an ELM WD radius of $R_{\rm ELM} = 0.08\,R_{\odot}$, the orbit would have to be wider than $a_{\rm f} = R_{\rm ELM}/r_{\rm L}(0.27) > 0.29\,R_{\odot}$ for the ELM WD not to be in contact. For the ELM phase to be long-lived against orbital decay by gravitational radiation, the orbital period should be significantly wider. Similarly, the binary population syntheses work by Bogomazov & Tutukov (2009) indicates there is less probablity that the low-mass helium WD is formed after the CE phase. Chen et al. (2017) show that EL CVn, which is close to the systems in this paper, cannot be produced by CE for the same reason. The orbital separation shrinks too much that the two stars may merge.

Chapter 3

Tidal Dissipation in WASP-12

This chapter is based on Weinberg et al. (2017).

3.1 Introduction

The orbits of hot Jupiters are expected to decay due to tidal dissipation within their host stars (Rasio et al. 1996). While there is considerable indirect evidence of orbital decay in the ensemble properties of hot Jupiter systems (Jackson et al. 2008, 2009; Hansen 2010; Penev et al. 2012; Schlaufman & Winn 2013; Teitler & Königl 2014), the recent transit timing observations of WASP-12 by Maciejewski et al. (2016) and Patra et al. (2017) could be the first direct evidence of orbital decay of an individual system. They detect a decrease in the orbital period at a rate $\dot{P} = -29 \pm 3\,\mathrm{ms\,yr^{-1}}$. This corresponds to an inspiral timescale of just $P/|\dot{P}| = 3.2\,\mathrm{Myr}$ and a stellar tidal quality factor $Q'_* \approx 2 \times 10^5$.

As both studies note, it is difficult to tell whether the observed $\dot{P}$ is due to orbital decay or is instead a portion of a long-term ($\approx 14\mathrm{yr}$) oscillation of the apparent period. The latter could be due to apsidal precession if the eccentricity is $e \approx 0.002$. However,

it is not clear how to maintain such an e in the face of rapid tidal circularization. Patra et al. (2017) mention gravitational perturbations from the star's convective eddies, a mechanism Phinney (1992) proposed to explain the small but nonzero eccentricities of pulsars orbiting white dwarfs. However, the host star ($M_* \simeq 1.3 M_\odot$) has a very low mass convective envelope ($\simeq 10^{-3} M_\odot$) and we estimate that there is too little energy in the eddies to maintain an $e \sim 10^{-3}$. Another mechanism that can cause decade-long oscillations of the period that Patra et al. mention is the Applegate (1992) effect, which invokes variations in the quadrupole moment of the star over a magnetic activity cycle. However, Watson & Marsh (2010) estimate that for WASP-12b, this effect shifts the transit arrival times by $\Delta T \lesssim 10$s after $T \approx 10$yr. This corresponds to an average $|\dot{P}| \simeq 2P\Delta T/T^2 < 1 \mathrm{ms\,yr^{-1}}$ (Birkby et al. 2014), more than an order of magnitude smaller than the measured value.

With a few more years of monitoring it should be possible to distinguish unequivocally between orbital decay and precession (Patra et al. 2017). In this paper, we consider whether the decay explanation is plausible. In Section 3.2, we construct stellar models that fit the observed properties of WASP-12. In Section 3.3, we describe the relevant tidal processes and then use the stellar models to calculate the expected rate of tidal dissipation. We conclude in Section 3.4.

3.2 Stellar Models of WASP-12

The WASP-12 host star has an effective temperature $T_{\rm eff} = 6300 \pm 150$K and a mean density $\rho_* \equiv 3M_*/4\pi R_*^3 = 0.475 \pm 0.038\,\mathrm{g\,cm^{-3}}$ (Hebb et al. 2009; Chan et al. 2011; here and below we adopt the values from the latter reference). Note that ρ_* is measured solely from the transit parameters of the light curve (see Seager & Mallén-Ornelas 2003) and is not derived from a fit to stellar evolution models, unlike

the stellar mass M_* and radius R_*. The spectrum of WASP-12 is consistent with a supersolar metallicity ([Fe/H] $= 0.30 \pm 0.10$) and a spin that is slow ($v \sin i < 2.2 \pm 1.5\,\mathrm{km\,s^{-1}}$) and likely misaligned with the planet's orbital plane (Schlaufman 2010; Albrecht et al. 2012). By fitting stellar models to $T_{\rm eff}$, ρ_*, and the metallicity, Chan et al. (2011; see also Hebb et al. 2009; Enoch et al. 2010; Fossati et al. 2010; Maciejewski et al. 2011) find $M_* = 1.36 \pm 0.14 M_\odot$, $R_* = 1.595 \pm 0.071 R_\odot$, and a surface gravity $\log g_* = 4.164 \pm 0.029$ (in cgs units). Based on three separate age dating techniques (lithium abundance, isochrone analysis, and gyrochronology) Hebb et al. (2009) find that WASP-12 is likely to be several Gyr old, implying an age comparable to its main sequence lifetime.

We construct stellar models using the MESA stellar evolution code (Paxton et al. 2011, 2013, 2015), version 9575. We assume a solar abundance scale based on Asplund et al. (2009; solar metallicity $Z = Z_\odot = 0.0142$) and follow the MESA prescriptions given in Choi et al. (2016) for calculating the abundances, equation of state, opacity, and reaction rates.

As we show below, the properties of WASP-12 are consistent with both $M_* \simeq 1.3 M_\odot$ main-sequence models and $M_* \simeq 1.2 M_\odot$ subgiant models. The range of subgiant models that fit the observations is sensitive to how convection and mixing in radiative zones is implemented in MESA. In particular, we find it is sensitive to the values of the parameters of mixing length theory $\alpha_{\rm MLT}$, overshooting $f_{\rm ov}$, semiconvection $\alpha_{\rm sc}$, and diffusive mixing. Although recent studies are starting to place interesting constraints on some of these parameters (Silva Aguirre et al. 2011; Magic et al. 2015; Moravveji et al. 2015, 2016; Moore & Garaud 2016; Deheuvels et al. 2016), there is still considerable uncertainty, especially as to how they depend on stellar mass, metallicity, and age. For simplicity, we therefore use the Schwarzschild criterion with

$f_{\rm ov} = 0$, we neglect diffusive mixing, and we consider a range of values for $\alpha_{\rm MLT}$.

In Figure 3.1 we show the evolution of $T_{\rm eff}$ and ρ_* for six stellar models. The three $M_* = 1.30-1.35 M_\odot$ models (red dashed curves) match the observed constraints (grey box) when the star is on the main sequence. The three $M_* = 1.20 M_\odot$ models (blue solid curves) match the observed constraints during the post-main sequence phase, when the star is a subgiant and the core is no longer convective. The different models are selected in order to illustrate that the evolution of $T_{\rm eff}$ and ρ_* is sensitive to not only M_*, but also Z and α_{MLT}.

All six models shown in Figure 3.1 spend about 0.5 Gyr within the measured range of $T_{\rm eff}$ and ρ_*. During this portion of their evolution, the radii and surface gravity of the higher-mass models in Fig. 3.1 span $R_* = 1.50 - 1.62 R_\odot$ and $\log g_* = 4.14 - 4.20$ while the lower-mass models span $R_* = 1.47-1.55 R_\odot$ and $\log g_* = 4.13-4.18$. These are consistent with the (model-dependent) constraints reported in the literature.

As we describe in Section 3.3, the efficiency of tidal dissipation is significantly enhanced if WASP-12 has a radiative core. The only models with radiative cores that we find are consistent with the measured $T_{\rm eff}$ and ρ_* are the subgiant models. Torres et al. (2012) estimate a somewhat lower $T_{\rm eff} = 6118 \pm 64$ K, which could match the $T_{\rm eff}$ of main sequence models with fully radiative cores (i.e., $M_* \lesssim 1.1 M_\odot$). However, we find that such models have too high a ρ_*.

In Figure 3.2 we show $T_{\rm eff}$ as a function of ρ_* at the moment the core ceases to be convective and the star enters the subgiant phase. We find that for a given M_*, increasing $\alpha_{\rm MLT}$ or decreasing Z increases $T_{\rm eff}$ and ρ_*. The models that are either inside or to the right (since ρ_* decreases with age) of the grey box are consistent with the observations for a portion of the subgiant branch. The constraints are consistent with subgiant models whose parameters lie in the range $1.20 \lesssim M_*/M_\odot \lesssim 1.25$,

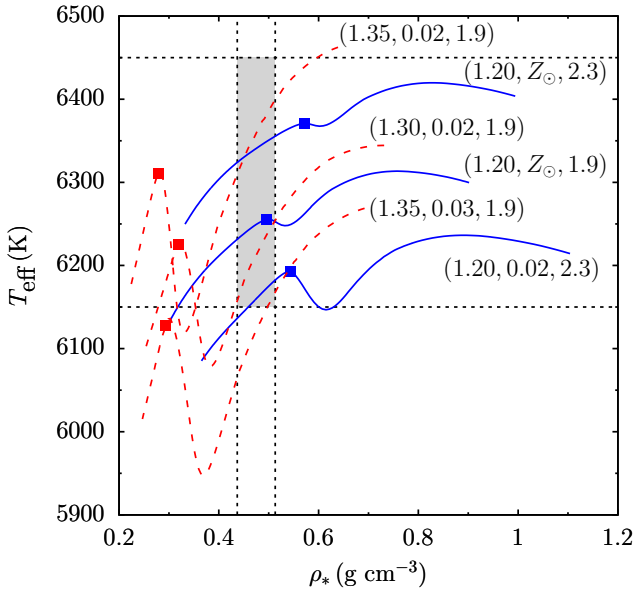

Fig. 3.1.— Evolution of the effective temperature $T_{\rm eff}$ and mean density ρ_* for six stellar models. Each model is labelled by $(M_*/M_\odot, Z, \alpha_{\rm MLT})$. The evolution goes from right to left starting from when the star is $1Gyr$ old. The squares mark when the core ceases to be convective. Observations of WASP-12 constrain its $T_{\rm eff}$ and ρ_* to lie within the region indicated by the grey box. The blue solid (red dashed) curves are models that match the observations when on the sub-giant branch (main sequence).

$Z_\odot \lesssim Z \lesssim 0.03$ (i.e., $0 \lesssim$ [Fe/H] $\lesssim 0.3$), and $1.9 \lesssim \alpha_{\rm MLT} \lesssim 2.3$.

3.3 Tidal dissipation

The orbit of WASP-12 appears circular ($e < 0.05$; Husnoo et al. 2012) and, given the age of the system, the planet's rotation is expected to be synchronized (Goldreich & Soter 1966; Rasio et al. 1996). Therefore, any ongoing tidal dissipation must be occurring within the non-sychronized host star. Dissipation mechanisms include turbulent damping of the equilibrium tide within the convective regions of the star and linear or nonlinear damping of the dynamical tide. Studies of the former find $Q'_* \sim 10^8 - 10^9$ (Penev & Sasselov 2011). This is more than three orders of magnitude too small a dissipation rate (too large a Q'_*) to explain the apparent orbital decay of WASP-12. We therefore focus on tidal dissipation due to the dynamical tide.

The dynamical tide in WASP-12 is dominated by resonantly excited internal gravity waves. Such waves propagate in the stratified regions of the star (where the Brunt-Väisälä buoyancy frequency $N^2 > 0$) and are evanescent within convective regions ($N^2 < 0$). As a result, the dynamical tide is excited near radiative-convective boundaries (RCBs), where its radial wavelength is long and it can couple well to the long lengthscale tidal potential (Zahn 1975, 1977).

When a star like WASP-12 (a late-F star) is on the main sequence, it has both a convective core and a convective envelope. When core hydrogen burning ends and the star evolves off the main-sequence and becomes a subgiant, its core ceases to be convective. In Figure 3.3 we show N as a function of stellar radius r for a main-sequence and subgiant model of WASP-12. In the main-sequence model, the convective core extends from the center to $r \simeq 0.1 R_\odot$ and the convective envelope extends from $r \simeq 1.35 R_\odot$ to very near the surface. The propagation cavity of the

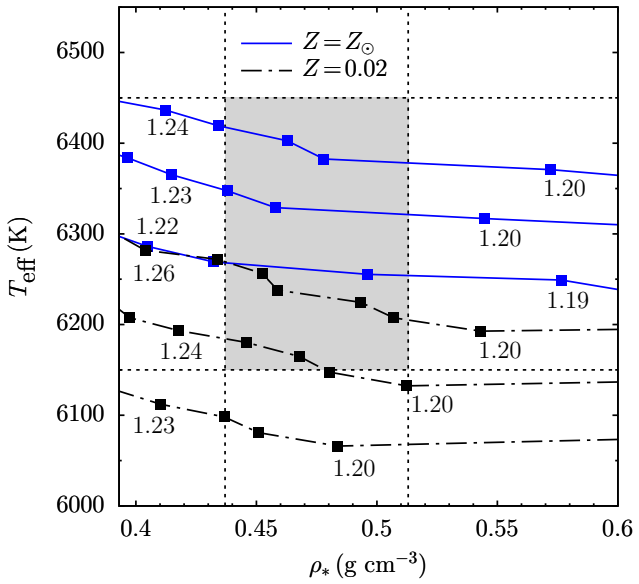

Fig. 3.2.— Effective temperature $T_{\rm eff}$ and mean density ρ_* at the moment when the core ceases to be convective and the star enters the subgiant phase. The labels indicate $M_*/M_\odot$ with points spaced by $0.01 M_\odot$ (connected by straight lines for clarity). The blue solid curves assume solar metallicity $Z = Z_\odot = 0.0142$ and the black dashed-dotted curves assume $Z = 0.02$. The three curves for each Z assume, from bottom to top, $\alpha_{\rm MLT} = 1.9$, 2.1, and 2.3. Observations of WASP-12 constrain its $T_{\rm eff}$ and ρ_* to lie within the region indicated by the grey box.

dynamical tide is determined by these two radii (they are its inner and outer turning points, respectively; see red arrows in Fig. 3.3).

In the subgiant model, by contrast, $N^2 > 0$ all the way to the center. We find a linear scaling with radius $N \simeq Cr$, where $C \simeq 0.1(R_\odot\,\mathrm{s})^{-1}$. The dynamical tide propagates where the tidal frequency $\omega < N(r)$; for the dominant $\ell = 2$ tide, $\omega = 2\Omega$, where Ω is the orbital frequency. Thus, the tide raised by WASP-12b ($\omega/2\pi = 21.2\,\mu$Hz) has an inner turning point at $r \simeq \omega/C \simeq 10^{-3}R_\odot$ during the subgiant phase (blue arrows in Fig. 3.3). The dynamical tide propagates much closer to the center of the star when the star is a subgiant compared to when it is on the main sequence.

3.3.1 Dynamical tide luminosity and wave breaking

If the dynamical tide loses very little energy in the group travel time between turning points, it forms a global standing wave. Conversely, if it loses a significant fraction of its energy between turning points, it behaves more like a traveling wave excited near the outer convection zone and traveling inward to the center. We will show that the dynamical tide is a standing wave for the main sequence models of WASP-12 and a traveling wave for the subgiant models. We now calculate the luminosity L assuming a traveling wave.

In the gravity wave propagation zone, the traveling wave luminosity is given by $L(r) = r^2 \int d\Omega\, \rho\psi_{\rm dyn}\dot{\xi}_{r,\rm dyn}$, where $\psi = \delta p/\rho + U$, δp is the Eulerian pressure perturbation, U is the tidal potential, ξ_r is the radial displacement, and the subscript "dyn" denotes the short-wavelength, dynamical tide piece. $L(r)$ is nearly constant with r in the propagation zone (except near sharp features such as density variations on short

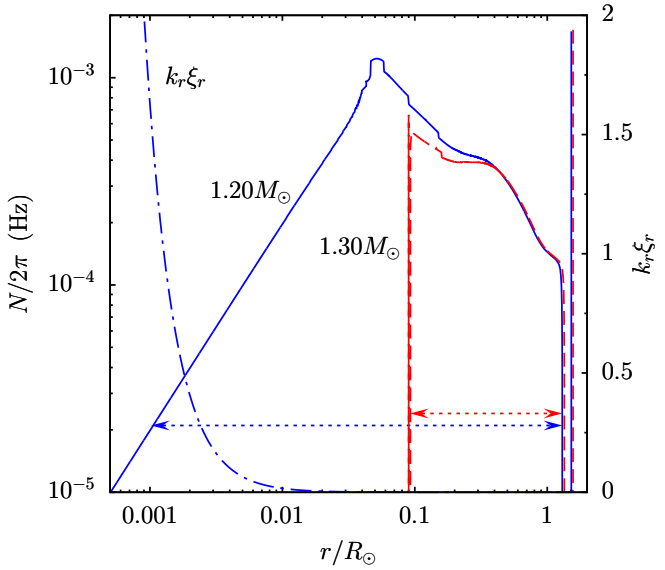

Fig. 3.3.— Radial profile of the Brunt-Väisälä frequency $N/2\pi$ (left-axis) and the nonlinearity measure $k_r\xi_r$ (right-axis). The blue solid curve and red dashed curve show $N/2\pi$ for two WASP-12 models, respectively: the subgiant model $(M_*/M_\odot, Z, \alpha_{\rm MLT}, Age/Gyr)$=$(1.20, Z_\odot, 2.1, 3.7)$ and the main-sequence model $(1.30, 0.02, 1.9, 2.7)$. The blue dashed-dotted curve shows $k_r\xi_r$ for the subgiant model. The arrows indicate the turning points of the dynamical tide.

lengthscales[1]). To compute ξ_r and ψ, we solve the equations of motion of the linear tide (e.g., Weinberg et al. 2012). We use the Cowling approximation, in which the perturbed gravity is ignored, a good approximation for the short-wavelength dynamical tide. A mechanical boundary condition $\psi - U = g\xi_r$ is used at the surface of the star, and the inward-going traveling wave boundary condition $d(\psi - \psi_0)/dr = ik_r(\psi - \psi_0)$ is applied at a radius well within the propagation zone. Here ψ_0 is an approximation of the long-wavelength, particular solution, called the "finite frequency equilibrium tide" (see Arras & Socrates 2010); it is given by $\Lambda^2\psi_0 = \omega^2 d(r^2\xi_{r,\mathrm{eq}})/dr$, where $\Lambda^2 = \ell(\ell+1)$ and $\xi_{r,\mathrm{eq}} = -U/g$ is the radial displacement of the zero-frequency equilibrium tide. The dynamical tide piece of the solution is given by $\xi_{r,\mathrm{dyn}} = \xi_r - \xi_{r,\mathrm{eq}}$ and $\psi_{\mathrm{dyn}} = \psi - \psi_0$.

This numerical calculation of L may be compared to analytic treatments in which approximate solutions in the radiative and convection zones are matched across the RCB (Zahn 1975; Goldreich & Nicholson 1989; Goodman & Dickson 1998; Kushnir et al. 2017). While an analytic treatment is, in principle, useful in providing simple formulae, the solution in the convection zone and the matching conditions at the RCB are complicated and can depend on the tidal frequency and the size of the outer convection zone. Nonetheless, we motivate an approximate fitting formula as follows. Given an equilibrium tide displacement $\xi_{r,\mathrm{eq}} \simeq -U/g$, the dynamical tide near the RCB is $\xi_{r,\mathrm{dyn}} \simeq \zeta(\lambda/r)\xi_{r,\mathrm{eq}}$, where ζ is a dimensionless constant that depends on the structure of the convection zone found by the matching conditions, and $\lambda = [-(\Lambda^2/\omega^2 r^2)dN^2/dr]^{-1/3}$ is the wavelength near the RCB. By the continuity equation, $\Lambda^2\psi_{\mathrm{dyn}}/\omega^2 r^2 \simeq d\xi_{r,\mathrm{dyn}}/dr \simeq \xi_{r,\mathrm{dyn}}/\lambda$. Thus, for the dominant $\ell = 2$ gravity

[1]Our stellar models have one or two sharp spikes in N (near $\sim 0.1R_\odot$) due to composition discontinuities that form as the convective core shrinks. However, these spikes are unphysical; we find that they disappear when we include overshooting and diffusive mixing. Here we simply smooth over them in order to calculate L.

wave,

$$L = A_L \frac{GM_p^2}{r_c} \left(\frac{r_c}{a}\right)^6 \left(\frac{\rho_c}{\bar{\rho}_c}\right) \left(\frac{\omega}{\omega_c}\right)^{8/3} \omega$$
$$\simeq 7 \times 10^{29} A_L \left(\frac{M_p}{10^{-3} M_*}\right)^2 \left(\frac{M_c}{M_\odot}\right)^{-7/3} \left(\frac{r_c}{R_\odot}\right)^{12} \left(\frac{\rho_c}{10^{-3} \mathrm{g\,cm^{-3}}}\right) \left(\frac{P}{\mathrm{day}}\right)^{-23/3} \mathrm{erg\,s^{-1}}, \tag{3.1}$$

Here a is the semi-major axis, r_c is the radius of the RCB where the wave is excited, ρ_c is the density at r_c, $\bar{\rho}_c = 3M_c/4\pi r_c^3$ and M_c are the mean density and enclosed mass within r_c, and $\omega_c = (GM_c/r_c^3)^{1/2}$ is the dynamical frequency at r_c. The dimensionless prefactor $A_L \simeq 0.02\zeta^2[-(r_c/\omega_c^2)dN^2/dr]^{-1/3}$.

Equation (3.1) is similar to the form derived by Kushnir et al. (2017). It is useful if A_L is nearly constant for different P and stellar models. In practice, we find that this is not the case. Specifically, we find that A_L increases with orbital period for $P \lesssim 2\,\mathrm{day}$ (this is because dN^2/dr is not perfectly constant in the driving region; see Barker 2011). Furthermore, at a fixed $P = 1.1\,\mathrm{day}$, we find that the different WASP-12 subgiant models give values in the range $0.2 \lesssim A_L \lesssim 0.6$. Because of the complicated behavior of A_L, we rely on the numerical calculation of L rather than Eq. (3.1).

If a fraction η of the wave luminosity L is deposited in a single group travel time across the star, then (Goldreich & Soter 1966; Ogilvie 2014)

$$\frac{P}{|\dot{P}|} = \frac{G^{2/3} M_p M_* \Omega^{2/3}}{3(M_p + M_*)^{1/3} \eta L} \simeq \frac{9.1}{\eta L_{30}} \left(\frac{M_*}{M_\odot}\right)^{2/3} \left(\frac{M_p}{M_{\mathrm{Jup}}}\right) \left(\frac{P}{\mathrm{day}}\right)^{-2/3} \mathrm{Myr}, \tag{3.2}$$

where $L_{30} = L/10^{30} ergs^{-1}$. The value of η depends on how efficiently the dynamical tide is dissipated as it propagates through the radiative interior.

The principal dissipation mechanisms acting on the dynamical tide are damping

due to radiative diffusion and nonlinear wave interactions (Goodman & Dickson 1998; Barker & Ogilvie 2010; Weinberg et al. 2012; Essick & Weinberg 2016; Chernov et al. 2017). Radiative damping at a rate γ causes the amplitude of the tide to decrease by a factor of $\exp(-\gamma t_{\rm gr})$ in a group travel time $t_{\rm gr}$ across the star. Damping due to nonlinear interactions is especially strong if the wave displacement ξ_r is so large that $k_r \xi_r \gtrsim 1$, where $k_r \simeq \Lambda N/\omega r$ is the radial wavenumber. Such a strongly nonlinear wave overturns the local stratification and breaks. Since it deposits all of its energy and angular momentum before reflecting, wave breaking implies $\eta \simeq 1$ (Barker & Ogilvie 2010; Barker 2011).

We can estimate $k_r \xi_r$ in the WKB approximation using conservation of energy flux, which states that $\rho N^2 v_{\rm gr} |\xi_r|^2 \simeq L/4\pi r^2$ as the dynamical tide propagates inward from the envelope RCB (Goodman & Dickson 1998). Here $v_{\rm gr} \simeq \omega/k_r$ is the radial group velocity and ξ_r now denotes the rms radial displacement averaged over time and angle at fixed radius. This gives

$$k_r \xi_r \simeq \sqrt{\frac{\Lambda^3 N L}{4\pi \rho r^5 \omega^4}} \simeq 1.3 \left(\frac{C_{0.1} L_{30}}{\rho_2}\right)^{1/2} \left(\frac{P}{\rm day}\right)^2 \left(\frac{r}{10^{-3} R_\odot}\right)^{-2}. \tag{3.3}$$

The second line represents the scaling in a radiative core, where $N = Cr$ with $C_{0.1} = C/0.1(R_\odot\,{\rm s})^{-1}$ and $\rho_2 = \rho/10^2 {\rm g\,cm^{-3}}$. Our numerical solutions of $k_r \xi_r$ agree well with this WKB estimate.

3.3.2 Resonance locking

As a star evolves, its g-mode frequencies can increase, allowing them to sweep into resonance with the tidal frequency. If the resulting tidal torques are sufficiently large, the dynamical tide can end up in a stable "resonance lock" and drive orbital decay

on the stellar evolution timescale. Resonance locking has been invoked to explain the observed properties of a variety of tidally interacting binaries (Witte & Savonije 2002; Fuller & Lai 2012; Burkart et al. 2013, 2014; Fuller et al. 2016, 2017).

We find that resonance locking cannot explain the apparent orbital decay of WASP-12. This is because the g-mode frequencies in the models evolve too slowly for a mode to remain in resonance lock at the observed $\dot{P}$ (even during the rapid evolutionary stage just before the convective core disappears). In the future, we plan to investigate whether resonance locking is important in other short-period exoplanetary systems.

3.3.3 Tidal dissipation on the main sequence

We find that tidal dissipation on the main sequence is too inefficient to explain the observed $\dot{P}$. First, we find that $\gamma t_{\rm gr} \approx 10^{-6}$ for internal gravity waves resonant with the tidal forcing (we use the GYRE pulsation code [Townsend & Teitler 2013] to solve the non-adiabatic oscillation equations and thus $\gamma t_{\rm gr}$ for the WASP-12 models). Radiative damping is therefore an insignificant source of dissipation. This is consistent with the results of Chernov et al. (2017), who also consider radiative damping of the dynamical tide in main sequence models of WASP-12. Although they show that the observed $\dot{P}$ could be explained if $\gamma t_{\rm gr} \sim 1$, which they refer to as the moderately large damping regime, they do not identify any mechanism that could enable the tide to be in this regime.

Second, we find $k_r \xi_r \ll 1$ throughout the propagation cavity of the main sequence models. By Eq. (3.3), $k_r \xi_r$ is largest near the inner turning point, which for the main-sequence models is located at $r \simeq 0.1 R_\odot$ (the top of the convective core); at this radius $k_r \xi_r \ll 1$. Thus, the dynamical tide does not break while the star is on

the main sequence.

Even if $k_r\xi_r \ll 1$ and the dynamical tide forms a standing wave, it can still potentially lose energy through weakly nonlinear interactions involving three-mode couplings (Essick & Weinberg 2016). To check this, we computed three-mode coupling coefficients κ_{abc} using the methods described in Weinberg et al. (2012). We considered the stability of the dynamical tide to the resonant parametric instability, which involves the tide (mode a) coupling to daughter g-modes (modes b and c) whose eigenfrequencies satisfy $\omega_b + \omega_c \simeq \omega_a$. We find that κ_{abc} is small ($\kappa_{abc} \sim 1$ using the normalization in Weinberg et al. 2012) and the tide is stable to the parametric instability (i.e., the nonlinear growth rate $\Gamma < \gamma$). We therefore conclude that while the star is on the main sequence, $\eta \ll 1$ and $P/|\dot{P}| \gg$ Myr.

3.3.4 Tidal dissipation on the subgiant branch

In the subgiant models, the radiative damping rate γ is again too small to significantly damp the dynamical tide. However, unlike the main sequence models, the subgiant models have a *radiative* core and a convective envelope. As a result, the inner turning point of the dynamical tide is much closer to the center of the star and we find that $k_r\xi_r \gtrsim 1$ near the inner turning point.

Our numerical solutions give luminosities in the range $L_{30} = [3.0, 10.5]$ for the subgiant models. Specifically, for the subgiant model shown in Fig. 3.3, we find $L_{30} = 3.6$. For this model, the key parameters of the convective envelope are $r_c \simeq 1.30 R_\odot$, $M_c \simeq 1.20 M_\odot$, $\rho_c \simeq 2.3 \times 10^{-3}\,\mathrm{g\,cm^{-3}}$ and the key parameters of the core are $\rho_2 \simeq 3.8$, and $C_{0.1} \simeq 1.3$. Plugging these into Eq. (3.1) and taking $M_p = 1.40 M_{\rm Jup}$ (Chan et al. 2011) gives $L_{30} \simeq 16 A_L$, which comparing to our numerical solution implies $A_L \simeq 0.2$. Evaluating Eq. (3.3) at the inner turning point $r = \omega/C = 1.0 \times 10^{-3} R_\odot$, gives

$k_r\xi_r = 1.5$, in good agreement with the full numerical solution. Our other subgiant models yield very similar results, with values in the range $k_r\xi_r = [1.4, 2.5]$.

This implies that during the subgiant phase, the dynamical tide becomes strongly nonlinear near the inner turning point and breaks. As a result, $\eta \simeq 1$ and by Equation (3.2), the range in L imply decay timescales in the range $P/|\dot{P}| = [1.4, 4.5]\,\mathrm{Myr}$ (and $Q'_* = [0.8, 2.2] \times 10^5$). This agrees well with the observed $P/|\dot{P}| = 3.2 \pm 0.3\,\mathrm{Myr}$.

Although we find $k_r\xi_r > 1$, it is only just slightly in excess of unity and one might wonder whether the wave really is efficiently damped ($\eta \simeq 1$). Numerical simulations by Barker (2011) show that as long as $k_r\xi_r > 1$, the wave breaks and efficiently transfers its angular momentum to the background mean flow. Furthermore, Essick & Weinberg (2016) find that if $k_r\xi_r \gtrsim 0.1$, the dissipation due to weakly nonlinear interactions with secondary waves is nearly as efficient as when $k_r\xi_r \gtrsim 1$. This therefore suggests that $\eta \simeq 1$ for the WASP-12 subgiant models.

3.4 Discussion

The main sequence and subgiant models are both $\approx 3\,\mathrm{Gyr}$ old and spend $\approx 0.5\,\mathrm{Gyr}$ within the measured range of $T_{\rm eff}$ and ρ_*. If the observed $\dot{P}$ is indeed due to orbital decay, then an advantage of the subgiant scenario is that it naturally explains why the planet survived for 3 Gyr and is now decaying on a 3 Myr timescale. Although the system only spends $\sim 0.1\%$ of its life in the present state, there are $\simeq 30$ hot Jupiters with $P < 3\,\mathrm{days}$ orbiting stars with $M_* > 1.2M_\odot$. The dynamical tide likely breaks during the subgiant phase in all of these systems and thus they all spend $\sim 0.1\%$ of their $\sim$ Gyr long lives in a state during which the planet decays on $\sim$ Myr timescales.[2]

[2]As an aside, we note that because $P/|\dot{P}|$ increases rapidly with P, this mechanism cannot explain the apparent deficit of giant planets orbiting subgiants with periods between 10 and 100 days discussed in Schlaufman & Winn (2013).

We therefore estimate that out of the 30 systems, the probability of detecting one in a state like WASP-12 is $\sim 3\%$.

Even though wave breaking of the dynamical tide can drive orbital decay on Myr timescales, it cannot spin up and align the entire star. This is because the wave breaks very close to the stellar center ($r < 0.01 R_\odot$) and while the torque L/Ω might spin up the stellar core (Barker & Ogilvie 2010), it is too small to strongly affect the spin at the stellar surface. Therefore, our results do not conflict with the observed slow, misaligned rotation of WASP-12.

A combination of continued transit timing and occultation observations over the next few years should resolve whether the WASP-12 timing anomalies are due to orbital decay or apsidal precession (Patra et al. 2017). Since we find that the decay scenario is only plausible if the star is a subgiant, tighter constraints on the stellar parameters can also help provide resolution. Given stellar modeling uncertainties, better constraints on just $T_{\rm eff}$ and ρ_* might not be sufficient. Asterosesimology offers a promising alternative. Asteroseismic studies have determined whether stars are subgiants by measuring the sizes of convective cores (Deheuvels et al. 2016) and measured the mass and radii of stars hosting planets to few percent accuracy (Huber et al. 2013).

Chapter 4

Orbital Decay in Binaries

This chapter is based on a submitted paper (Sun et al. 2018).

4.1 Introduction

Tidal friction becomes orders of magnitude larger as stars leave the main sequence (MS) and ascend the RGB. Binaries that suffered relatively weak tidal effects on the MS may suffer catastrophic orbital decay during the SGB (Schlaufman & Winn 2013), RGB and asymptotic giant branch, resulting in the binary components coming into contact. Sufficiently massive secondaries, $M_2 \gtrsim 10^{-2}\,M_\odot$, may then initiate a common envelope spiral-in and ejection of the primary's envelope (Paczynski 1976), forming a close binary containing the secondary and a helium-core white dwarf. Smaller secondaries may give rise to mergers with the helium core of the primary, or destruction in the envelope of the primary (Nelemans & Tauris 1998).

The engulfment of companions proceeds from smaller to larger orbital separation. Most previous studies (e.g. Schröder & Connon Smith 2008; Kunitomo et al. 2011; Mustill & Villaver 2012; Villaver et al. 2014) have focused on the end result, namely

the critical separation outside of which systems may survive as the primary transitions into a white dwarf. This paper focuses on earlier stages, when the primary has left the MS but is well below the tip of the RGB, as these are more commonly found in spectroscopic surveys.

This paper was motivated by the close binaries found in the APOGEE survey. Employing three years of APOGEE (Majewski et al. 2017) observations from the twelfth data release of the Sloan Digital Sky Survey (Alam et al. 2015), Troup et al. (2016) compiled a catalog of 376 newly-found close binary systems. These are single-lined binaries with radial velocity fits for the orbit and secondary minimum mass, and a large range of Galactocentric radius, metallicity and evolutionary state of the primary. This sample is unique, as it contains both dwarf and giant primaries, and secondaries ranging from planetary to stellar masses. The present paper focuses on the 180 primaries which are post-MS, as theory predicts these systems have much stronger tidal friction. Interestingly, brown dwarf (BD) secondaries are nearly as common as stellar-mass secondaries in the APOGEE-1 sample. The putative "brown-dwarf desert", a lack of close binaries with solar-type primaries and BD secondaries, is *not* found in this sample, in seeming contradiction to decades of previous surveys of FGK dwarfs (Grether & Lineweaver 2006). The presence of secondaries, from planetary to brown dwarf to stellar mass, allows a test of synchronization and orbital decay over the entire range, from small-secondary Darwin unstable systems, which will come into contact due to orbital decay, as well as large-secondary systems, which will quickly synchronize. The latter then evolve on the RGB evolutionary time of the primary, with the spin frequency nearly equal to the orbital frequency as the star evolves.

Both equilibrium and dynamical tides are considered in this paper. The first tidal

friction mechanism we use is the equilibrium tide, in which shearing of the the tidally forced fluid motion is dissipated as heat by turbulent viscosity in the convective envelope. As gravity waves are evanescent there, and the frequencies are far below acoustic waves, the fluid motion is not wavelike. Rather, fluid nearly follows equipotential surfaces, and large scale shearing motions are present. This fluid motion is sometimes approximated with the analytic "equilibrium tide" solution out of convenience, although that derivation is only formally valid in radiative zones. (Terquem et al. 1998) However, since the surface of the star is nearly an equipotential, this analytic solution performs well, and is convenient. It is used in this paper. The fluid motions in the convective zone are damped by turbulent viscosity, in which resonant turbulent eddies due to thermal convection transport momentum and damp the tidal shear flow. The dissipation rate for this process depends on the uncertain details of the interaction of small-scale turbulence with a mean flow, but the two theories discussed in this paper have scalings $P_{\rm orb}^{-4}$ and $P_{\rm orb}^{-5}$ for the dissipation rate, and hence decrease much more slowly than the dynamical tide's $P_{\rm orb}^{-7.7}$. Hence it is expected that the dynamical tide dominates at small separation and the equilibrium tide at larger separation. One of the aims of this paper is to estimate the critical separation at which dynamical and equilibrium tide dissipation are comparable.

The dissipation of the equilibrium tide by turbulent viscosity in convection zones was first developed by Zahn (1977). In that paper, a turbulent viscosity $\nu_\ell = v_\ell \ell/3$ was proposed, where $\ell \sim H$ and $v_\ell \sim (F/\rho)^{1/3}$ are the size and velocity of the large, energy-bearing eddies. Here H is the pressure scale height, F is the heat flux, and ρ is the mass density. In many situations where this theory is applied, the large eddy turn-over time, $\tau_\ell = \ell/v_\ell$ is much longer than the forcing period, $P_{\rm f}$, and cannot efficiently transport momentum to damp the shear flow. Zahn (1989) proposed that

large, non-resonant eddies move a small fraction $P_{\rm f}/2\tau_\ell$ of an overturn, and so the eddy turnover time should be reduced by this linear-in-period factor. Goldreich & Nicholson (1977)(hereafter GN) argued that resonant eddies on smaller scales damp the shear. There was later support for dissipation by resonant eddies in both analytic calculations (Goodman & Oh 1997) and numerical simulations (Penev & Sasselov 2011; Penev et al. 2011). Assuming Kolmogorov scalings for the turbulent eddies, GN argue for a quadratic reduction factor $(P_{\rm f}/2\pi\tau_\ell)^2$. For $P_{\rm f} \ll \tau_\ell$, this leads to a very large suppression of the viscosity. By contrast, even for resonant eddies, numerical simulations find a scaling closer to linear, perhaps due to the fact that the largest eddies do not follow inertial-range, Kolmogorov scalings. In addition, the transition from linear to quadratic scaling has not been resolved in the simulations. As the RGB stars studied here may have turnover times $\gtrsim 10^2$ days while the orbital periods are of order days to weeks, there may be several orders of magnitude difference in the predictions given by standard (un-reduced), linear and quadratic scalings.

The treatment of the equilibrium tide in the present paper was influenced by Phinney (1992) and Verbunt & Phinney (1995), who studied circularization of binaries containing an RGB star. The latter presented analytic formulae for circularization which take into account the evolution of the RGB star to larger radius and luminosity. They applied this analytic circularization formula to 28 binaries, finding that all systems could be well explained with a non-reduced kinematic viscosity. Here, equivalent formulae are derived for the orbital decay problem and for reduced viscosity.

Binary orbital frequencies are below the frequencies of acoustic waves, and hence only low-frequency gravity waves can be resonantly excited by the tide. During the SGB and RGB phase, the core is radiative and internal gravity waves are excited by the tide at the boundary between the radiative zone and the convective envelope

(Goodman & Dickson 1998; Bolmont & Mathis 2016; Chernov et al. 2013; Ivanov et al. 2013; Gallet et al. 2017; Weinberg et al. 2017; Kushnir et al. 2017). The waves then travel inward toward the center. Two damping mechanisms may prevent the formation of a standing wave. Radiative diffusion is dominant on the SGB and RGB, and can easily damp the dynamical tide from any orbiting companion, independent of its mass. Even if radiative diffusion were not present, companions larger than roughly 1 Jupiter mass will give rise to such large wave amplitudes near the center that the stratification is overturned and the wave breaks, depositing it's energy as heat and torquing the gas in the wave-breaking layer (Barker & Ogilvie 2010; Barker 2011). In this paper it is assumed that efficient angular momentum redistribution takes place to the rest of the star.

Numerous studies (e.g., Schröder & Connon Smith 2008; Kunitomo et al. 2011; Mustill & Villaver 2012; Villaver et al. 2014) have considered the effect of post-main sequence stellar evolution and tidal evolution on planetary orbits, with the goal of predicting the properties of planetary systems around white dwarfs. For massive planets in close orbits, orbital decay can lead to engulfment of the planet. By contrast, smaller mass planets that do not suffer orbital decay must wait for the star's radius to expand out to their orbit. Mustill & Villaver (2012) employed turbulent viscosity in the star's convective envelope as the tidal friction, and experimented with different prescriptions for reduction of the viscosity when the eddy turnover time is longer than the forcing period. However, since the semi-major axes explored were all large ($\gtrsim$ 1 AU) most of the eddies in the convection zone turn over fast compared to the forcing period, and the full turbulent viscosity ends up being used. High mass loss rates during the post-main sequence evolution will cause orbits to expand as the star's mass decreases.

The prescriptions for the equilibrium and dynamical tide dissipation rates are discussed in Sections 4.2 and 4.3, respectively.

4.2 Equilibrium Tide Dissipation Rate

Consider a primary star of mass M_1 and radius R_1 in a circular orbit of separation a with a secondary star of mass M_2. The tide raised by the secondary in the convective envelope of the primary creates a time-dependent fluid shear, which is damped by the turbulent viscosity of convective eddies. This process transfers energy and angular momentum from the orbit to the stellar convection zone. For simplicity, efficient angular momentum redistribution is assumed in the primary so that the rotation rate Ω is uniform over the star.

The orbital torque, N, is related to the energy dissipation rate in the rotating frame, $\dot{E}$, through the pattern speed $n - \Omega$ as $N = \dot{E}/(\Omega - n)$, where $n = \sqrt{G(M_1 + M_2)/a^3}$ is the orbital frequency. This relation is valid even as $\Omega \to n$, i.e. synchronous rotation. The torque $N \to 0$, since $\dot{E} \sim (\Omega - n)^2 \to 0$ as $\Omega \to n$. This torque changes the orbital angular momentum, $L = \mu n a^2$, where $\mu = M_1 M_2/(M_1 + M_2)$ is the reduced mass of the system. The semi-major axis then changes at a rate

$$\dot{a} = -\frac{2\dot{E}}{\mu n(n - \Omega)a}. \tag{4.1}$$

Since $\dot{E} > 0$, the orbit decays for a slowly rotating star ($\Omega < n$) and expands for a rapidly rotating star ($\Omega > n$). Equation 4.1 agrees with the end result of the derivation in Hut (1981), and is also valid even when the moment of inertia of the primary star is changing with time due to stellar evolution.

For massive secondaries, the spin of the primary may be tidally synchronized to

the orbit, with subsequent tidal evolution occurring on the stellar evolution timescale of the primary (e.g., Damiani & Lanza 2015). The conserved total angular momentum of the system, assumed aligned, is $J = L+S_1+S_2$, where $S_1 = I_1\Omega$ is the spin angular momentum of the primary, and S_2 is that of the secondary. Here I_1 is the moment of inertia of the primary, and Ω is the primary's angular velocity. Since the moment of inertia of the secondary I_2 is much smaller than I_1, we ignore S_2. In that case,

$$L + S_1 \simeq \text{constant}. \tag{4.2}$$

At each time t, $\Omega(t)$ is determined from the initial values $L(0)$ and $S_1(0)$ as $\Omega(t) = (L(0) + S_1(0) - L(t))/I_1(t)$. In this way a separate differential equation is not needed for Ω.

One technical point is that even a tiny amount of mass loss would cause an artificial spinup of the primary according to Equation 4.2, since L would decrease even at fixed a. To eliminate this issue, the two masses are fixed during the evolution. This is a good approximation for the stars near the base of the giant branch considered here, since little mass has been lost, and e.g., the expansion of the orbit would be tiny at this stage.

The viscous dissipation rate for incompressible flow is given by Landau & Lifshitz (1959)

$$\dot{E} = \frac{1}{2} \sum_{i=x,y,z} \sum_{k=x,y,z} \int \rho\nu \left(\frac{\partial v_i}{\partial x_k} + \frac{\partial v_k}{\partial x_i} \right)^2 d^3x \tag{4.3}$$

where the sums are over the three spatial directions, v_i is the velocity of the tidal flow, x_i are Cartesian coordinates, ν is the (isotropic) kinematic viscosity, and ρ is the mass density. Isotropic turbulent viscosity is assumed for simplicity. Numerical simulations find modest deviations from isotropy for Boussinesq convection (Penev

et al. 2009, 2011). The velocity of the tidal flow may be represented as a spherical harmonic expansion

$$\mathbf{v} = \sum_{\ell m} (-i\omega_m) \left[\xi_{r,\ell m}(r) Y_{\ell m}(\theta,\phi)\mathbf{e}_r + \xi_{h,lm}(r) r \boldsymbol{\nabla} Y_{\ell m}(\theta,\phi)\right] e^{-i\omega_m t} \tag{4.4}$$

where $\xi_{r,\ell m}$ and $\xi_{h,\ell m}$ are the radial and horizontal component of the Lagrangian displacement vector, and $\omega_m = m(n-\Omega)$ is the forcing frequency in the rotating frame. Plugging Equation 4.4 into Equation 4.3 and performing the angular integral gives

$$\begin{aligned}\dot{E} = &\frac{1}{2}\sum_{\ell m}\omega_m^2 \int_{r_{\rm bcz}}^{R_1} dr r^2 \rho\nu \Bigg[4\left(\frac{d\xi_{r,\ell m}(r)}{dr}\right)^2 + 2\ell(\ell+1)\left(\frac{d\xi_{h,\ell m}(r)}{dr} + \frac{\xi_{r,\ell m}(r)}{r} - \frac{\xi_{h,\ell m}(r)}{r}\right)^2 \\ &+ 2\left(\ell(\ell+1)\frac{\xi_{h,\ell m}(r)}{r} - 2\frac{\xi_{r,\ell m}(r)}{r}\right)^2\Bigg]\end{aligned} \tag{4.5}$$

where $r_{\rm bcz}$ is the radius at the base of surface convective zone. Since the $m = 0$ term has zero frequency it does not contribute. The $\pm m$ terms give equal contributions.

The tidal potential in the primary due to a secondary orbiting at co-latitude $\pi/2$ and and orbit angle $(n-\Omega)t$ is

$$\begin{aligned}U =& \sum_{\ell=2}^{\infty}\sum_{m=-\ell}^{\ell} U_{\ell m}(r) Y_{\ell m}(\theta,\phi) e^{-i\omega_m t} \\ =& -GM_2 \sum_{\ell=2}^{\infty}\sum_{m=-\ell}^{\ell} \frac{4\pi}{2\ell+1}\frac{r^\ell}{a^{\ell+1}} Y_{\ell m}\left(\frac{\pi}{2},0\right) Y_{\ell m}(\theta,\phi) e^{-i\omega_m t},\end{aligned} \tag{4.6}$$

which is smaller than the potential GM_1/R_1 at the surface of the primary by a small factor $\epsilon = (M_2/M_1)(R_1/a)^3$ for $\ell = 2$. In the equilibrium tide approximation (e.g.,

Goldreich & Nicholson 1977), the radial and horizontal displacements are

$$\xi_{r,\ell m}(r) = -\frac{U_{\ell m}(r)}{g}$$

and

$$\xi_{h,\ell m}(r) = -\frac{1}{\ell(\ell+1)}\frac{U_{\ell m}(r)}{g}\left(2\ell - \frac{d\ln g}{d\ln r}\right)$$

Given the run of ρ, ν, g, $\xi_{r,\ell m}$ and $\xi_{h,\ell m}$ versus r for a stellar model, $\dot{E}$ is computed by numerical integration of Equation 4.5 for a given stellar model. Analytic approximations for this integral are discussed in the Appendix.

When the turnover time $\tau_{\rm ed}$ of the large eddies becomes longer than the forcing period $P_f = P_{\rm orb}/2$ (for $m = 2$), it is expected than turbulent viscosity is reduced, since the large eddies cannot transport momentum efficiently. Three models of turbulent viscosity will be investigated: "standard" viscosity

$$\nu_{\rm std} = \frac{1}{3} v_{\rm ed} \alpha H, \tag{4.7}$$

Zahn's formula with a linear reduction

$$\nu_{\rm Z} = \nu_{\rm std} \times \min\left(1, \frac{P_f}{2\tau_{\rm ed}}\right), \tag{4.8}$$

and Goldreich and Nicholson's formula with a quadratic reduction

$$\nu_{\rm GN} = \nu_{\rm std} \times \min\left(1, \left(\frac{P_f}{2\pi\tau_{\rm ed}}\right)^2\right), \tag{4.9}$$

The numerical factors in each expression are somewhat arbitrary (Penev et al. 2009). Due to the large eddy velocity near the surface, the eddy turnover time will generally

be shorter than forcing periods of interest there. Reduced viscosity is important deep in the convection zone where eddy velocities are small, due to increasing density.

If the viscosity scales with orbital period $P_{\rm orb} = 2\pi/n$ as $\nu \propto P_{\rm orb}^{\alpha}$, then for $\Omega \ll n$, $\dot{E} \propto M_2^2 a^{-9+3\alpha/2} = M_2^2 a^{-(\beta+2)}$ and $\dot{a} \propto M_2 a^{-7+3\alpha/2} = M_2 a^{-\beta}$ with $\beta = 7 - 3\alpha/2$. The relevant values of β are then 7, 5.5 and 4 for standard, linear and quadratic scalings. The exponent β is a crucial parameter that directly determines the relative number of systems at different orbital separation.

4.2.1 A Numerical Example

For close-in orbits and deep stellar convection zones, the viscosity is expected to be significantly reduced from the standard value. This section shows a numerical example to illustrate the reduction factor. Figure 4.1 shows the depth dependence of turbulent viscosity (top panel), eddy turnover time and interior mass (middle panel), and $d\dot{E}/d\ln P$ from Equation 4.5 (bottom panel); here P is pressure. Representative values have been used, with a $M_1 = 1 M_\odot$ RGB star with radius $R_1 = 10 R_\odot$, companion mass $M_2 = 0.01\, M_\odot$, orbital separation $a = 0.1\,$AU and orbital period $P_{\rm orb} = 11.4$ days.

The middle panel of Figure 4.1 shows that this RGB star has eddy turnover times $\tau_{\rm ed} = \alpha_{\rm mlt} H/v_{\rm ed} \gtrsim 100\,$days near the peak of the integrand. Hence tidal forcing for any orbit shorter than $P_{\rm orb} \simeq 100\,$days is expected to have reduced viscosity. The peak in eddy turnover time is due to the scale height becoming small both near the surface, due to lower temperature, and toward the center, due to higher gravity.

Near the peak of the integrand the eddies are turning over 10 times slower than the tidal forcing period. The top panel shows that this leads to a reduction factor of 10^{-1} and 10^{-4} relative to standard viscosity, respectively. The bottom panel shows

that $d\dot{E}/d\ln P$ has a strong peak for standard viscosity, due to decreasing mass near the surface and decreasing tidal shear toward the interior. The integrands for Zahn and GN viscosities are reduced in size and with flattened peaks closer to the surface. The Zahn case still has a peak in the integrand well below the depth where $P_f = \tau_{\rm ed}$, however the GN case has a flat integrand over 3-4 decades in pressure, ending at $P_f = \tau_{\rm ed}$.

Appendix 4.7 discusses analytic approximations to the dissipation rate for the different assumptions for turbulent viscosity. This approximations will be used in Section 4.5 to understand the critical orbital separation out to which orbital decay is expected to have caused systems to merge.

4.3 Dynamical Tide Dissipation Rate

The dynamical tide involves the excitation of internal gravity waves near the RCB. If damping is weak, waves will reflect in the core and form standing waves. When the wave can be damped in less than one group velocity travel time the result is a traveling wave. In the traveling wave regime, the dissipation rate is given by the inward-going wave luminosity, $L_{\rm dyn}$.

During the SGB and RGB phases the core is radiative and the envelope convective. The dynamical tide is excited at the radiative-convective boundary (RCB), with the waves propagating inward toward the center (e.g., Goodman & Dickson 1998). There are two damping mechanisms that may cause the wave to damp at or before it reaches the center. First, radiative diffusion damping becomes progressively more important as the star evolves off the MS, due to the large number of internal gravity wave nodes in the core (Dziembowski 1977). This mechanism depends only on the orbital period, and is independent of the companion mass. Second, waves may "break" nonlinearly

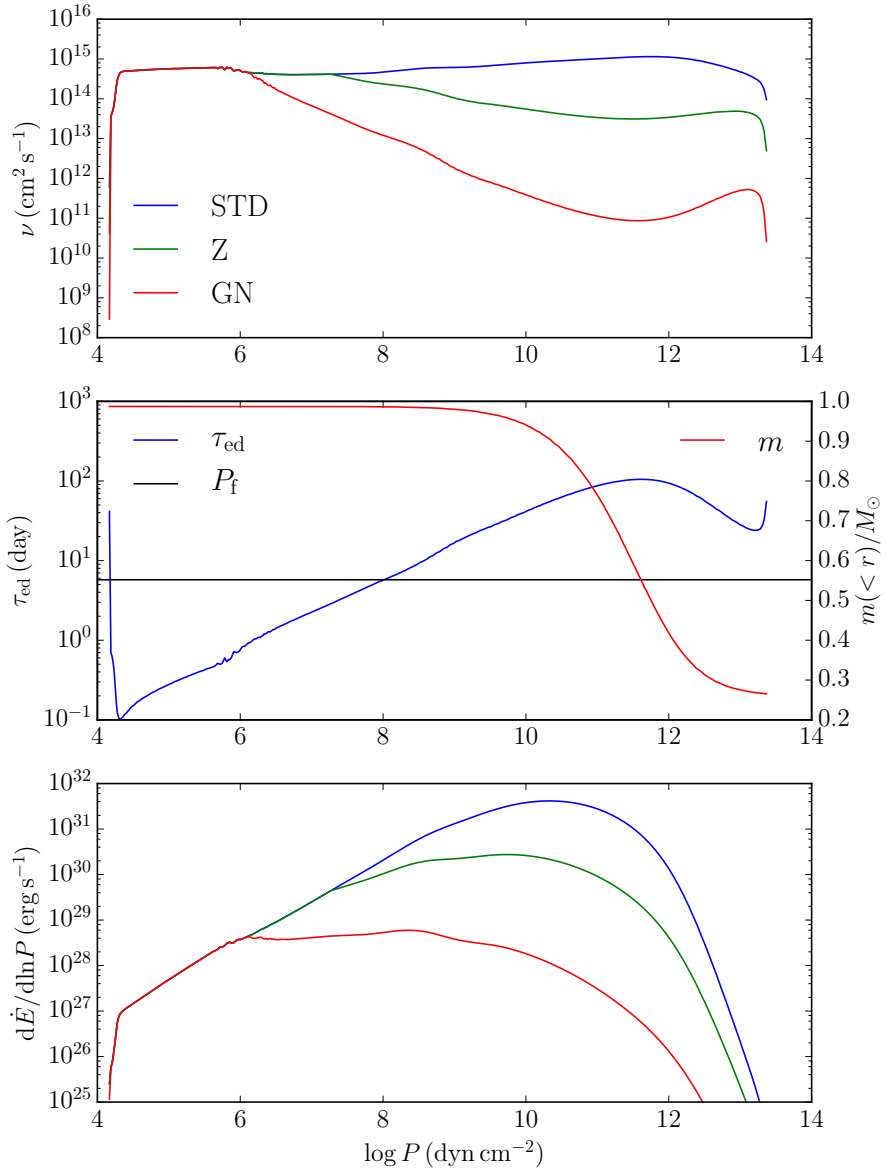

Fig. 4.1.— Depth dependence of quantities needed for the turbulent viscosity dissipation rate. The parameters used are a $M_1 = 1\,M_\odot$ RGB star with radius $R_1 = 10\,R_\odot$, companion mass $M_2 = 0.01\,M_\odot$, and separation $a = 0.1$ AU (orbital period $P_{\rm orb} = 11.4$ days). The top and bottom panels show the standard, Zahn and GN prescriptions as blue, green and red lines, respectively. The top panel shows the run of the three prescriptions for turbulent viscosity as a function of pressure in the convective envelope. The middle panel shows the eddy turnover time (blue solid line), forcing period ($P_{\rm orb}/2 = 5.7$ days, the black horizontal line) and interior mass $m(r)$ in terms of $\log P$. The bottom plot gives the integrand of the energy dissipation integral.

at the center, and not reflect back (Barker & Ogilvie 2010; Barker 2011). Here wave breaking may mean overturning the local stratification, or strong wave-wave interactions which transfer energy from the tidally-excited fluid motion to daughter waves (Weinberg et al. 2012; Barker & Ogilvie 2010; Barker 2011). Nonlinear wave breaking depends on the companion mass, as well as the orbital period.

The traveling wave luminosity is computed from stellar models by solving the linearized radial momentum and continuity equations and applying the appropriate boundary conditions for an inward-going traveling wave in the radiative zone. Define the radial Lagrangian displacement ξ_r, the potential $\psi = \delta p/\rho + U$, the Eulerian pressure perturbation δp, and the tidal potential U. The radial momentum equation and continuity equations, in the Cowling approximation, are then (e.g., Unno et al. 1989)

$$\frac{d\psi}{dr} = \frac{N^2}{g}\left(\psi - U\right) - (N^2 - \sigma^2)\xi_r \tag{4.10}$$

and

$$\frac{d\xi_r}{dr} = \xi_r\left(\frac{g}{c^2} - \frac{2}{r}\right) + \psi\left(\frac{k_h^2}{\sigma^2} - \frac{1}{c^2}\right) + \frac{U}{c^2}, \tag{4.11}$$

where the horizontal wavenumber is $k_h^2 = \ell(\ell+1)/r^2$. At the surface, the evanescent wave boundary condition applied is (Unno et al. 1989) $\delta p/\rho = \psi - U - g\xi_r$. The inward-going traveling wave boundary condition is

$$\frac{d\left(\psi - \psi_0\right)}{dr} = ik_r\left(\psi - \psi_0\right), \tag{4.12}$$

where ψ_0 is an approximate long-wavelength, particular solution and $k_r = k_h N/\omega$ is the radial wavenumber. The value of ψ_0 can be computed from the equilibrium tide

as (Arras & Socrates 2010; Weinberg et al. 2012, 2017)

$$\psi_0 = \frac{\omega^2}{\ell(\ell+1)} \frac{d(r^2 \xi_{\rm r,eq})}{dr}. \tag{4.13}$$

The dynamical tide pieces of ξ_r and ψ are denoted $\xi_{\rm r,dyn} = \xi_r - \xi_{\rm r,eq}$ and $\psi_{\rm dyn} = \psi - \psi_0$. In the gravity wave propagation zone, the traveling wave luminosity is given by

$$L_{\rm dyn} = r^2 \int d\Omega \rho \psi_{\rm dyn} \dot{\xi}_{\rm r,dyn}, \tag{4.14}$$

which involves an integral over two spherical harmonics. The purpose of subtracting the long-wavelength response is to decrease the size of the oscillatory part of the $L_{\rm dyn}(r)$, making it easier to isolate the value in the propagation zone far away from the RCB.

The decrease of gravity wave energy in the core due to radiative diffusion can be parametrized as

$$\alpha \equiv \frac{\dot{E}_{\rm diff}}{L_{\rm dyn}} \simeq 2 \int_0^{r_{\rm rcb}} dr \frac{k_h^3 N}{\omega^4} \nabla_{\rm ad} (\nabla_{\rm ad} - \nabla) \frac{4\sigma T^4 g^2}{3\kappa P^2} \equiv \left(\frac{P_{\rm orb}}{P_{\rm orb,diff}} \right)^4. \tag{4.15}$$

Here $\dot{E}_{\rm diff}$ is the dissipation rate including both the inward and outward going waves, giving the factor of 2 in Equation 4.15. The adiabatic and stellar temperature gradients are denoted $\nabla_{\rm ad}$ and ∇, respectively, and κ is the opacity. This formula was derived for the dynamical tide component using the low frequency, quasi-adiabatic approximation discussed in Unno et al. (1989), and is valid in the degenerate core and non-degenerate burning shell, where most of the contribution arises.

Outside $P_{\rm orb,diff}$, defined in Equation 4.15, radiative diffusion damping is strong,

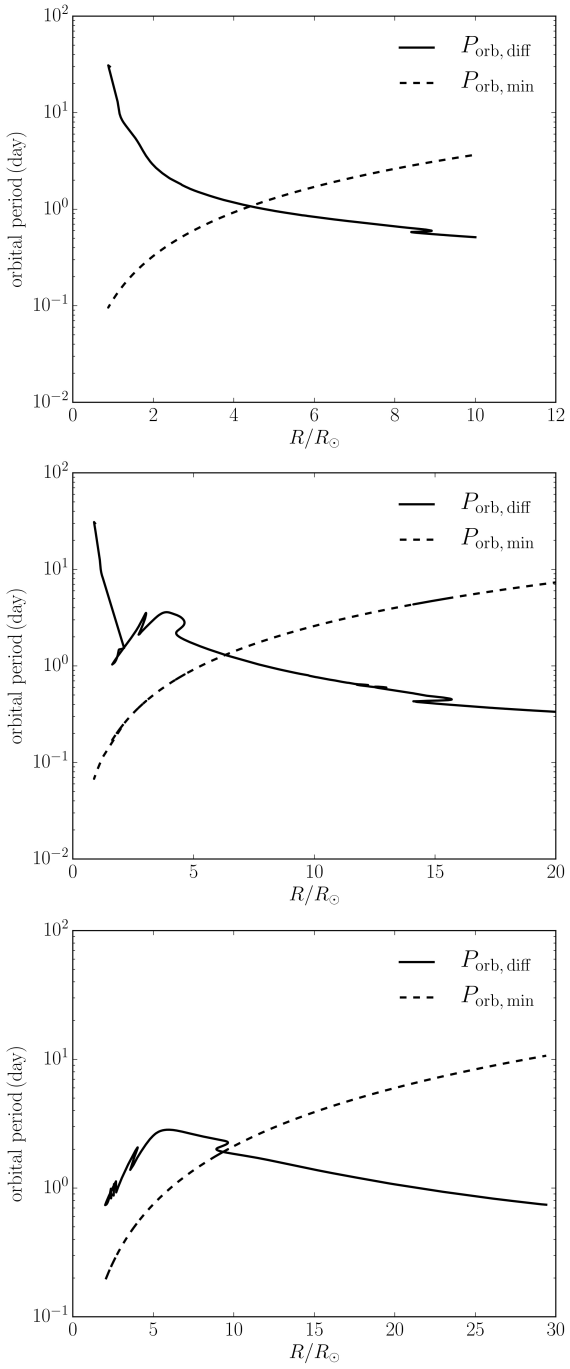

Fig. 4.2.— Critical orbital period during the evolution for stars of mass $M_1 = 1$ (top panel), 2 (middle panel), $3\,\mathrm{M}_\odot$ (bottom panel). The solid line shows the critical orbital period, $P_{\rm orb,\,diff}$ outside of which the radiative diffusion damping timescale is shorter than the group travel time in the core, and the traveling wave regime obtains. The dashed lines show the minimum possible orbital period $P_{\rm orb,\,min}$ for a star of that mass and radius, where the companion is orbiting at the surface of the star. At a given stellar radius, the standing wave limit can only occur if the dashed line is below the solid line.

and the traveling wave limit occurs, and vice versa for $P_{\rm orb} < P_{\rm orb,diff}$. Figure 4.2 shows the $P_{\rm orb,\,diff}$ versus stellar radius, R, which acts as a proxy for age. In all three cases, radiative diffusion will lead to the traveling wave limit for orbital periods $P_{\rm orb} \gtrsim 1\,{\rm day}$ over part of the SGB and all the RGB. This enhanced radiative diffusion is caused by the short vertical wavelength in the core.

Radiative diffusion may also have an important effect on the driving of waves at the RCB. For very thin surface convection zones in MS stars of mass $M_1 \gtrsim 1.3\,M_\odot$, the thermal time can become shorter than the forcing period, and radiative diffusion will rapidly damp out temperature differences induced by the wave, effectively eliminating the buoyancy force. The wave luminosity is expected to be suppressed when $\omega \lesssim \omega_{\rm diff}$, where the thermal diffusion frequency at the RCB is approximated as

$$\omega_{\rm diff} \simeq \frac{F}{\rho g \lambda^2}. \tag{4.16}$$

Here F is the flux and $\lambda \equiv |\ell(\ell+1)(dN^2/dr)/(\omega^2 r^2)|^{-1/3} \simeq H(\omega/c_s k_h)^{2/3}$ is the Airy wavelength of the gravity wave (Goodman & Dickson 1998). In this paper it is assumed that rapid thermal diffusion will greatly reduce the wave luminosity, so that it is set to zero when the thermal time $t_{\rm th} = PC_pT/gF$ is shorter than the forcing period $P_{\rm f}$. As the convective envelope rapidly deepens on the SGB, where $\omega_{\rm diff}$ decreases fast and $t_{\rm th}$ increases fast, $\omega = \omega_{\rm diff}$ and $t_{\rm th} = P_{\rm f}$ occur at almost the same stage during the evolution. Therefore, turning on the dynamical tides at $t_{\rm th} > P_{\rm f}$ is a good approximation. This effectively sets the inward-going wave luminosity to zero on the MS for the $M_1 = 2$ and $3\,M_\odot$ cases. As the star leaves the MS, the convection zone will deepen rapidly and hence our assumption allows the dynamical tide dissipation to turn on suddenly at the end of the MS. This effect is clearly evident in the results for the $M_1 = 2$ and $3\,M_\odot$ stars.

In the calculations of orbital decay in later sections, it is convenient to have tabulated formulas for the wave luminosity that can be rapidly evaluated, as opposed to solving the above boundary value problem. If $\lambda \simeq (\omega/ck_h)^{2/3} H$ is much smaller than the local scale height H, which is valid when the forcing frequency is much smaller than the Lamb frequency at the RCB, the Airy approximation is good and the wave luminosity can be written in the form (Goodman & Dickson 1998)

$$L_{\rm dyn} = \left(\frac{3^{2/3}\Gamma^2(1/3)}{2\pi}\right)[\ell(\ell+1)]^{-4/3}\omega^{11/3} \times \left(\rho r^5 \left|\frac{dN^2}{d\ln r}\right|^{-1/3} \frac{\zeta^2 \xi_{r,\rm eq}^2}{r^2}\right) \tag{4.17}$$

and where the dimensionless parameter ζ is defined by

$$\frac{d\xi_{\rm r,dyn}}{dr} \equiv \zeta \frac{\xi_{\rm r,eq}}{r}, \tag{4.18}$$

and ζ is set by matching the solution in the convection zone to that in the radiative zone. All the quantities in Equation 4.17 are evaluated at the RCB. Our numerical calculations find that ζ grows strongly during the RGB. Equating the analytical formula in Equation 4.17 to the numerical results generated from Equation 4.14 for each stellar model gives the parameter ζ. When applying Equation 4.17 in the calculations of orbital decay, the use of the Airy approximation on the radiative side of the RCB requires that the wavelength is always much shorter than a scale height. For closer orbits, the larger forcing frequency implies larger wavelengths, and the luminosity can be larger than implied by Equation 4.17, and this approach may underestimate the orbital decay rate. When both dynamical and equilibrium tides are included, the orbital decay rate becomes $\dot{a} = -2(\dot{E}_{\rm eq} + |L_{\rm dyn}|)/\mu n(n-\Omega)a$.

Equation 4.17 is only valid in the short wave length limit, where $\lambda \ll H$ at RCB. For closer orbits, ω increases and λ can approach H. Equation 4.17 will *underestimate*

$L_{\rm dyn}$ for these close orbits, and the orbital decay rate would be larger than in the results presented here.

Given $L_{\rm dyn}$, the nonlinearity of the wave must be checked by evaluating

$$k_r \xi_{r,\rm dyn} = \sqrt{\frac{[\ell(\ell+1)]^{3/2} N L_{\rm dyn}}{4\pi\rho r^5 \omega^4}} \tag{4.19}$$

in the radiative zone. If $\alpha > 1$, or if $\alpha < 1$ but $k_r \xi_{r,\rm dyn} > 1$, the dissipation rate is given by the full $|L_{\rm dyn}|$. On the other hand, if $\alpha < 1$ and $k_r \xi_{r,\rm dyn} < 1$, the dissipation rate is set as zero as the wave reflects back and forms a standing wave, with much smaller dissipation rate.

4.4 Examples of Orbital Decay

This section presents calculations of orbital decay for a range of primary mass, secondary mass and initial separation. Each integration of the equation $\dot{a} = -2(\dot{E}_{\rm eq} + |L_{\rm dyn}|)/\mu n(n-\Omega)a$ includes the dynamical tide, as well as a prescription for the turbulent viscosity used to damp the equilibrium tide. Calculations using standard, Zahn and Goldreich-Nicholson viscosity are compared to assess if they result in potentially detectable differences in the critical separation for rapid orbital decay. The range of substellar companion masses is chosen to span the range of synchronized and non-synchronized cases. The range of primary masses and evolutionary state post-MS represent the bulk of binaries with SGB and RGB primaries and a substellar secondary.

Modules for Experiments in Stellar Astrophysics (MESA, version 8845, Paxton et al. 2011, 2013, 2015) is used to provide the stellar structure for three stars of mass $M_1 = 1, 2$ and $3\,M_\odot$ during the MS, and ending when the stellar radius is 10 times

the MS value. The initial metallicity is $Z = 0.02$. The type 2 opacity table is used. The nuclear burning network used is "o18_and_ne22.net". The mixing length factor is 2. The Schwarzschild criterion for the definition of the convective zone is applied.

In the following three sections, results are presented for the three different primary masses.

4.4.1 $M_1 = 1\,M_\odot$

Sun-like stars have a radiative core and a relatively thick convective envelope on the MS, allowing the ingoing-wave dynamical tide to operate. The convection zone deepens significantly on the RGB in both mass and radius, giving rise to equilibrium tide dissipation rates many orders of magnitude larger than on the MS. At fixed semi-major axis, the dynamical tide increases strongly during the SGB, and is relatively constant on the RGB.

The top panel of Figure 4.3 shows the evolution of a for a $M_1 = 1M_\odot$ primary and a $M_2 = 0.01M_\odot$ secondary, including dynamical tides and equilibrium tides with standard viscosity, $\nu_{\rm std}$. The surface gravity, $\log g \equiv \log_{10}(g/({\rm cm\,s^{-2}}))$ is a proxy for the evolutionary state of the primary star from the MS phase ($\log g = 4.5$) to the RGB ($\log g \ll 4.5$). When the orbital decay rate is small, a is constant. Since the orbital decay rate increases so rapidly after the MS, the orbit will decay rapidly compared to the stellar evolution timescale, and the line will become nearly vertical. The system merges at the end of the MS for $a_{\rm ini} = 0.05$ AU, at the early RGB phase for $a_{\rm ini} = 0.125$ AU and at the middle RGB phase for $a_{\rm ini} = 0.2$ AU. From the middle panel, none of the examples synchronize for this relatively low companion mass (starting from $\Omega = 0$). The bottom panel shows the dynamical tide wave luminosity $L_{\rm dyn}$ and the equilibrium tide energy dissipation rate $\dot{E}_{\rm eq}$ during the evolution. For the case of

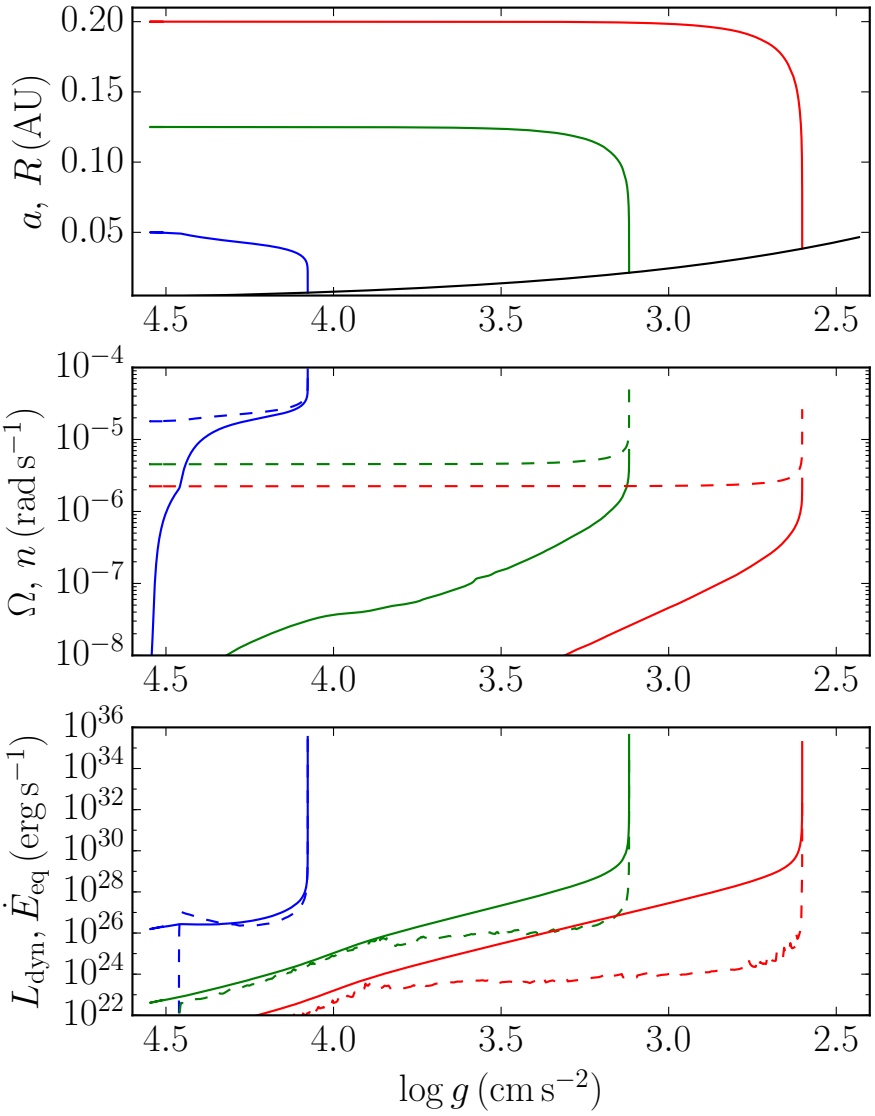

Fig. 4.3.— Orbital decay for a $M_1 = 1\,M_\odot$ primary, with companion mass $M_2 = 0.01\,M_\odot$ and initial separations $a = 0.05$ (blue), 0.125 (green) and 0.2 (red) AU. Here $\log g$ of the primary star shows the evolution of the star, from left to right. (Top panel) Semi-major axis vs $\log g$. The black line shows the stellar radius, R_1. (Middle panel) Primary rotation rate (Ω, solid lines) and binary orbital frequency (n, dashed lines). (Bottom panel) Dynamical tide ($|L_{\mathrm{dyn}|}$, dashed lines) and standard viscosity (ν_{std}) equilibrium tide ($\dot{E}_{\mathrm{eq}}$, solid lines) dissipation rates.

$a_{\rm ini} = 0.05$ AU, $L_{\rm dyn} > \dot{E}_{\rm eq}$ when the internal gravity wave breaks nonlinearly near the star center, and $\dot{E}_{\rm eq}$ dominates later. The $a_{\rm ini} = 0.125$ and 0.2 AU cases are both dominated by the equilibrium tide.

There are two trends that favor the equilibrium tide over the dynamical tide for wider orbits. First, they have different dependence on orbital period, with $L_{\rm dyn} \propto P_{\rm orb}^{-7.67}$ and $\dot{E}_{\rm eq} \propto P_{\rm orb}^{-6}$, so the latter decreases outward more slowly. Second, the dynamical tide luminosity has an initial increase by several orders of magnitude during the SGB, but then becomes relatively constant during the RGB (at fixed semi-major axis). This is in contrast to the equilibrium tide, which shows a continuous increase up the RGB. Hence for decay of wider orbits, which occurs for a more evolved primary star, the equilibrium tidal friction is more important.

Next, Figure 4.4 compares the orbital decay for a $M_1 = 1\,M_\odot$ primary with three different companion masses. For the low mass companion, $M_2 = 10^{-3}\,M_\odot \simeq 1\,M_{\rm Jup}$, $\dot{a} \propto M_2$ leads to a small orbital decay rate, and the spin is far from synchronous. By comparison, the $M_2 = 0.01 M_\odot$ case is also not synchronized, but the orbital decay occurs faster due to the larger mass. The higher mass, $M_2 = 0.2\,M_\odot$ case would have had even stronger orbital decay, if synchronization did not occur. However, this system synchronizes on the SGB, after which point the orbit evolves on the much slower stellar evolution timescale, so that this case actually lives *longer* than the two lower mass cases. The lower panel of Figure 4.4 shows that destruction occurs due to the Darwin instability, at separation $a_{\rm D} \simeq (3I_1/\mu)^{1/2} \simeq (3I_1/M_2)^{1/2}$ and orbital frequency $n_{\rm max} \simeq \sqrt{G(M_1+M_2)/a_{\rm D}^3} \simeq \sqrt{GM_1/a_{\rm D}^3}$. [1] Beyond this point, the spin has larger angular momentum than the orbit, and the orbital frequency will tend to increase rapidly, leaving the spin frequency behind. Hence the critical semi-major

[1] The critical separation can be derived by solving for the separation where $\partial J/\partial n = 0$ assuming $\Omega = n$.

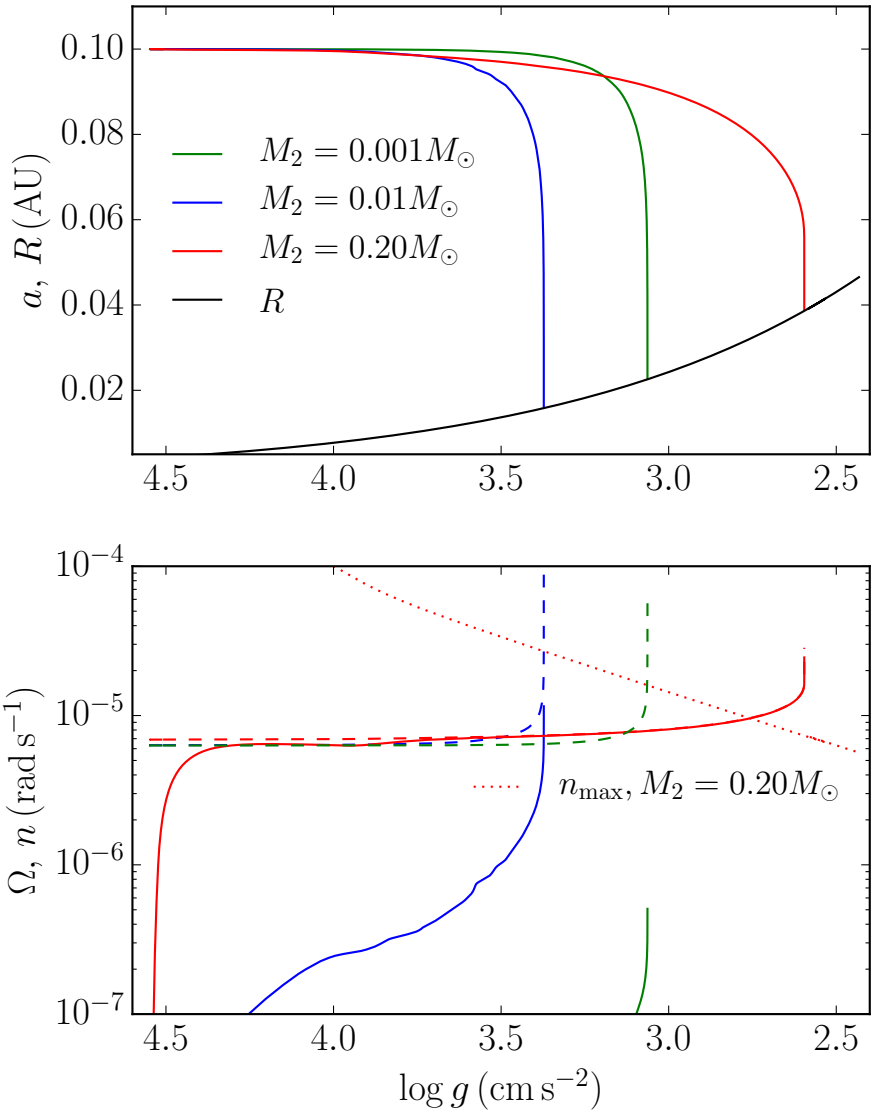

Fig. 4.4.— The effect of synchronous rotation on orbital decay for $M_1 = 1\,M_\odot$, $M_2 = 0.001$ (green lines), 0.01(blue lines) and $0.2\,M_\odot$ (red lines). (top panel) Semi-major axis (a) versus evolutionary state of the primary ($\log g$), and stellar radius. (bottom panel) Primary rotation rate (Ω), orbital frequency (n) and orbital frequency at which the Darwin instability begins ($n_{\rm max}$), evaluated for secondary mass $M_2 = 0.2\,M_\odot$.

axis out to which orbits are destroyed is not a monotonic function of M_2; for small M_2 it increase, while for large M_2 it decreases. This will be shown analytically in Section 4.5.

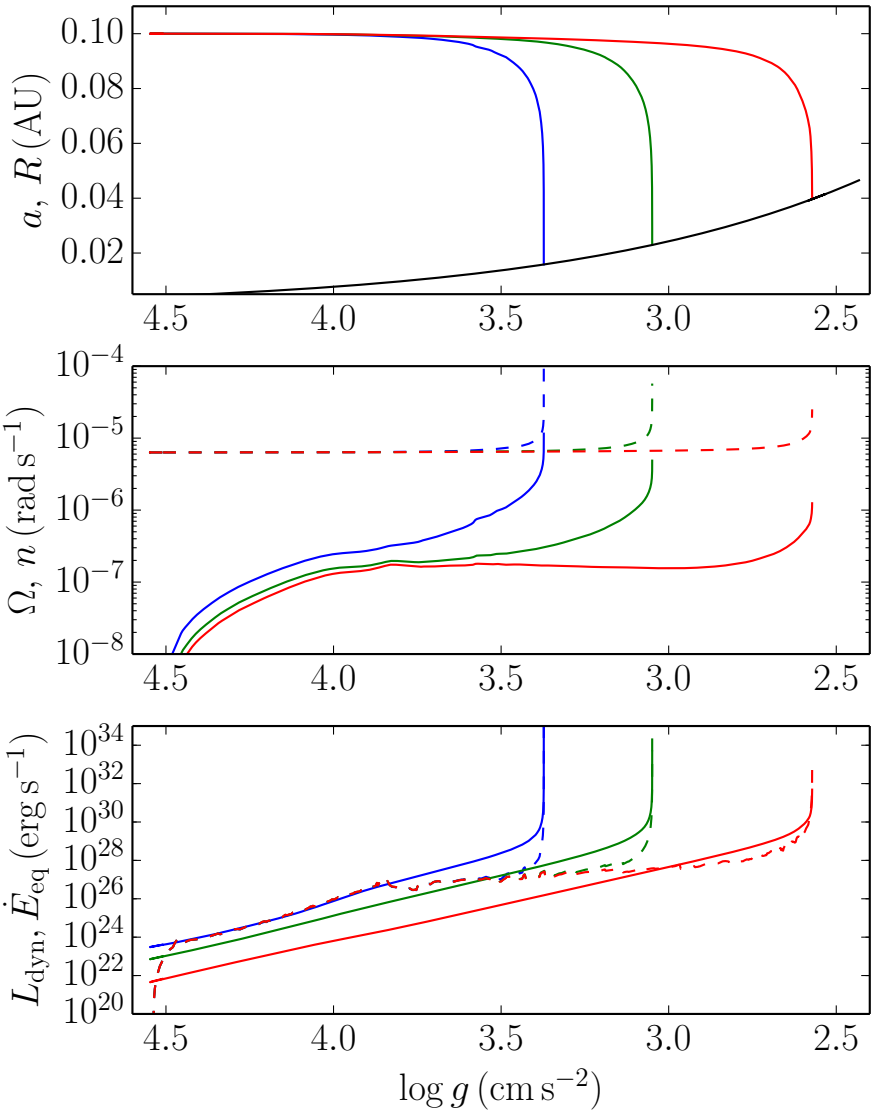

Fig. 4.5.— A comparison of a versus log g applied with the three descriptions on the kinematic viscosity: standard (blue), Zahn (green), GN (red). The black solid line shows R_1. The primary star mass is $M_1 = 1M_\odot$, the companion mass is $M_2 = 0.01M_\odot$, and $a_{\rm ini} = 0.1$ AU.

Figure 4.5 compares the evolution for the three different prescriptions for the turbulent viscosity. The dynamical tide is included in all three runs. As expected, for the non-synchronized case, reduced viscosity slows the orbital decay allowing systems to live longer. The difference in $\log g$ where the system merges is $\Delta(\log g) \simeq 0.3 - 0.8$ between standard and Zahn, and Zahn and GN viscosity. The reduction in $\dot{E}_{\rm eq}$ will typically lead to an early phase dominated by the dynamical tide, and if the star climbs sufficiently far up the RGB before merger, a later phase dominated by reduced equilibrium tide. Note again that $L_{\rm dyn}$ is nearly constant during the RGB phase.

4.4.2 2 $M_\odot$ Model

For $M_1 = 2\,M_\odot$, the star has a convective core on the MS, which inhibits nonlinear wave breaking at the center. [2] More importantly, the surface convection zone is so thin that radiative diffusion damping suppresses the driving of the wave. On the SGB, the core becomes radiative and the surface convection zone deepens, at which point both efficient excitation and nonlinear wave breaking can occur.

Figure 4.6 shows the evolution for $M_1 = 2\,M_\odot$ and $M_2 = 0.01 M_\odot$ starting from $a_{\rm ini} = 0.05$, 0.15 and 0.25 AU. Standard viscosity is used, and the dynamical tide is included. The bottom panel shows that $L_{\rm dyn} = 0$ until $\log g = 3.5$, where the surface convection zone deepens and $t_{\rm th} > P_{\rm f}$. Further $\dot{E}_{\rm eq}$ is much smaller than the $M_1 = 1\,M_\odot$ case on the MS, due to the smaller convection zone. The end result is that tidal friction in this model is much weaker than the $M_1 = 1\,M_\odot$ model on the MS, but comparable on the SGB and RGB. The middle panel shows that none of the cases synchronize for this companion mass. In the top panel, for $a_{\rm ini} = 0.25$ AU, the system merges at $\log g = 2.5$, where the features in the red line occur at dredge-up,

[2] An outward traveling wave flux excited at the radiative-convective boundary of the central convection zone is ignored in this paper.

where the convective envelope reach the hydrogen burning shell. In Figure 4.7, the z-shape in $n_{\max}$ near $\log g = 3.5 \sim 3.4$ occurs between central hydrogen exhaustion and shell ignition, where the star first shrinks and then expands. In the bottom panel,

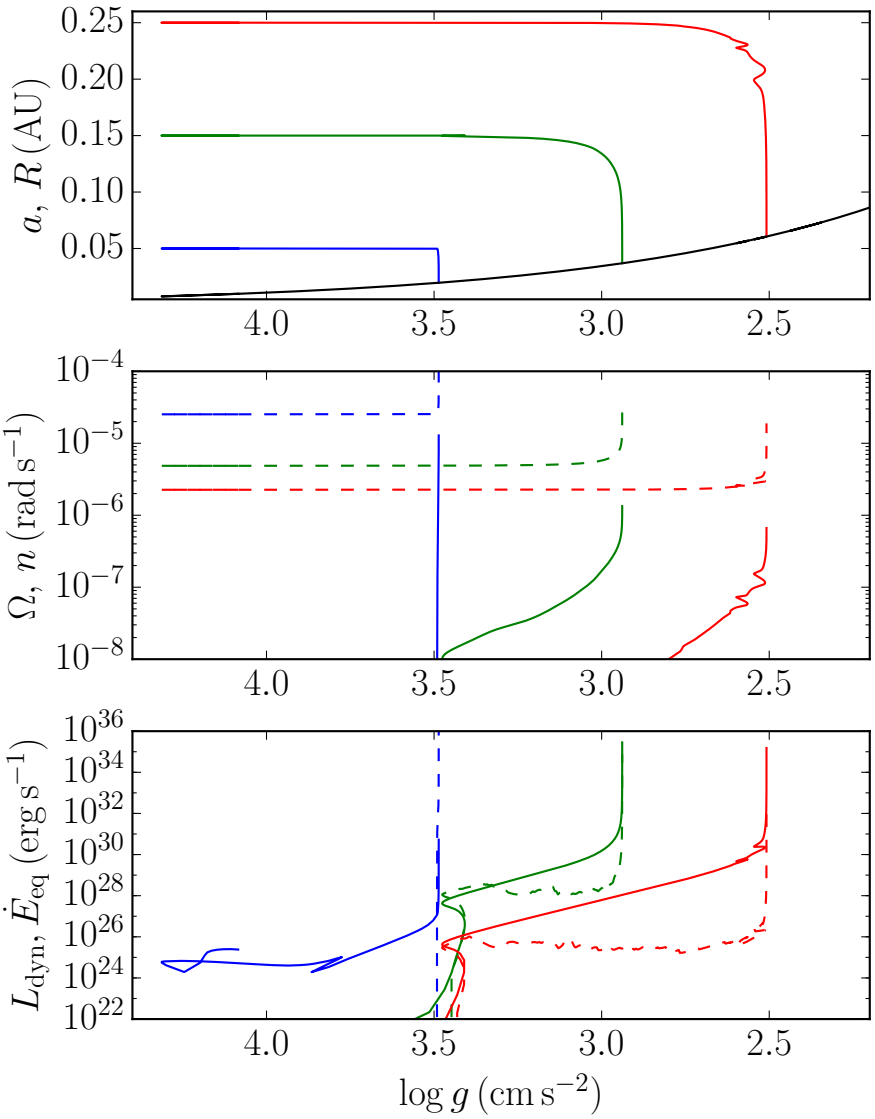

Fig. 4.6.— Same as Figure 4.3 but with $M_1 = 2\,M_\odot$, $M_2 = 0.01\,M_\odot$ and $a_{\rm ini} = 0.05$ (blue lines), 0.15 (green lines) and 0.25 (red lines) AU.

$L_{\rm dyn}$ dominates by orders of magnitude in the $a = 0.05\,{\rm AU}$ case once it turns on. This causes the immediate decay of the orbit seen in the top plot. For the $a = 0.15$ and $0.25\,{\rm AU}$ cases, dynamical tides are important only briefly after they turn on, and the equilibrium tide then dominates to merger.

Figure 4.7 again uses $M_1 = 2\,M_\odot$ and compares tracks with $M_2 = 0.001, 0.01$ and $0.5\,M_\odot$ for $a_{\rm ini} = 0.15\,{\rm AU}$. Similar to the $M_1 = 1\,M_\odot$ case, the two low mass cases are not synchronized while the higher mass case is synchronized until the Darwin instability.

Figure 4.8 shows the effect of reduced viscosity for the runs with the $M_1 = 2\,M_\odot$ primary. The same trends are apparent as in Figure 4.5, except that both dynamical and equilibrium tide dissipation only turn on for $\log g \lesssim 3.5$ where the convection zone deepens.

4.4.3 3 $M_\odot$ Model

The $M_1 = 3\,M_\odot$ case is qualitatively similar to that of $M_1 = 2\,M_\odot$. Tidal dissipation is suppressed during the MS, effectively turning on when the convective envelope thickens near $\log g \simeq 3.0$ on the sub-giant branch.

The bottom panel of Figure 4.9 shows that the dynamical tide is much bigger than equilibrium tide when it turns on, and immediately causes both the $a = 0.05$ and $0.15\,{\rm AU}$ orbits to decay. Only the $a = 0.25\,{\rm AU}$ orbit is sufficiently wide that the star has time to move up the RGB and equilibrium tides can dominate. None of the cases have synchronous spin for this companion mass (middle panel).

Figure 4.10 shows a close-up of the dissipation rates in the bottom panel of Figure 4.9. For the $M_2 = 0.001\,M_\odot$ (blue lines) and $M_2 = 0.01\,M_\odot$ (green lines) cases, the dynamical tide (dashed lines) dominates the equilibrium tide (solid lines) as soon as

it turns on. For the $M_2 = 0.5\,M_\odot$ case (red lines) $L_{\rm dyn}$ and $\dot{E}_{\rm eq}$ stay closer to each other.

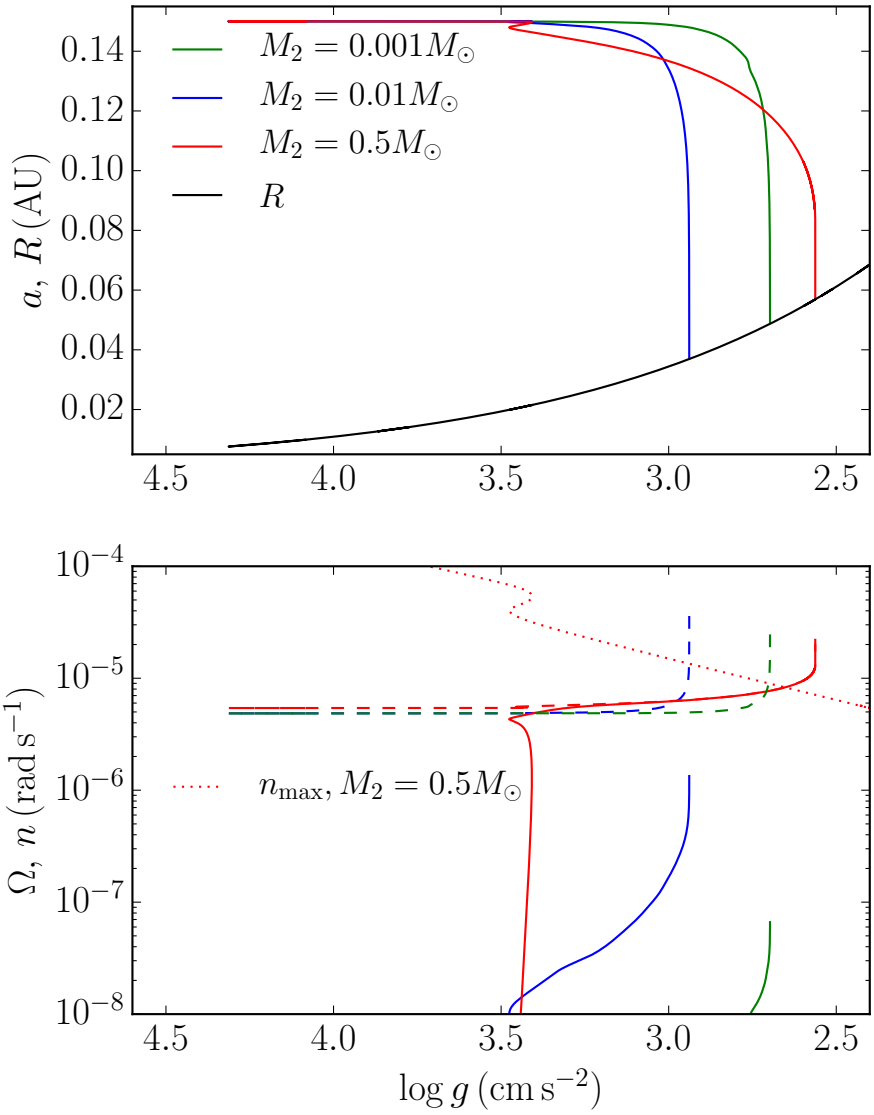

Fig. 4.7.— Same as Figure 4.4 but with $M_1 = 2\,M_\odot$, and $M_2 = 0.001$ (green), 0.01 (blue) and 0.5 (red), and starting separation $a_{\rm ini} = 0.15\,\mathrm{AU}$. In the lower panel, the green dotted line displays the orbital frequencies above which the Darwin instability occurs ($n_{\rm max}$), evaluated with $M_2 = 0.5 M_\odot$.

Figure 4.11 again compares the evolution with standard viscosity and including the dynamical tide for three different companion masses. All three cases merge over a small range of $\log g$ soon after the dynamical tide turns on. For the most massive $M_2 = 0.5\,M_\odot$ companion, in spite of the fact that the spin becomes synchronous, the

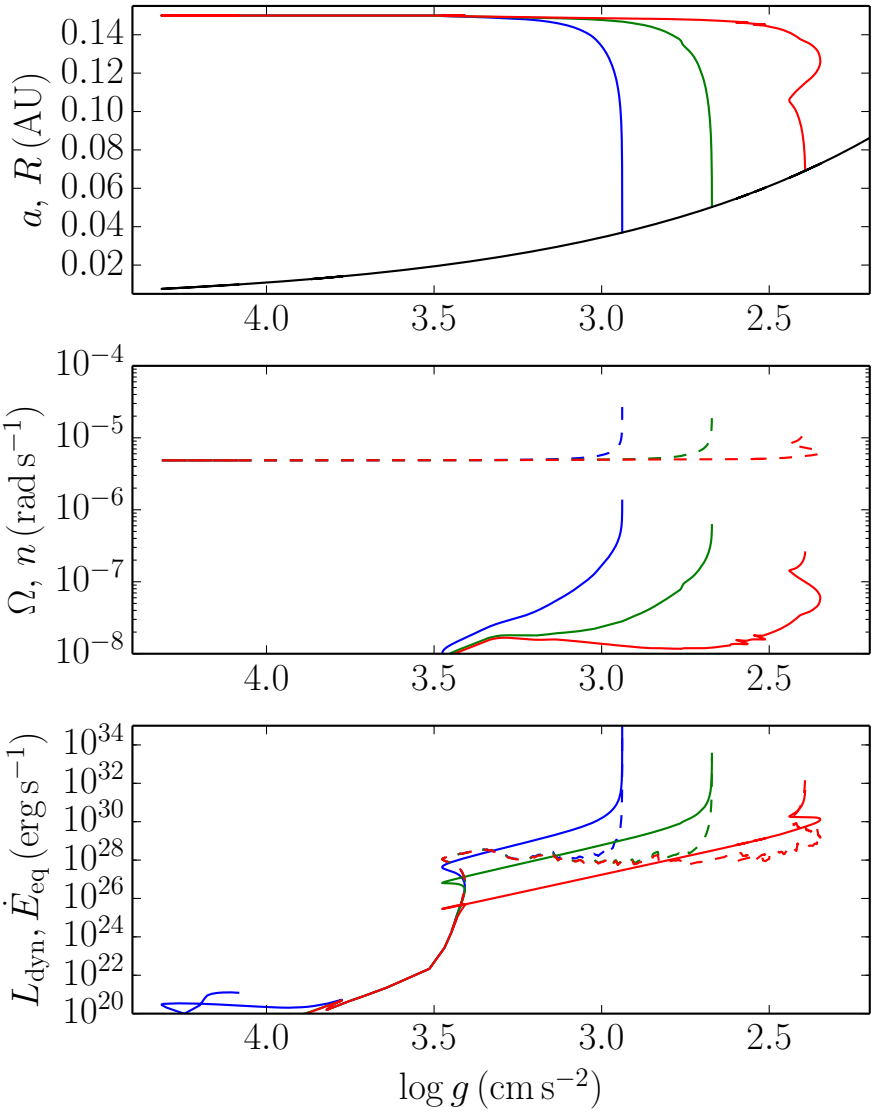

Fig. 4.8.— Same as Figure 4.5 but for $M_1 = 2\,M_\odot$ and $a_{\mathrm{ini}} = 0.15\,\mathrm{AU}$.

binary is still short lived since the Darwin instability turns on at roughly the same time.

Figure 4.12 shows the effect of the three prescriptions for turbulent viscosity, also

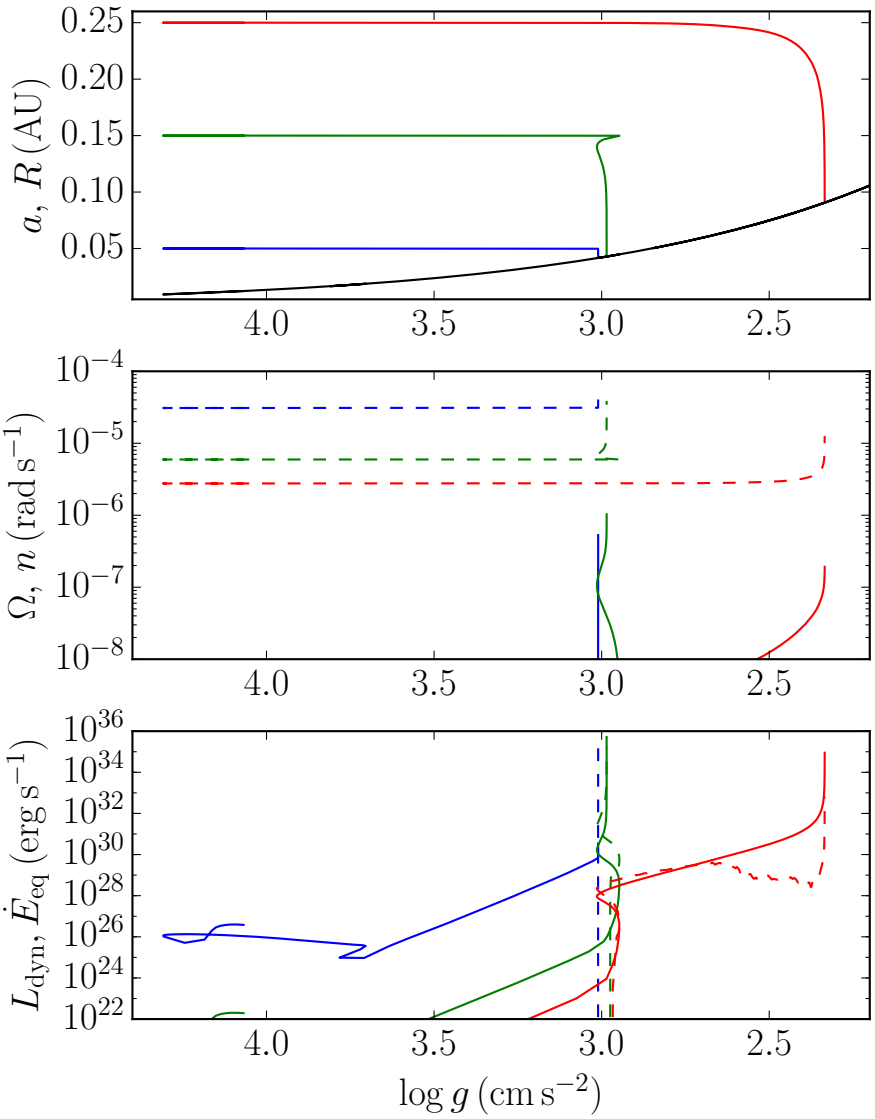

Fig. 4.9.— Same as Figure 4.3 but with $M_1 = 3\,M_\odot$, $M_2 = 0.01\,M_\odot$ and $a_{\rm ini} = 0.05$ (blue lines), 0.15 (green lines) and 0.25 (red lines) AU.

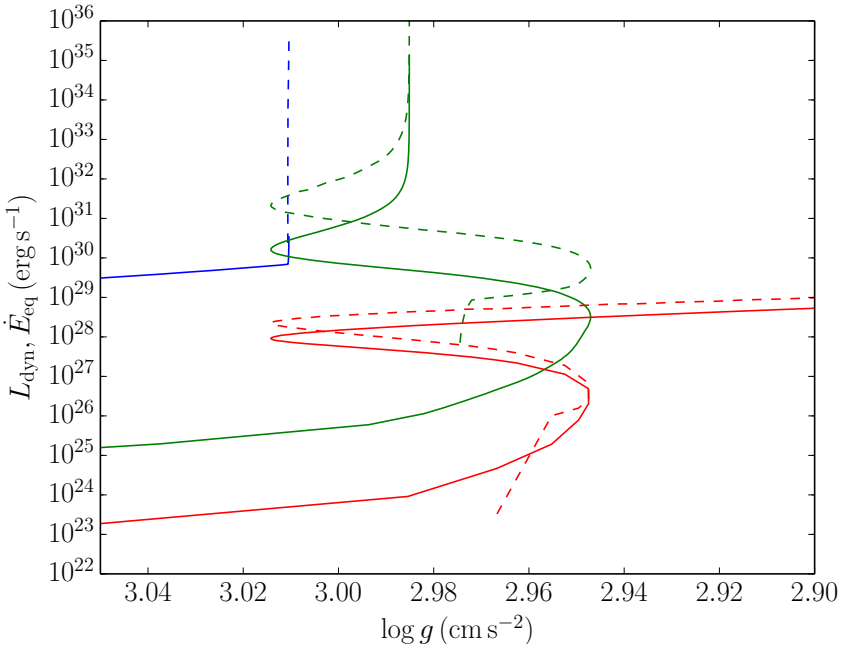

Fig. 4.10.— Close-up of the bottom panel of Figure 4.9, near where the convective envelope deepens and tidal friction increases dramatically.

including the effect of the dynamical tide. For the $M_1 = 3\,M_\odot$ and $M_2 = 0.01\,M_\odot$ case, as soon as the dynamical tide turns on it is dominant in all three cases, and so all three merge near the same $\log g$.

4.5 Critical Semi-major Axis for Mergers

Examples of orbital decay were shown in Section 4.4 to understand the importance of the turbulent viscosity prescription, the strength of dynamical versus equilibrium tide, and synchronous spin at each stage in a star's evolution. In this section, calculations of the "critical radius", $a_{\rm crit}(t)$, which depends on the age of the system, are presented. The critical radius is defined as the separation out to which orbits would have decayed down to the surface of the primary by the age t. Few binaries are expected to be

found with $a \lesssim a_{\rm crit}(t)$ since those orbits should have decayed and the binary already merged, while binaries with $a \gtrsim a_{\rm crit}$ are relatively unaffected by orbital decay. Hence

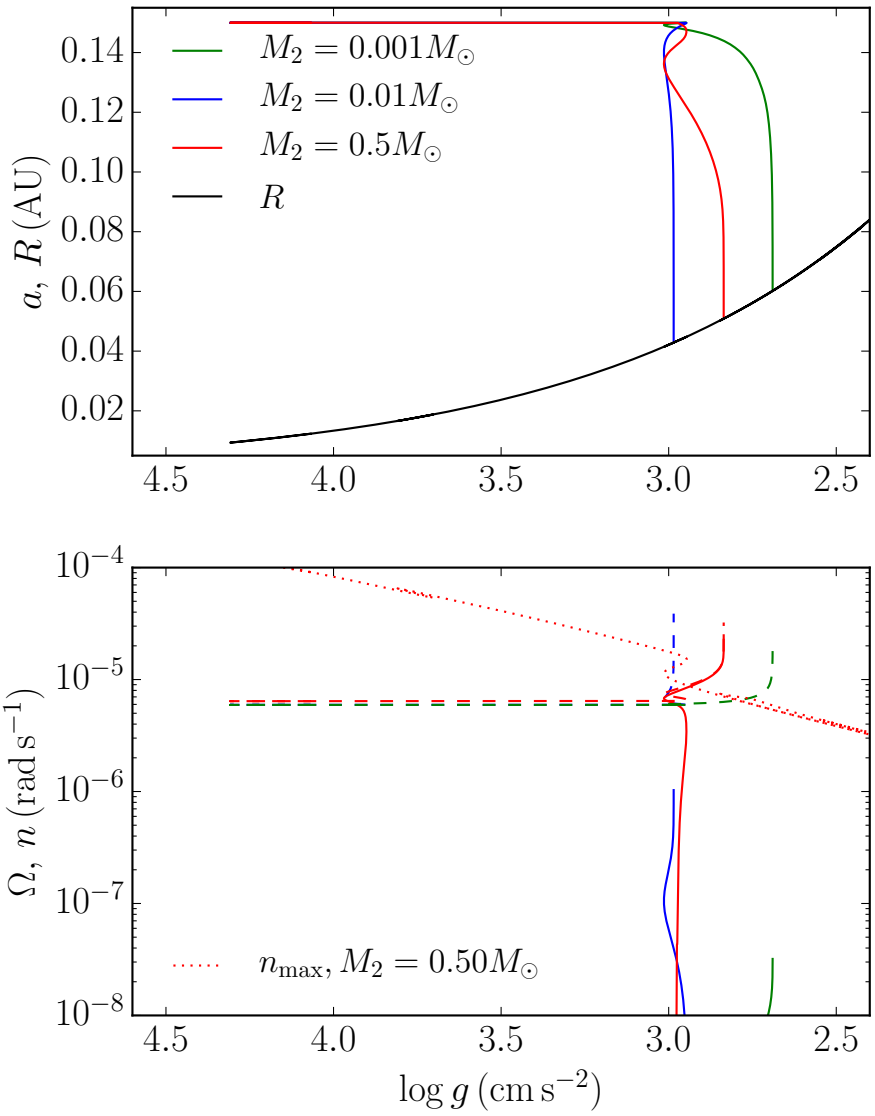

Fig. 4.11.— Same as Figure 4.4 but with $M_1 = 3\,M_\odot$, and $M_2 = 0.001$ (green), 0.01 (blue) and 0.5 (red), and starting separation $a_{\rm ini} = 0.15\,\mathrm{AU}$. In the lower panel, the green dotted line displays the orbital frequencies above which the Darwin instability occurs ($n_{\rm max}$), evaluated with $M_2 = 0.5 M_\odot$.

if a lack of systems is observed for some range of semi-major axis, the plot of $a_{\rm crit}$ versus $\log g$ shows which range might be absent of binaries due to tides, and for which range the lack of systems must have some other explanation as tides become ineffective.

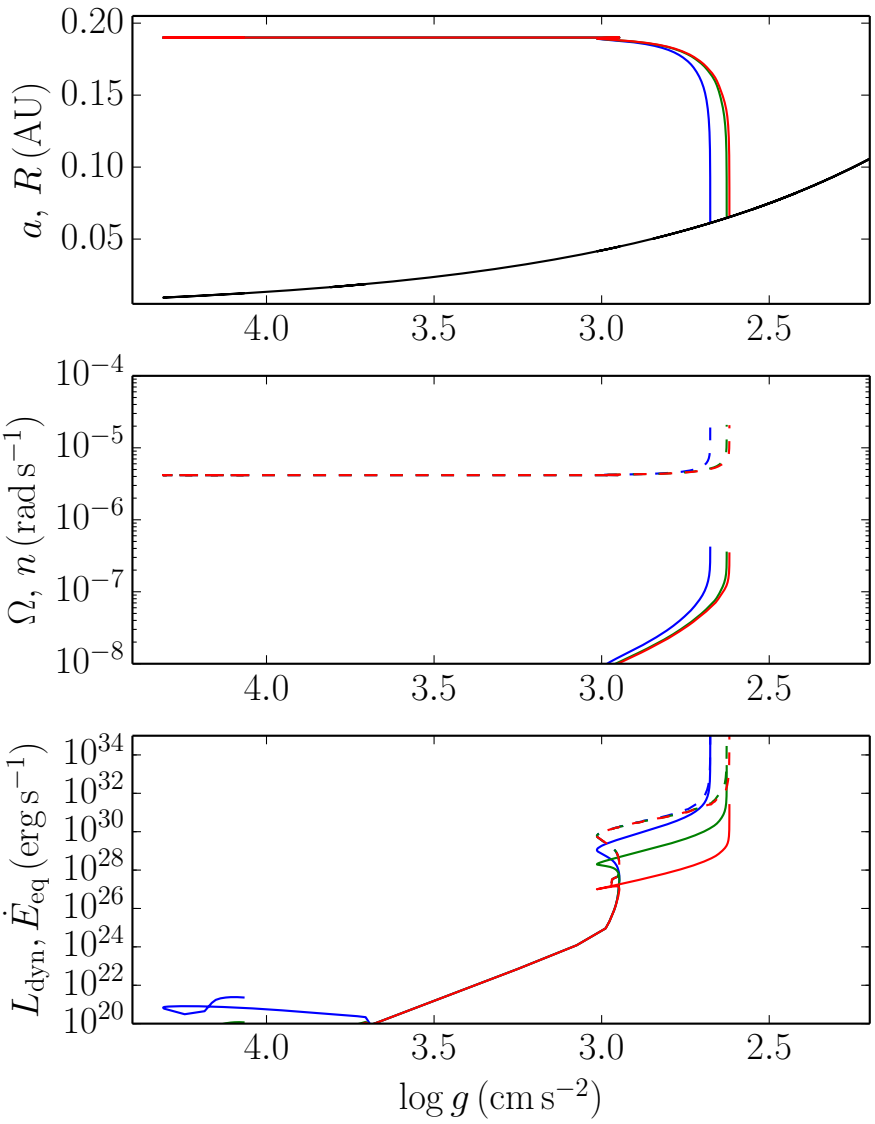

Fig. 4.12.— Same as Figure 4.5, but with $M_1 = 3\,M_\odot$, $M_2 = 0.01\,M_\odot$, and $a_{\rm ini} = 0.19$ AU.

Figures 4.13, 4.14 and 4.15 show $a_{\rm crit}$ versus $\log g$ for a primary mass of $M_1 = 1, 2, 3\,M_\odot$, respectively. The different lines in each plot are for different secondary masses, M_2. Zahn's prescription for reduced viscosity will be used in all plots, since reduced viscosity was found to greatly slow down orbital decay for the close orbits of interest. This reduces to standard viscosity when eddy turnover times are short. Numerical results will be presented first, and then analytic formulae for $a_{\rm crit}$ in order to understand the scalings, and which friction mechanism is dominant. The comparison below between the $a_{\rm crit}$ and data is also an extension of Chernov et al. (2017), where five systems containing hot Jupiters are investigated with orbital decay by the dynamical tide. Our computing of $a_{\rm crit}$ is considered with both equilibrium tides and dynamical tides.

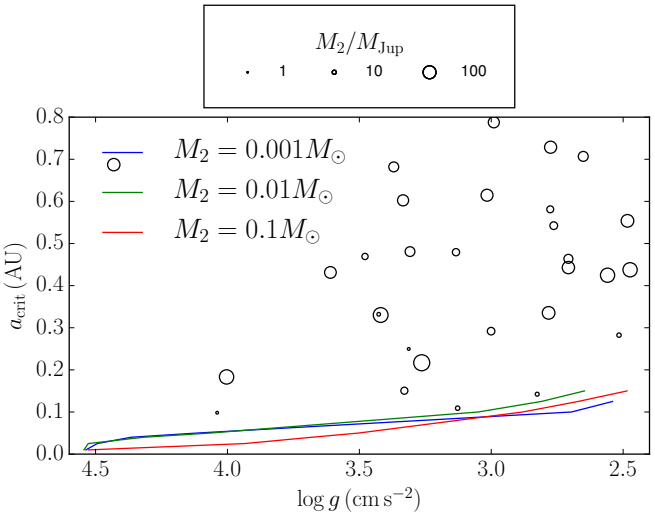

Fig. 4.13.— The critical semi-major axis $a_{\rm crit}$ versus $\log\, g$ for $M_1 = 1M_\odot$ with three companion masses: $M_2 = 0.001M_\odot$ (blue), $M_2 = 0.01M_\odot$ (green) and $M_2 = 0.1M_\odot$ (red). The black dots are the APOGEE data (Troup et al. 2016), with M_1 between $0.5M_\odot$ and $1.5M_\odot$, and M_2 between $1M_{\rm Jup}$ - $100M_{\rm Jup}$. Note that for extremely small $a_{\rm init}$, $M_2 = 0.001$ - $0.1\,M_\odot$ would suffer orbital decay before the end of the MS, and well before the RGB. This corresponds to the $a_{\rm init}$ lines on the bottom left of the figure.

Figure 4.13 compares calculations of $a_{\rm crit}$ versus $\log g$ for $M_1 = 1 M_\odot$. These calculations are compared to data from the APOGEE survey (Troup et al. 2016) for primary stars in the mass range $M_1 = 0.8$ - $1.5\,M_\odot$. All the observed systems have $a > a_{\rm crit}$, meaning that the orbital decay rate is small compared to the stellar evolution timescale. The lack of systems at $a < a_{\rm crit}$ may be interpreted as either the population of closer systems with $a < a_{\rm crit}$ have already merged due to orbital decay, or such close binary systems are rare or never formed in the first place.

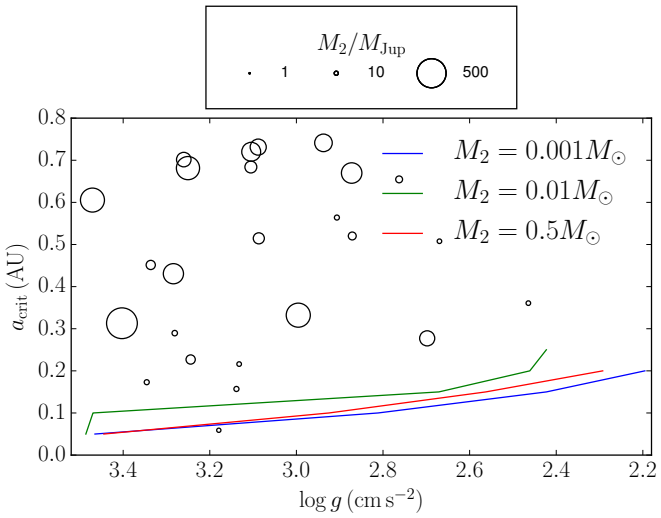

Fig. 4.14.— Same as Figure 4.13 for $M_1 = 2 M_\odot$ and $M_2 = 0.001$ (blue), 0.01 (green) and $0.5 M_\odot$ (red). The black dots are the APOGEE data (Troup et al. 2016), with $M_1 = 1.5$ - $2.5 M_\odot$ and $M_2 = 1$ - $500 M_{\rm Jup}$.

Figure 4.14 shows the $M_1 = 2 M_\odot$ case. Due to the thin surface convection zone, and a central convection zone, dynamical tides are assumed ineffective on the MS. The surface convection zones deepens near $\log g \simeq 3.5$, at which point both dynamical and equilibrium tides increase dramatically. This causes rapid orbital decay over a range of small orbital separation. At $a_{\rm crit} = 0.05$ AU, dynamical tides rapidly shrink the orbit, and even the high mass companions can't synchronize the orbit within the

short time orbital decay scale. Therefore the $a_{\rm crit}$ lines for the three M_2 are close. At $a_{\rm crit} = 0.1$ AU for the $M_2 = 0.01 M_\odot$ secondary, dynamical tides are still strong and the orbit shrinks at $\log g = 3.5$. Slow orbital decay occurs both for the high mass companion, due to synchronous spin, and low mass companions due to the weak tidal force. All but one of APOGEE systems have $a \geq a_{\rm crit}$, again showing that the $a \leq a_{\rm crit}$ systems, especially with $\log g \lesssim 3.5$, may have already been destroyed.

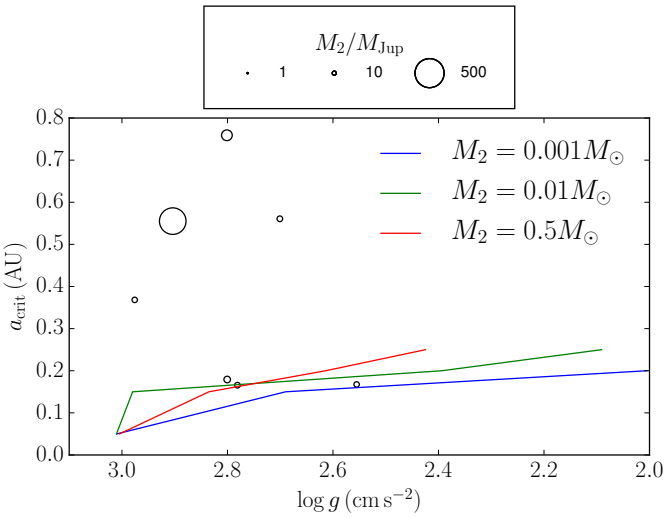

Fig. 4.15.— Same as Figure 4.13 for $M_1 = 3 M_\odot$ with three companion masses $M_2 = 0.001 M_\odot$ (blue), $M_2 = 0.01 M_\odot$ (green) and $M_2 = 0.5 M_\odot$ (red). The black dots are the APOGEE data (Troup et al. 2016), with $M_1 = 2.5$ - $3.5 M_\odot$ and $M_2 = 1$ - $500 M_{\rm Jup}$.

Figure 4.15 shows the $M_1 = 3 M_\odot$ case. Similar to the $2 M_\odot$, $a_{\rm crit} = 0.05$ AU case, dynamical tides are strong and synchronization does not occur. The system separation decreases quickly at $\log g = 3.0$ for the range $M_2 = 0.001$ - $0.5 M_\odot$. At $a_{\rm crit} = 0.2$ AU for the $M_2 = 0.5 M_\odot$ secondary, the distance of 0.2 AU is far away for the high mass companion to synchronize the orbit, which makes the system survive shorter compared with using a $M_2 = 0.01 M_\odot$ or $M_2 = 0.001 M_\odot$ secondary. Similarly, the observed systems are shown in black circles. In this case there are three observed

binaries near the $a = a_{\rm crit}$ lines, that may be undergoing more rapid orbital decay. Wide orbits with with $a_{\rm obs} > 0.8$ AU are not shown in Figure 4.13 to 4.14.

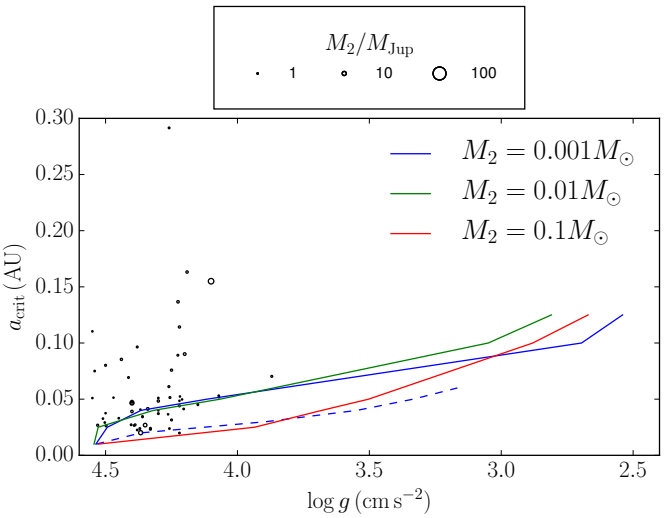

Fig. 4.16.— Same as Figure 4.13 for $M_1 = 1 M_\odot$ with three companion masses $M_2 = 0.001 M_\odot$ (blue), $M_2 = 0.01 M_\odot$ (green) and $M_2 = 0.5 M_\odot$ (red). The blue dashed line is for $a_{\rm crit}$ turning on the equilibrium tides only with Zahn's description. The black dots are the data from exoplanets.org, with $M_1 = 1.0$ - $1.3 M_\odot$ and $M_2 = 1$ - $13 M_{\rm Jup}$.

The calculations of $a_{\rm crit}$ are also compared to binaries containing an exoplanet and host star from Han et al. (2014) (downloaded from exoplanets.org). Figure 4.16 shows stars in the mass range $M_1 = 1 - 1.3\,M_\odot$ with planetary mass companions. These stars are in the MS or early SGB. [3]

Contrary to the APOGEE data in Figure 4.13, a significant number of these star-planet binaries are found with $a < a_{\rm crit}$ in the exoplanet host sample in Figure 4.16. If correct, this result would imply that a large number of binaries have orbital decay times short compared to their age, and are being observed in a short-live phase just

[3]The reason why the upper limit is set at $1.3 M_\odot$ is because stars with $M > 1.3 M_\odot$ have a convective core and thin convective envelope, hence both the dynamical and equilibrium tide dissipation rates are expected to be smaller by comparison, giving small $a_{\rm crit}$ during the MS stage.

before merger. Moreover, the tail of the semi-major axis distribution at $a < a_{\rm crit}$ should be accompanied by a much larger number $\propto \dot{a}^{-1} \propto a^{9.5}$ at larger separation, where $\beta = 9.5$ for dynamical tides. Hence the ~ 10 systems at $a/a_{\rm crit} \sim 0.5$ should be accompanied by $\sim 10 \times 2^{9.5} \simeq 7000$ systems at $a > a_{\rm crit}$. Such a large reservoir of systems at $a > a_{\rm crit}$ is not present in the sample, and it is difficult to imagine that observational bias would cause such a severe lack of systems at only slightly larger orbital separation.

A second explanation for the $a < a_{\rm crit}$ systems in Figure 4.16 would be a suppression of the dynamical tide on the MS. A factor of 2 increase in $a_{\rm crit}$ implies a large $\sim 10^2$ decrease in dissipation rate, since $L_{\rm dyn} \propto a^{-23/3}$. The blue dashed line in Figure 4.16 shows $a_{\rm crit}$ including only the equilibrium tide, with Zahn's reduced viscosity, and ignoring the dynamical tide. Most of the observed systems have $a > a_{\rm crit}$ compared to the equilibrium tide line.

The question is then why the dynamical tide should be strongly suppressed on the MS. While many of the systems have mass near the $k_r \xi_r \simeq 1$ wave breaking limit, a number of them are comfortably above the wave breaking limit, and a traveling wave should be expected. It is unclear why the wave luminosity should be suppressed by $\sim 10^2$ for stars with thick surface convection zones on the MS.

A third explanation could be that these systems with $a < a_{\rm crit}$ have a convective core during the MS, so that the wave reflects and the dynamical tide dissipation is suppressed. The convective core size of MS stars increases as the mass increases. If the stellar mass estimated by observations underestimates the true mass, then some of the systems with $a < a_{\rm crit}$ have been compared to a calculation for a radiative core, when they should have been compared to the calculation for a convective core. Once the dynamical tide turns off, $a_{\rm crit}$ is set by the equilibrium tide, which is in better

agreement with the data. Given that the error bars on stellar mass are in the range of ~ 0.1 to $0.2 M_{\odot}$, it may be difficult to determine if the star has a convective core from the present observations. Figure 4.17 shows $a_{\rm crit}$ is very sensitive to M_1 during the MS phase for stars in range from $M_1 = 1.0 M_{\odot}$ to $1.5 M_{\odot}$. When the dynamical tides turn on, the slope of $a_{\rm crit}$ increases. This is especially more obvious for the $a_{\rm crit}$ lines of $M_1 = 1.1 M_{\odot}$ (black, $a_{\rm crit}$=0.02 - 0.03 AU) and $M_1 = 1.2 M_{\odot}$ (magenta, $a_{\rm crit}$=0.03 - 0.04 AU). For the case of $M_1 = 1.1 M_{\odot}$, the dynamical tides are suppressed at the early MS because of the convective envelope. Then the convective core ceases and lately, the nonlinearity reaches 1, then the dynamical tides turn on. For the case of $M_1 = 1.2 M_{\odot}$ - $1.5 M_{\odot}$, the convective core exists for a longer time during the MS. When it ceases and almost the same time, $k_r \xi_r$ is close to 1 and the dynamical tides become effective. The reason of the increase in $k_r \xi_r$ is that the density near the star center increases and the inner turning point of the wave moves inwardly as composition gradient also increase during the evolution. This result agrees with Barker & Ogilvie (2010). Therefore, the uncertainty in confirming the mass or log g of the primary star may explain why there are many exoplanet systems are below $a_{\rm crit}$ line.

Lastly, another consideration may be important for systems with $a < a_{\rm crit}$ detected by the radial velocity method. In this case we have used the minimum mass, $M_2 \sin(i)$ as the true mass M_2 in our calculations, where i is the orbit inclination. For systems in which the primary spin is not synchronized, increasing M_2 implies larger $a_{\rm crit}$, and a worse agreement between theory and observation. However for sufficiently large M_2 that the primary spin synchronizes, the rate of orbital decay and $a_{\rm crit}$ are much smaller. In practice, among the systems with $a < a_{\rm crit}$, there are only two systems detected by the radial velocity method, for which $\sin(i)$ is not known. For these two

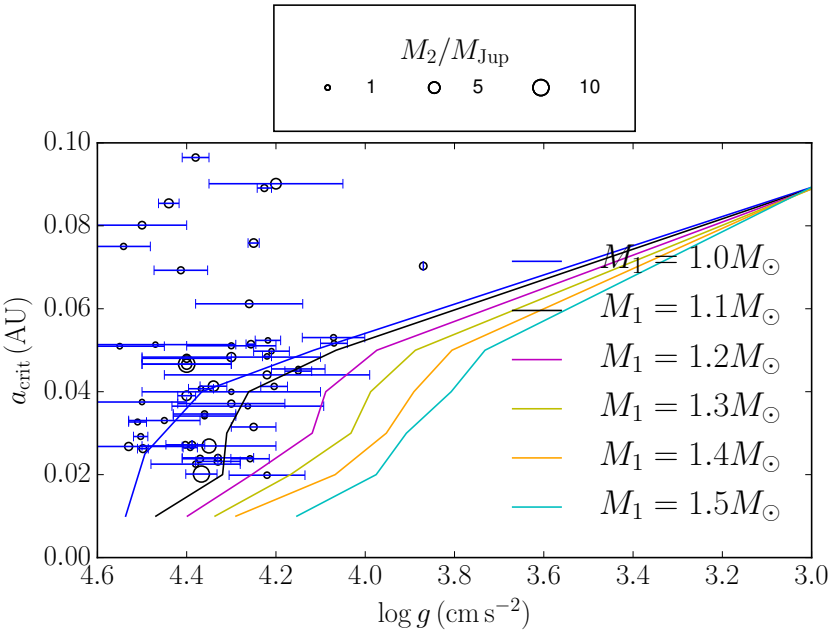

Fig. 4.17.— Critical semi-major axis $a_{\rm crit}$ versus $\log g$ for different $M_1 = 1.0M_\odot$ (blue), $1.1M_\odot$ (black), $1.2M_\odot$ (magenta), $1.3M_\odot$ (yellow), $1.4M_\odot$ (orange), $1.5M_\odot$ (cyan). The data is in open circle with error bars of $\log g$ in blue.

systems, if $\sin(i)$ is sufficiently small and M_2 sufficiently large so that the primary synchronizes, this may help explain the $a < a_{\rm crit}$ systems, since the theory line $a_{\rm crit}$ has used too small a value of M_2. In practice systems with $\sin(i) \ll 1$ are rare. Furthermore, most of the $a < a_{\rm crit}$ systems were detected by the transit method, for which $\sin(i) \simeq 1$.

For binaries with high mass companions, the spin of the primary star will synchronize to the orbit, and orbital decay then proceeds on the stellar evolution timescale. This long phase of evolution ends when

$$a \leq a_D \simeq 6\,R_1 \left(\frac{I_1}{0.12\,M_1 R_1^2}\right)^{1/2} \left(\frac{0.01\,M_1}{M_2}\right)^{1/2}, \tag{4.20}$$

as the orbital decay will accelerate and the rotation rate of the primary will no

longer be synchronized. An analytic calculation of $a_{\rm crit}$ in the synchronized case is complicated. The use of $a_{\rm D}$ as $a_{\rm crit}$ is not a good approximation as typically there has been orbital decay before the instability is reached, and also because there some further expansion of the primary after $a = a_{\rm D}$. Our numerical results show that $a_{\rm D}$ is typically smaller than $a_{\rm crit}$ by a factor of ~ 2.

Next, analytic scalings for $a_{\rm crit}$ are derived for the equilibrium tide, assuming $\Omega \ll n$ and $M_2 \ll M_1$. Plugging the viscous heating rate into Equation 4.1 gives the orbital decay rate for each viscosity formula to be

$$\dot{a}_{\rm STD} = -9.65 \times 10^{-7}\,{\rm cm\,s^{-1}} \left(\frac{M_2}{M_1}\right)\left(\frac{R_1}{R_\odot}\right)^{7.93}\left(\frac{a}{0.1{\rm AU}}\right)^{-7}, \tag{4.21}$$

$$\dot{a}_{\rm Z} = -4.57 \times 10^{-7}\,{\rm cm\,s^{-1}} \left(\frac{M_1}{M_\odot}\right)^{-2}\left(\frac{M_2}{M_\odot}\right)\left(\frac{R_1}{R_\odot}\right)^{7.74}\left(\frac{a}{0.1{\rm AU}}\right)^{-11/2}, \tag{4.22}$$

and

$$\dot{a}_{\rm GN} = -2.7 \times 10^{-8}\,{\rm cm\,s^{-1}} \left(\frac{M_1}{M_\odot}\right)^{-3}\left(\frac{M_2}{M_\odot}\right)\left(\frac{R_1}{R_\odot}\right)^{7.56}\left(\frac{a}{0.1{\rm AU}}\right)^{-4}. \tag{4.23}$$

Each formula has the form $\dot{a} = -f(t)a^{-\beta}$ where the time-dependence has been parametrized in terms of stellar radius here. The critical semi-major axis for which the orbit can decay to $a = 0$ in a time t is

$$a_{\rm crit}(t) = [(\beta+1)\tau(t)]^{1/(\beta+1)} \tag{4.24}$$

where

$$\tau(t) = \int_0^t dt' f(t') \tag{4.25}$$

is a new time coordinate with the units (length)$^{\beta+1}$.

The time integral may be simply performed for RGB stars (Verbunt & Phinney 1995). Since the radius and shell-burning luminosity mainly depend on the helium core mass, $M_{\rm He,1}$, a change of variables from t to R_1 may be found using

$$\dot{R}_1 = \frac{dR_1}{dM_{\rm He,1}} \frac{dM_{\rm He,1}}{dt} \simeq \left(\frac{R_\odot}{3.7\,{\rm Gyr}}\right) \left(\frac{R_1}{R_\odot}\right)^{2.3}. \tag{4.26}$$

The time integrals can then be written

$$\tau(t) \simeq 3.7\,{\rm Gyr} \int_0^{R_1/R_\odot} dx f(t) x^{-2.3}, \tag{4.27}$$

where $x = R_1/R_\odot$. Since $f(t)$ has been expressed as a power of R_1, the integrals can be directly evaluated, and are dominated by the largest x. The results for each viscosity formula are then

$$a_{\rm crit,STD}(t) \simeq 0.37\,{\rm AU} \left(\frac{M_2}{0.1\,M_1}\right)^{1/8} \left(\frac{R_1}{10\,R_\odot}\right)^{0.83} \tag{4.28}$$

$$a_{\rm crit,Z}(t) \simeq 0.41\,{\rm AU} \left(\frac{M_\odot}{M_1}\right)^{4/13} \left(\frac{M_2}{0.1\,M_\odot}\right)^{2/13} \left(\frac{R_1}{10\,R_\odot}\right)^{0.99} \tag{4.29}$$

$$a_{\rm crit,GN}(t) \simeq 0.35\,{\rm AU} \left(\frac{M_\odot}{M_1}\right)^{3/5} \left(\frac{M_2}{0.1\,M_\odot}\right)^{1/5} \left(\frac{R_1}{10\,R_\odot}\right)^{1.25} \tag{4.30}$$

while each expression has a similar value for these fiducial parameters, their scalings with M_1, M_2 and R_1 differ. As $M_2 \ll M_1$, $\xi_{r,\ell m} \sim \xi_{h,\ell m}$ and $\Omega \ll n$ are assumed,

there is a disagreement between the factors before the scalings from Equation 4.21 to 4.30 and the numerical result. The factors in Equation 4.29 are 0.28, 0.26 and 0.25 AU for $M_1 = 1$, 2 and $3M_\odot$, respectively. The main purpose of showing these equations is to find how $a_{\rm crit}$ scales with M_1, M_2 and R_1.

The critical semi-major axis for reduced viscosity is only relevant if $\tau_{\rm ed} \gtrsim P_f$ at the critical radius. Plugging Equation 4.29 into Equation 4.45 shows that the Zahn prescription applies for

$$R_1 \leq 5.1\, R_\odot \left(\frac{0.1\, M_\odot}{M_2}\right)^{0.18} \left(\frac{M_1}{M_\odot}\right)^{1.31} \quad \text{(Zahn)}, \tag{4.31}$$

$$R_1 \leq 10\, R_\odot \left(\frac{0.1\, M_\odot}{M_2}\right)^{0.26} \left(\frac{M_1}{M_\odot}\right)^{1.1} \quad \text{(GN)}. \tag{4.32}$$

So if a particular system has $a \lesssim a_{\rm crit}(t)$ during the time when R_1 is less than these critical values, then reduced viscosity should be used rather than standard viscosity. Further up the giant branch the standard viscosity would apply.

Next an approximate expression is derived for $a_{\rm crit}$ for the dynamical tide. In Section 4.3 it was found that at fixed semi-major axis, $L_{\rm dyn}$ increased strongly on the SGB and was nearly constant on the RGB. The numerical results for the RGB can be fit with the form

$$L_{\rm dyn} = C_{L,{\rm dyn}} \left(\frac{M_1 + M_2}{M_\odot}\right)^{11/6} \left(\frac{M_2}{M_\odot}\right)^{2} \left(\frac{a}{0.1{\rm AU}}\right)^{-23/2} \tag{4.33}$$

where $C_{L,{\rm dyn}} = 3.51 \times 10^{30}, 7.02 \times 10^{31}$, and $3.36 \times 10^{35} {\rm erg\,s^{-1}}$ for $M_1 = 1,\ 2$ and $3M_\odot$, respectively. Plugging Equation 4.33 into Equation 4.1, and using Equation 4.26 to

convert age to stellar radius gives the final result

$$a_{\rm crit} = C_{a_{\rm crit},{\rm dyn}} \left(\frac{M_1+M_2}{M_\odot}\right)^{11/63} \left(\frac{M_2}{M_1}\right)^{2/21} \left[\left(\frac{R_{\rm brgb}}{R_\odot}\right)^{-1.3} - \left(\frac{R_1}{R_\odot}\right)^{-1.3}\right]^{2/21} \quad (4.34)$$

the coefficient has the value $C_{a_{\rm crit}} = 0.14$, 0.19 and 0.42 AU for $M_1 = 1,\ 2$ and $3 M_\odot$, respectively. Unlike the equilibrium tide, the integral over time is dominated by the base of the RGB for the dynamical tide, and a lower limit $R_{\rm brgb}$ has been assumed for the radius there. Hence $a_{\rm crit}$ asymptotes to a constant as R_1 grows, allowing the equilibrium tide to dominate for wide orbits. Similar to the scaling functions for the equilibrium tide, Equation 4.33 and 4.34 is qualitatively right with the scalings of M_1, M_2 and R_1, but they are not in a good agreement with the numerical result for the entire SGB and RGB phase. Because the wave luminosity is not a constant in SGB phase, and the equilibrium tide is the main mechanism for orbital shrinking in RGB phase.

All the results presented in Section 4.4 used sufficiently large M_2 that $k_r \xi_r > 1$ in the core, giving rise to traveling waves. The dynamical tide due to smaller, planetary mass companions may still generate the traveling wave limit of the dynamical tide if $P_{\rm orb} > P_{\rm orb,diff}$ and radiative diffusion damping is strong. However, if M_2 is too small, the orbit will not decay, but rather the star will expand out to meet the planet. The lower limit to M_2 that has $a_{\rm crit} > R_1$ may be estimated from Equation 4.34. For $M_1 = 1\,M_\odot$, in the limit $R_1 \gtrsim R_{\rm brgb}$, for simplicity, the result is

$$M_{2,\rm min} \simeq 3\,M_\oplus \left(\frac{R_1}{10\,R_\odot}\right)^{21/2} \left(\frac{R_{\rm brgb}}{5\,R_\odot}\right)^{1.3}. \quad (4.35)$$

Hence there is a small parameter space for sub-Jupiter-sized planets to have a modest

amount of orbital decay prior to the merger.

4.6 Conclusion

Motivated by current and future surveys that find binaries with SGB or RGB primaries and stellar or substellar secondaries, MESA models for primary stars of mass $M_1 = 1, 2$ and $3\,M_\odot$ have been used to compute dynamical and equilibrium tidal dissipation rates. The resultant orbital decay rate was used to compare merger times for different primary and secondary masses and orbital separations, as well as different prescriptions for turbulent viscosity. The role of synchronization of the primary's spin and the Darwin instability have been taken into account.

Analytic formulae have been derived for the equilibrium tide dissipation rate for each prescription of turbulent viscosity, by approximating the convection zone as an $n = 3/2$ polytrope. These formulae are used to derive the critical separation ($a_{\rm crit}$) out to which non-synchronized binaries will have merged by some time or $\log g$ of the primary.

The dynamical tide dominates for close-in systems, with less evolved primaries. The equilibrium tide dominates for wider systems and more evolved primaries. The dividing line between the two depends on primary and secondary masses, as well as the prescription for reduced viscosity.

The tidal evolution depends sensitively on the primary star's mass. For stars of mass $M_1 \gtrsim 1.3\,M_\odot$, equilibrium and dynamical tidal friction is strongly suppressed on the MS, and turns on suddenly during the sub-giant branch phase as the convective envelope deepens. For close-in systems this may result in orbital decay that proceeds rapidly compared to the stellar evolutionary timescale. The reason why the equilibrium tide is suppressed at the MS stage is because the energy dissipation rate

depends on the convective envelope mass and the eddy velocity. These two physical quantities are much larger in the RGB phase. In the MS phase, the dynamical tide is suppressed because the wave can't propagate inward, and the convective envelope for $M_1 \gtrsim 1.3\,M_\odot$ is very thin.

For $M_2 = 1$ - $10\,M_{\rm Jup}$, the low mass secondary cannot provide enough angular momentum to synchronize the spin. For synchronization to occur, M_2 must be on the order of $0.1 M_\odot$. After it reaches the Darwin instability, the system merges soon after. Neither small ($M_2 \lesssim 10 M_{\rm Jup}$) nor large ($M_2 \gtrsim 100 M_{\rm Jup}$) companions can give rise to fast orbital decay. Small mass companions exert weak tidal forces, thereby causing low energy dissipation rates. High mass companions synchronize their orbits quickly, resulting in a small forcing frequency and consequently low energy dissipation rate. Only intermediate mass ($10 \lesssim M_2 \lesssim 100 M_{\rm Jup}$) secondaries can sustain a large energy dissipation rate.

By accounting for the Darwin instability, dynamical tide, and Zahn's prescription for the reduced viscosity in the equilibrium tide, we define a critical separation $a_{\rm crit}$ below which the system merges rapidly. We find that the majority of APOGEE binaries show separations larger than $a_{\rm crit}$ for the observed $\log g$, indicating that these systems are tidally stable. A handful of systems have observed separations $a < a_{\rm crit}$, implying rapid orbital decay. For the data from exoplanet MS host stars, we find that 19 of observed systems with $M_1 < 1.3 M_\odot$ have $a < a_{\rm crit}$. This implies that the dynamical tide may be suppressed in the MS stage for some stars with a radiative core.

Schlaufman & Winn (2013) discussed observational evidence that SGBs with planetary-mass companions show a strong deficit of systems with $a \lesssim 0.67\,{\rm AU}$ ($P_{\rm orb} =$ 200 days). Further, the closest systems at 0.67 AU had fairly circular orbits. They

proposed a scenario to explain this with tides, in which tidal friction is weak on the MS but increases dramatically on the sub-giant branch. Their scenario requires $R_1 \sim 3$ - $4\,R_\odot$ primary stars to cause orbital decay out to 0.67 AU, and circularization of the orbits just outside this. Our results show that, with the tidal friction mechanisms included here, that orbital decay rate can only affect systems out to $a = 0.05$ - 0.15 AU for this range of radii (and depending on the stellar mass), and that tidal friction is many orders of magnitude too weak to affect systems at $a = 0.67$ AU.

4.7 Appendix A Analytic Estimate of the Heating Rate

Analytic estimates for the dissipation rate can be derived by treating the convective envelope as an $n = 3/2$ polytrope with interior mass $m(r) \simeq M_1$. The latter assumption greatly simplifies the formulae for the density profile, however it leads to factor of a few errors for standard viscosity since the dissipation occurs sufficiently deep in the convection zone that the interior mass $m(r)$ is changing rapidly there (see the middle panel of Figure 4.1). The approximation is better for linear and quadratic scalings, as their main contribution is closer to the surface.

For $\ell = 2$, the dissipation integral can be simplified to

$$\dot{E} \simeq \frac{2016\pi}{5}(n-\Omega)^2 R_1^2 \left(\frac{M_2}{M_1}\right)^2 \left(\frac{R_1}{a}\right)^6 \int_{r_{\rm bcz}}^{R_1} dr \rho\nu \left(\frac{r}{R_1}\right)^8 . \tag{4.36}$$

MESA models of a $M_1 = 1.5\,M_\odot$ RGB envelope gives a polytropic constant, $K =$

$P/\rho^{5/3}$, strongly dependent on the evolutionary phase as

$$K \simeq 3.98 \times 10^{14}\,\mathrm{cm^4\,g^{-2/3}\,s^{-2}} \left(\frac{R_1}{R_\odot}\right)^{0.94}. \tag{4.37}$$

Integrating the equation of hydrostatic balance then gives the density profile

$$\rho(r) \simeq 2.65\,\mathrm{g\,cm^{-3}} \left(\frac{M_1}{M_\odot}\right)^{3/2} \left(\frac{R_\odot}{R_1}\right)^{2.9} \left(\frac{R_1 - r}{r}\right)^{3/2}. \tag{4.38}$$

The pressure scale height is

$$H = \frac{P}{\rho g} = \frac{2}{5}\frac{r(R_1 - r)}{R_1} \tag{4.39}$$

which has a peak of $H = R_1/10$ at $r = R_1/2$. Verbunt & Phinney (1995) found the luminosity-radius relation is roughly $L_1/L_\odot \simeq (R_1/R_\odot)^{1.6}$. The mixing length velocity $v_{\rm ed} \simeq (L_1/4\pi r^2\rho)^{1/3}$ can then be used to give the "standard" (non-reduced) viscosity

$$\nu_{\rm std} = \frac{1}{3} v_{\rm ed}\alpha_{\rm mlt} H \simeq 5.34 \times 10^{13}\,\mathrm{cm^2\,s^{-1}} \left(\frac{M_\odot}{M_1}\right)^{1/2} \left(\frac{R_1}{R_\odot}\right)^{1.83} \left(\frac{r}{R}\right)^{5/6} \left(\frac{R_1 - r}{R_1}\right)^{1/2} \tag{4.40}$$

which has a maximum inside the convection zone. The eddy turnover time is

$$\tau_{\rm ed} = \frac{\alpha_{\rm mlt} H}{v_{\rm ed}} \simeq 346\,\mathrm{days} \left(\frac{M_1}{M_\odot}\right)^{1/2} \left(\frac{R_1}{10R_\odot}\right)^{0.17} \left(\frac{r}{R_1}\right)^{7/6} \left(\frac{R_1 - r}{R_1}\right)^{3/2}, \tag{4.41}$$

with peak value longer than the orbital periods of many APOGEE binaries with $P_f = P_{\rm orb}/2 \sim$ days $-$ weeks.

Given the run over these quantities with radius, the integrals for each viscosity model can now be performed. For standard viscosity the dissipation rate is

$$\dot{E}_{\rm std} = 5.66 \times 10^{28}\,{\rm erg\ s^{-1}}\ \ (1-\Omega/n)^2 \left(\frac{M_\odot}{M_1}\right)\left(\frac{M_2}{M_\odot}\right)^2\left(\frac{R_1}{R_\odot}\right)^{7.9}\left(\frac{0.1\,{\rm AU}}{a}\right)^9, \quad (4.42)$$

by comparison, the dissipation rate for the "Zahn" (linear in P_f) turbulent viscosity is

$$\frac{\dot{E}_{\rm Z}}{\dot{E}_{\rm std}} = 0.47\,\left(\frac{a}{0.1\,{\rm AU}}\right)^{3/2}\left(\frac{M_1}{M_\odot}\right)^{3/2}\left(\frac{M_1+M_2}{M_\odot}\right)^{1/2}\left(\frac{R_\odot}{R_1}\right)^{0.19}\left(1-\frac{\Omega}{n}\right)^{-1}, \quad (4.43)$$

and the GN (quadratic in P_f) rate is

$$\frac{\dot{E}_{\rm GN}}{\dot{E}_{\rm std}} = 0.027\,\ln\Lambda\left(\frac{a}{0.1\,{\rm AU}}\right)^3\left(\frac{M_1}{M_\odot}\right)\left(\frac{R_\odot}{R_1}\right)^{0.34}\left(1-\frac{\Omega}{n}\right)^{-2}. \quad (4.44)$$

Here $\ln\Lambda \equiv \int_{P_{\rm min}}^{P_{\rm max}} d\ln P \simeq$ a few represents the flat integrand observed for the GN curve in Figure 4.1.

The Zahn and GN scalings are shallower with orbital separation and stellar radius, and have a different dependence on forcing frequency. For nearly synchronous rotation, the forcing frequency $2(n-\Omega)$ becomes small, and standard viscosity is appropriate.

Equations 4.43 and 4.44 can be set to unity and solved for the critical semi-major axis inside of which reduced viscosity operates. Zahn's prescription holds for

$$a \le 0.17\,{\rm AU}\left(\frac{M_\odot}{M_1}\right)\left(\frac{M_\odot}{M_1+M_2}\right)^{1/3}\left(\frac{R_1}{R_\odot}\right)^{0.11}\left(1-\frac{\Omega}{n}\right)^{2/3} \quad (4.45)$$

and a similar expression holds for the GN prescription, with a slightly different numerical coefficient reflecting the coefficients $1/2$ and $1/(2\pi)^2$ in two prescriptions.

Chapter 5

Summary

This thesis focuses on the areas of stellar and binary evolution, as well as oscillations and tidal friction in binaries. The following chapter summarizes the work on three projects that cover different topics, ranging from white dwarfs to evolved stars to exoplanets.

In Chapter 2, we investigated if the observed population of pulsating ELM WDs could be formed through the "magnetic braking" model, which has previously been used to explain Cataclysmic Variables and AM CVN binaries. I performed an extensive parameter study (of donor and accretor masses and initial orbital periods) and compared the resulting evolutionary models to the observations of $\log g$, $T_{\rm eff}$ and orbital period $P_{\rm orb}$. We used the MESA code to perform the binary evolution calculations via the non-conservative stable mass transfer channel (the total mass and angular momentum for the system is not conserved). We also explore the CE and conservative mass transfer formation channels.

My Roche-lobe overflow models make detailed predictions for the size of the hydrogen-rich envelope relative to the helium core (see Figure 2.20). Since the size of the envelope can be a large fraction of the total stellar radius, the g-mode periods are

quite sensitive to the envelope size. After the mass transfer phase, the orbit of the resulting WD binary continues to shrink because of the gravitational wave emission (if $P_{\rm orb} <\sim 1$ hour), ultimately leading to the merger of the double degenerate stars.

In close binary system, aside from the gravitational wave and magnetic braking loss, tidal friction may also play an important role in changing the orbital parameters. In Chapter 4, we computed the equilibrium tidal dissipation rate from first principles, for MESA models of RGB stars as a function of age. A crucial consideration is the prescription for "reduced viscosity" (Zahn 1989; Goldreich & Nicholson 1977), which occurs when the energy-bearing eddies turn over slower than the tidal forcing timescale, as this is the norm for the APOGEE sample.

No survey of dynamical tidal wave luminosity has been carried out over a broad range of stellar masses and evolutionary stages. The amplitude of dynamical tide forcing is a crucial, but poorly-understood effect. Therefore we study dynamical tide excitation over the stellar mass range $M = 1.0 - 3.0\,M_{\odot}$, of interest to current surveys. Our calculations find that the dynamical tide dominates for close separations ($\dot{E}_{\rm dyn} \sim P_{\rm orb}^{-7.67} - P_{\rm orb}^{-10}$) in subgiant phase stars and that the equilibrium tide dominates for wide separations ($\dot{E}_{\rm eq} \sim P_{\rm orb}^{-4} - P_{\rm orb}^{-6}$) in middle- and late-stage RGB stars.

The content in Chapter 3 is the application of our dynamical tides calculation onto a specific system, WASP-12. We show that if the WASP-12 is on the main sequence, known tidal friction mechanisms are too inefficient to explain the observed $\dot{P}$. However, once core nuclear burning ends and the core becomes radiative, gravity waves launched at the radiative-convective boundary may travel inward and "break" nonlinearly, depositing their energy and angular momentum. This implies a vast increase in the tidal dissipation rate compared to the main sequence value, and the orbit of a Gyrs old planet may find itself with only Myrs left to live. The inward

luminosity of gravity waves excited at the radiative-convective boundary. I used a numerical approach in which an inward-going traveling wave boundary condition was applied in the radiative zone. The numerical method makes fewer assumptions than previous calculation methods, enabling efficient calculation of the wave luminosity for different stellar structures.

References

Abbott, B. P., Abbott, R., Abbott, T. D., et al. 2016, Physical Review Letters, 116, 061102

Aerts, C., Christensen-Dalsgaard, J., & Kurtz, D. W. 2010, Asteroseismology

Alam, S., Albareti, F. D., Allende Prieto, C., et al. 2015, ApJS, 219, 12

Albrecht, S., Winn, J. N., Johnson, J. A., et al. 2012, ApJ, 757, 18

Applegate, J. H. 1992, ApJ, 385, 621

Arras, P., & Socrates, A. 2010, ApJ, 714, 1

Asplund, M., Grevesse, N., Sauval, A. J., & Scott, P. 2009, ARA&A, 47, 481

Barker, A. J. 2011, MNRAS, 414, 1365

Barker, A. J., & Ogilvie, G. I. 2010, MNRAS, 404, 1849

Bell, K. J., Kepler, S. O., Montgomery, M. H., et al. 2015, in Astronomical Society of the Pacific Conference Series, Vol. 493, 19th European Workshop on White Dwarfs, ed. P. Dufour, P. Bergeron, & G. Fontaine, 217

Bensby, T., Feltzing, S., & Oey, M. S. 2014, A&A, 562, A71

Birkby, J. L., Cappetta, M., Cruz, P., et al. 2014, MNRAS, 440, 1470

Bogomazov, A. I., & Tutukov, A. V. 2009, Astronomy Reports, 53, 214

Bolmont, E., & Mathis, S. 2016, Celestial Mechanics and Dynamical Astronomy, 126, 275

Boothroyd, A. I., & -Juliana Sackmann, I. 1995, ArXiv Astrophysics e-prints, astro-ph/9512121

Brown, W. R., Gianninas, A., Kilic, M., Kenyon, S. J., & Allende Prieto, C. 2016, ApJ, 818, 155

Brown, W. R., Kilic, M., Allende Prieto, C., Gianninas, A., & Kenyon, S. J. 2013, ApJ, 769, 66

Brown, W. R., Kilic, M., Allende Prieto, C., & Kenyon, S. J. 2010, ApJ, 723, 1072

—. 2012, ApJ, 744, 142

Browning, M. K. 2008, ApJ, 676, 1262

Burkart, J., Quataert, E., & Arras, P. 2014, MNRAS, 443, 2957

Burkart, J., Quataert, E., Arras, P., & Weinberg, N. N. 2013, MNRAS, 433, 332

Chan, T., Ingemyr, M., Winn, J. N., et al. 2011, AJ, 141, 179

Chen, X., Maxted, P. F. L., Li, J., & Han, Z. 2017, MNRAS, 467, 1874

Chernov, S. V., Ivanov, P. B., & Papaloizou, J. C. B. 2017, MNRAS, 470, 2054

Chernov, S. V., Papaloizou, J. C. B., & Ivanov, P. B. 2013, MNRAS, 434, 1079

Choi, J., Dotter, A., Conroy, C., et al. 2016, ApJ, 823, 102

Córsico, A. H., & Althaus, L. G. 2014, A&A, 569, A106

Córsico, A. H., Althaus, L. G., Serenelli, A. M., et al. 2016, A&A, 588, A74

Courant, R., & Hilbert, D. 1953, Methods of mathematical physics - Vol.1; Vol.2

Cowling, T. G. 1941, MNRAS, 101, 367

Damiani, C., & Lanza, A. F. 2015, A&A, 574, A39

Darwin, G. H. 1879, The Observatory, 3, 79

D'Cruz, N. L., Dorman, B., Rood, R. T., & O'Connell, R. W. 1996, ApJ, 466, 359

Deheuvels, S., Brandão, I., Silva Aguirre, V., et al. 2016, A&A, 589, A93

Driebe, T., Blöcker, T., Schönberner, D., & Herwig, F. 1999, A&A, 350, 89

Dziembowski, W. 1977, , 27, 95

Eggleton, P. P. 1983, ApJ, 268, 368

Enoch, B., Collier Cameron, A., Parley, N. R., & Hebb, L. 2010, A&A, 516, A33

Essick, R., & Weinberg, N. N. 2016, ApJ, 816, 18

Evans, C. R., Iben, Jr., I., & Smarr, L. 1987, ApJ, 323, 129

Fossati, L., Bagnulo, S., Elmasli, A., et al. 2010, ApJ, 720, 872

Fryer, C. L. 1999, ApJ, 522, 413

Fuller, J., Hambleton, K., Shporer, A., Isaacson, H., & Thompson, S. 2017, MNRAS, 472, L25

Fuller, J., & Lai, D. 2012, MNRAS, 420, 3126

Fuller, J., Luan, J., & Quataert, E. 2016, MNRAS, 458, 3867

Gallet, F., Bolmont, E., Mathis, S., Charbonnel, C., & Amard, L. 2017, A&A, 604, A112

Gianninas, A., Kilic, M., Brown, W. R., Canton, P., & Kenyon, S. J. 2015, ApJ, 812, 167

Goldreich, P., & Keeley, D. A. 1977, ApJ, 211, 934

Goldreich, P., & Nicholson, P. D. 1977, Icarus, 30, 301

—. 1989, ApJ, 342, 1079

Goldreich, P., & Soter, S. 1966, Icarus, 5, 375

Goodman, J., & Dickson, E. S. 1998, ApJ, 507, 938

Goodman, J., & Oh, S. P. 1997, ApJ, 486, 403

Grether, D., & Lineweaver, C. H. 2006, ApJ, 640, 1051

Han, E., Wang, S. X., Wright, J. T., et al. 2014, PASP, 126, 827

Han, Z., Tout, C. A., & Eggleton, P. P. 2000, MNRAS, 319, 215

Hansen, B. M. S. 2010, ApJ, 723, 285

Hansen, C. J., & Kawaler, S. D. 1994, Stellar Interiors. Physical Principles, Structure, and Evolution., 84, doi:10.1007/978-1-4419-9110-2

Hebb, L., Collier-Cameron, A., Loeillet, B., et al. 2009, ApJ, 693, 1920

Hermes, J. J., Montgomery, M. H., Winget, D. E., et al. 2012, ApJ, 750, L28

Hermes, J. J., Montgomery, M. H., Gianninas, A., et al. 2013a, MNRAS, 436, 3573

Hermes, J. J., Montgomery, M. H., Winget, D. E., et al. 2013b, ApJ, 765, 102

Hjellming, M. S., & Webbink, R. F. 1987, ApJ, 318, 794

Huber, D., Chaplin, W. J., Christensen-Dalsgaard, J., et al. 2013, ApJ, 767, 127

Husnoo, N., Pont, F., Mazeh, T., et al. 2012, MNRAS, 422, 3151

Hut, P. 1981, A&A, 99, 126

Iben, Jr., I., & Tutukov, A. V. 1984, ApJS, 54, 335

Istrate, A. G., Marchant, P., Tauris, T. M., et al. 2016, A&A, 595, A35

Ivanov, P. B., Papaloizou, J. C. B., & Chernov, S. V. 2013, MNRAS, 432, 2339

Jackson, B., Barnes, R., & Greenberg, R. 2009, ApJ, 698, 1357

Jackson, B., Greenberg, R., & Barnes, R. 2008, ApJ, 678, 1396

Kilic, M., Brown, W. R., Allende Prieto, C., et al. 2011, ApJ, 727, 3

—. 2012, ApJ, 751, 141

Kilic, M., Hermes, J. J., Gianninas, A., & Brown, W. R. 2015, MNRAS, 446, L26

Kippenhahn, R., Kohl, K., & Weigert, A. 1967, ZAp, 66, 58

Kippenhahn, R., & Weigert, A. 1990, Stellar Structure and Evolution, 192

Koester, D., Voss, B., Napiwotzki, R., et al. 2009, A&A, 505, 441

Kraft, R. P. 1967, ApJ, 150, 551

Kumar, P., & Goodman, J. 1996, ApJ, 466, 946

Kunitomo, M., Ikoma, M., Sato, B., Katsuta, Y., & Ida, S. 2011, ApJ, 737, 66

Kushnir, D., Zaldarriaga, M., Kollmeier, J. A., & Waldman, R. 2017, MNRAS, 467, 2146

Landau, L. D., & Lifshitz, E. M. 1959, Fluid mechanics

—. 1975, The classical theory of fields

Maciejewski, G., Errmann, R., Raetz, S., et al. 2011, A&A, 528, A65

Maciejewski, G., Dimitrov, D., Fernández, M., et al. 2016, A&A, 588, L6

Magic, Z., Weiss, A., & Asplund, M. 2015, A&A, 573, A89

Majewski, S. R., Schiavon, R. P., Frinchaboy, P. M., et al. 2017, AJ, 154, 94

Maxted, P. F. L., Anderson, D. R., Burleigh, M. R., et al. 2011, MNRAS, 418, 1156

Moore, K., & Garaud, P. 2016, ApJ, 817, 54

Moravveji, E., Aerts, C., Pápics, P. I., Triana, S. A., & Vandoren, B. 2015, A&A, 580, A27

Moravveji, E., Townsend, R. H. D., Aerts, C., & Mathis, S. 2016, ApJ, 823, 130

Mustill, A. J., & Villaver, E. 2012, ApJ, 761, 121

Nelemans, G., & Tauris, T. M. 1998, A&A, 335, L85

Nelemans, G., Yungelson, L. R., & Portegies Zwart, S. F. 2004, MNRAS, 349, 181

Nordhaus, J., Spiegel, D. S., Ibgui, L., Goodman, J., & Burrows, A. 2010, MNRAS, 408, 631

Ogilvie, G. I. 2014, ARA&A, 52, 171

Ogilvie, G. I., & Lesur, G. 2012, MNRAS, 422, 1975

Paczynski, B. 1976, in IAU Symposium, Vol. 73, Structure and Evolution of Close Binary Systems, ed. P. Eggleton, S. Mitton, & J. Whelan, 75

Patra, K. C., Winn, J. N., Holman, M. J., et al. 2017, AJ, 154, 4

Paxton, B., Bildsten, L., Dotter, A., et al. 2011, ApJS, 192, 3

Paxton, B., Cantiello, M., Arras, P., et al. 2013, ApJS, 208, 4

Paxton, B., Marchant, P., Schwab, J., et al. 2015, ApJS, 220, 15

Paxton, B., Schwab, J., Bauer, E. B., et al. 2018, ApJS, 234, 34

Penev, K., Barranco, J., & Sasselov, D. 2009, ApJ, 705, 285

—. 2011, ApJ, 734, 118

Penev, K., Jackson, B., Spada, F., & Thom, N. 2012, ApJ, 751, 96

Penev, K., & Sasselov, D. 2011, ApJ, 731, 67

Perlmutter, S., Aldering, G., Goldhaber, G., et al. 1999, ApJ, 517, 565

Phinney, E. S. 1992, Philosophical Transactions of the Royal Society of London Series A, 341, 39

Podsiadlowski, P., Han, Z., & Rappaport, S. 2003, MNRAS, 340, 1214

Podsiadlowski, P., Rappaport, S., & Pfahl, E. D. 2002, ApJ, 565, 1107

Rappaport, S., Verbunt, F., & Joss, P. C. 1983, ApJ, 275, 713

Rasio, F. A., Tout, C. A., Lubow, S. H., & Livio, M. 1996, ApJ, 470, 1187

Refsdal, S., & Weigert, A. 1971, A&A, 13, 367

Riess, A. G., Filippenko, A. V., Challis, P., et al. 1998, AJ, 116, 1009

Ruiter, A. J., Belczynski, K., Benacquista, M., Larson, S. L., & Williams, G. 2010, ApJ, 717, 1006

Salaris, M., & Cassisi, S. 2006, Evolution of Stars and Stellar Populations

Sandage, A., Saha, A., Tammann, G. A., et al. 1996, ApJ, 460, L15

Sandquist, E., Taam, R. E., Lin, D. N. C., & Burkert, A. 1998, ApJ, 506, L65

Schlaufman, K. C. 2010, ApJ, 719, 602

Schlaufman, K. C., & Winn, J. N. 2013, ApJ, 772, 143

Schröder, K.-P., & Connon Smith, R. 2008, MNRAS, 386, 155

Seager, S., & Mallén-Ornelas, G. 2003, ApJ, 585, 1038

Shapiro, S. L., & Teukolsky, S. A. 1983, Black holes, white dwarfs, and neutron stars: The physics of compact objects

Silva Aguirre, V., Ballot, J., Serenelli, A. M., & Weiss, A. 2011, A&A, 529, A63

Skumanich, A. 1972, ApJ, 171, 565

Smedley, S. L., Tout, C. A., Ferrario, L., & Wickramasinghe, D. T. 2017, MNRAS, 464, 237

Smith, M. A. 1979, PASP, 91, 737

Soberman, G. E., Phinney, E. S., & van den Heuvel, E. P. J. 1997, A&A, 327, 620

Spruit, H. C., & Ritter, H. 1983, A&A, 124, 267

Steinfadt, J. D. R., Bildsten, L., & Arras, P. 2010, ApJ, 718, 441

Sun, M., & Arras, P. 2018, ApJ, 858, 14

Tauris, T. M., & van den Heuvel, E. P. J. 2006, Formation and evolution of compact stellar X-ray sources, ed. W. H. G. Lewin & M. van der Klis, 623–665

Teitler, S., & Königl, A. 2014, ApJ, 786, 139

Terquem, C., Papaloizou, J. C. B., Nelson, R. P., & Lin, D. N. C. 1998, ApJ, 502, 788

Torres, G., Fischer, D. A., Sozzetti, A., et al. 2012, ApJ, 757, 161

Tout, C. A., Aarseth, S. J., Pols, O. R., & Eggleton, P. P. 1997, MNRAS, 291, 732

Townsend, R. H. D., & Teitler, S. A. 2013, MNRAS, 435, 3406

Tremblay, P.-E., Gianninas, A., Kilic, M., et al. 2015, ApJ, 809, 148

Troup, N. W., Nidever, D. L., De Lee, N., et al. 2016, AJ, 151, 85

Unno, W., Osaki, Y., Ando, H., Saio, H., & Shibahashi, H. 1989, Nonradial oscillations of stars

van der Sluys, M. V., Verbunt, F., & Pols, O. R. 2006, A&A, 460, 209

Verbunt, F., & Phinney, E. S. 1995, A&A, 296, 709

Villaver, E., Livio, M., Mustill, A. J., & Siess, L. 2014, ApJ, 794, 3

Watson, C. A., & Marsh, T. R. 2010, MNRAS, 405, 2037

Webbink, R. F. 1984, ApJ, 277, 355

Weinberg, N. N., Arras, P., Quataert, E., & Burkart, J. 2012, ApJ, 751, 136

Weinberg, N. N., Sun, M., Arras, P., & Essick, R. 2017, ApJ, 849, L11

Witte, M. G., & Savonije, G. J. 2002, A&A, 386, 222

Woods, T. E., & Ivanova, N. 2011, ApJ, 739, L48

Woods, T. E., Ivanova, N., van der Sluys, M. V., & Chaichenets, S. 2012, ApJ, 744, 12

Zahn, J. P. 1966, Annales d'Astrophysique, 29, 489

Zahn, J.-P. 1975, A&A, 41, 329

—. 1977, A&A, 57, 383

—. 1989, A&A, 220, 112